

UNIVERSITÀ DEGLI STUDI DI MILANO
Facoltà di Scienze Matematiche Fisiche e Naturali
Dipartimento di Fisica

1

CORSO DI DOTTORATO DI RICERCA IN
FISICA, ASTROFISICA E FISICA APPLICATA
CICLO XX

**EXTRACTION OF CHARACTERISTIC CONSTANTS IN QCD
WITH PERTURBATIVE AND NONPERTURBATIVE METHODS**

FIS/02, Fisica Teorica, Modelli e Metodi Matematici

**TUTOR: Prof. Stefano FORTE
COTUTOR: Prof. Giovanni RIDOLFI**

COORDINATORE del DOTTORATO: Prof. Giampaolo BELLINI

**Claudia SIMOLO
Matricola R06096**

anno accademico 2006-2007

Extraction of characteristic constants
in QCD with perturbative and
nonperturbative methods

Contents

I	On the QCD coupling at low energy scales	6
1	The QCD coupling in Perturbation Theory	7
1.1	The Renormalization Group method in QCD	8
1.2	QCD β function	14
1.3	RG-invariant coupling	15
1.4	Threshold matching	20
1.5	Landau singularities	21
1.6	Time-like coupling	22
2	The APT theoretical scheme	28
2.1	The “Euclidean” ghost-free coupling	28
2.2	Two-loop and higher orders	30
2.3	The “Minkowskian” domain in APT	35
2.4	Modifications of APT and the massive case	38
3	Bound states approach	41
3.1	QCD coupling from the meson spectrum	41
3.2	BS-model for quarkonium states	45
3.3	Extracting $\alpha_s^{\text{exp}}(Q^2)$ from the data	48
3.4	Theoretical uncertainties	50

3.5	BS-model results: concert of low and high energy data via APT	53
-----	---	----

4	Conclusive remarks	58
----------	---------------------------	-----------

II Progress in the determination of the gluon polarization **78**

5	Polarized parton distributions from DIS	79
----------	--	-----------

5.1	Structure functions and their moments	80
-----	---	----

5.2	The parton model predictions	83
-----	--	----

5.3	Polarized structure functions and pdfs in QCD	85
-----	---	----

5.4	Phenomenology of g_1	88
-----	----------------------------------	----

5.5	Target mass corrections	91
-----	-----------------------------------	----

6	Global analysis of inclusive DIS data	94
----------	--	-----------

6.1	Analysis method	94
-----	---------------------------	----

6.2	Parametrization of pdfs	96
-----	-----------------------------------	----

6.3	Update	98
-----	------------------	----

6.4	Low-energy data	103
-----	---------------------------	-----

6.4.1	Selection of CLAS data	103
-------	----------------------------------	-----

6.4.2	Higher-twist effects	106
-------	--------------------------------	-----

6.5	Gluon polarization from g_1 data	109
-----	--	-----

6.5.1	Best-fit results and impact of the data on the gluon first moment	109
-------	--	-----

6.5.2	Dependence of Δg on input densities	113
-------	---	-----

6.6	Phenomenological implications	116
-----	---	-----

6.6.1	Best-fit results for g_1	116
-------	--------------------------------------	-----

6.6.2	Polarized quark and gluon densities	120
-------	---	-----

7	Open-charm photoproduction at COMPASS	124
7.1	Direct determination of Δg	125
7.1.1	Experiments at polarized proton-proton colliders	125
7.1.2	Lepton-nucleon scattering in polarized fixed target experiments	126
7.1.3	The open-charm method at COMPASS	127
7.2	Theoretical analysis of charm asymmetries at COMPASS	129
7.2.1	General framework	129
7.2.2	Leading order cross section	132
7.2.3	COMPASS kinematics	134
7.2.4	Pdfs and fragmentation function	137
7.3	Phenomenological results	140
7.3.1	Asymmetries as a function of the measured variables	140
7.3.2	Results from pseudo-data fit	149
8	Conclusions	154

Part I

On the QCD coupling at low energy scales

Chapter 1

The QCD coupling in Perturbation Theory

The Renormalization Group method is an inherent part of the theoretical description of strong interaction processes. As known, the values of the QCD coupling extracted from high-energy data are in good agreement with the theoretical running coupling $\alpha_s(Q^2)$ as derived by the RG equations and properly normalized at the Z boson mass, thus providing a powerful test of asymptotic freedom ¹.

On the other hand, in the low-energy domain, the running coupling $\alpha_s(Q^2)$ develops, at any loop level, unphysical (so-called Landau) singularities that contradict the general principles of the local Quantum Field Theory and severely complicate the theoretical analysis of hadron dynamics.

A reasonable prescription to get rid of the Landau singularities in the QCD coupling is given by the Analytic Perturbation Theory (APT) approach. In this framework, the analyticity properties are recovered by imposing $\alpha_s(Q^2)$ to satisfy a dispersion relation with only the unitary cut on the time-like axis, while preserving the asymptotic freedom constraint.

This prescription has been exploited in the framework of a second order Bethe-Salpeter-like (BS) formalism adjusted for QCD in recent works [24], for the calculation of the meson spectrum in the light and heavy quark sectors. It has been there emphasized the relevance of the infrared evolution of the APT coupling in the few hundreds MeV region for a reasonable reproduction

¹For a summary of the high energy measurements of $\alpha_s(Q^2)$ see [1, 2].

of ground state mesons involving light and strange quarks, at variance with a naive truncation prescription. This feature strongly supports the APT approach within the BS framework.

On the other hand, in the present work [3, 4], the calculations of the meson spectrum within the BS formalism have been exploited in order to obtain an experimental determination of the strong coupling $\alpha_s^{\text{exp}}(Q^2)$ below 1 GeV, by comparison with the data.

The results turn out to be in satisfying agreement with the APT coupling and its evolution in the 200-500 MeV region. Furthermore, below this scale, some hints on the deep IR behavior are further provided, albeit affected by large theoretical errors.

In Sec. 1 the Renormalization Group method in QCD is briefly reviewed, and the state-of-the-art on the infrared behavior of the QCD-invariant coupling sketched, whereas in Sec. 2 the basis of the Analytic Perturbation Theory approach are outlined. Sec. 3 is devoted to the determination of the experimental values of the QCD coupling from the meson spectrum, the analysis method and the discussion of the results.

Finally, some technical material is exposed in the Appendices. A short description of the derivation of the second order BS formalism is given in App. A, whereas numerical tables in App. B display all the results in detail.

1.1 The Renormalization Group method in QCD

In the framework of Quantum Field Theory, an arbitrary change in the renormalization prescription basically results in a reparametrization of the theory by a suitable redefinition of couplings and masses, so as to leave physical quantities unaffected. The behavior of relevant Green functions under a change in the extra mass scale μ introduced by renormalization is specified by a set of continuous transformations, properly expressed by the differential equations of the renormalization group (RG) ². This leads to the notion of effective couplings and masses.

Choosing a renormalization scheme (RS) which performs all subtractions off shell, mass parameters can be treated on the same foot as couplings.

²For an overview on history and applications see for instance [5] and references therein.

In the “minimal subtraction scheme” (MS) the renormalization factors exhibit no mass-dependence and are of the general form

$$Z_j(\varepsilon, \alpha_s) = 1 + \sum_{n=1}^{\infty} \varepsilon^{-n} Z_j^{(n)}(\alpha_s), \quad (1.1)$$

where $\alpha_s = g^2/4\pi$ is the strong coupling and ε is the deviation from the physical space-time dimension, $d = 4 - \varepsilon$. The so-called “modified minimal subtraction scheme” ($\overline{\text{MS}}$) amounts to subtracting the whole $(\ln 4\pi - \gamma_E)$ -term together with the poles, and it has become a common standard in QCD. In MS-like schemes the arbitrary mass scale μ arises to keep the coupling dimensionless in $4 - \varepsilon$ dimensions, and the renormalized objects turn out to be scale dependent.

In transition from one parametrization $(\mu_0^2, \alpha_s(\mu_0^2), m(\mu_0^2))$ to a different one $(\mu^2, \alpha_s(\mu^2), m(\mu^2))$ Green functions are connected by finite renormalization transformations, and, in order to have a unique theory under an infinitesimal shift of the scale, they must satisfy the (inhomogeneous) RG equation

$$\mathbb{R} \Gamma(p_i; \alpha_\mu, m_\mu, \mu^2) = \gamma_\Gamma(\alpha_\mu) \Gamma(p_i; \alpha_\mu, m_\mu, \mu^2), \quad (1.2)$$

where p_i are relevant momenta and the shorthand α_μ stands for $\alpha_s(\mu^2)$ (similarly for m_μ). The RG operator is the total derivative over the scale parameter, namely

$$\mathbb{R} \equiv \mu^2 \frac{\partial}{\partial \mu^2} + \beta \frac{\partial}{\partial \alpha_\mu} + \gamma_m m_\mu \frac{\partial}{\partial m_\mu}, \quad (1.3)$$

where the sum over n_f quark flavors in the mass-term is understood, and the universal functions

$$\beta(\alpha_\mu) \equiv \mu^2 \frac{\partial \alpha_\mu}{\partial \mu^2}, \quad \gamma_m(\alpha_\mu) \equiv \frac{\mu^2}{m_\mu} \frac{\partial m_\mu}{\partial \mu^2} \quad \text{and} \quad \gamma_\Gamma(\alpha_\mu) \equiv \mu^2 \frac{\partial}{\partial \mu^2} \ln Z_\Gamma \quad (1.4)$$

have been defined. The RG coefficients β, γ_m and γ_Γ are computed in perturbation theory (PT) with the aid of the relative counterterms. Generally speaking, they are gauge-dependent finite functions of couplings and masses, once the physical limit $\varepsilon \rightarrow 0$ is performed; actually, in any mass-independent RS (such as minimal subtraction prescriptions or trivially in massless theories), the RG coefficients are mass-independent and function of α_s alone.

As far as the QCD coupling is concerned, the beta function in the first of Eqs. (1.4) has the usual PT power expansion

$$\beta(\alpha_s) = -\beta_0 \alpha_s^2 - \beta_1 \alpha_s^3 - \beta_2 \alpha_s^4 + \mathcal{O}(\alpha_s^5), \quad (1.5)$$

where β_l are the l-loop coefficients. At 1-loop level (i.e. keeping only the first term in (1.5)) solution to the first of Eqs. (1.4) reads

$$\alpha_s(\mu^2) = \frac{\alpha_s(\mu_0^2)}{1 + \beta_0 \alpha_s(\mu_0^2) \ln(\mu^2/\mu_0^2)} = \alpha_s(\mu_0^2) \sum_{n=0}^{\infty} \left(-\beta_0 \alpha_s(\mu_0^2) \ln \frac{\mu^2}{\mu_0^2} \right)^n, \quad (1.6)$$

namely, while the theory does not predict the actual size of α_s , its scale evolution is completely known. Indeed, α_s is not an observable by itself, but plays the role of the effective expansion parameter for physical quantities, and any determination of the strong coupling is then extracted from the measurements of observables for which PT predictions exist. Conventionally the mass of the Z_0 boson, $M_Z \sim 91.2$ GeV, is used as a reference scale to the world average of all (high energy) determinations, which is currently $\alpha_s(M_Z^2) = 0.1176(20)$ [2, 1].

Defining the overall scale parameter

$$\Lambda^2 = \mu_0^2 \exp \left[-\frac{1}{\beta_0} \frac{1}{\alpha_s(\mu_0^2)} \right], \quad (1.7)$$

Eq. (1.6) becomes

$$\alpha_s(\mu^2) = \frac{1}{\beta_0 \ln(\mu^2/\Lambda^2)}. \quad (1.8)$$

Since $4\pi\beta_0 = (11 - 2n_f/3)$ is a positive number for all presently known flavours, $\alpha_s(\mu^2)$ decreases to zero as $\mu^2 \rightarrow 0$ (asymptotic freedom), this property being not spoiled by higher loop corrections.

Given the arbitrariness of the renormalization scale μ , the best choice is a matter of expediency. The commonly adopted prescription is to fix μ at the physical scale of the process at hand. This can be motivated by a glance to the homogeneous RG equation satisfied by any (dimensionless) observable G , namely ³

$$\mu^2 \frac{d}{d\mu^2} G = \left(\mu^2 \frac{\partial}{\partial \mu^2} + \beta(\alpha_s) \frac{\partial}{\partial \alpha_s} \right) G = 0 \quad (1.9)$$

³Actually quark masses have been neglected, assuming that both the physical and the renormalization scales Q^2 and μ^2 are larger than any other relevant mass scale. If non negligible, quark masses give rise to an additional term in Eq. (1.9), similarly to Eqs. (1.2) and (1.3).

where G is typically function of the ratio ⁴ Q^2/μ^2 and of the renormalized coupling $\alpha_s(\mu^2)$, and is given in PT by a power series in $\alpha_s(\mu^2)$

$$G = g_0 \left(\frac{Q^2}{\mu^2} \right) + g_1 \left(\frac{Q^2}{\mu^2} \right) \frac{\alpha_s(\mu^2)}{\pi} + g_2 \left(\frac{Q^2}{\mu^2} \right) \left(\frac{\alpha_s(\mu^2)}{\pi} \right)^2 + \mathcal{O}(\alpha_s^3). \quad (1.10)$$

Eq. (1.9) clearly states the scale invariance of any physical observable, that is fulfilled only in infinite order. In any truncated order, however, the cancellation of the scale among the coupling and the coefficients is not complete, that is, a residual scale and scheme dependence still persists, and the degree of cancellation improves with the inclusion of higher orders.

The solution of Eq. (1.9) for the PT coefficients g_j exhibits a logarithmic dependence on Q^2/μ^2 (starting from the order α_s^2), that can be controlled by setting $Q^2 = \mu^2$. Then Eq. (1.10) takes the form

$$G(q) = \bar{g}_0 + \bar{g}_1 \frac{\alpha_s(Q^2)}{\pi} + \bar{g}_2 \left(\frac{\alpha_s(Q^2)}{\pi} \right)^2 + \mathcal{O}(\alpha_s^3), \quad (1.11)$$

and the energy dependence of G translates into the energy dependence of the effective parameter $\alpha_s(Q^2)$. A change in the value of μ^2 clearly amounts to a reorganization of the PT expansion.

The RG improved perturbative QCD yields a consistent picture of high energy strong interaction processes ⁵ from a few GeV up to a few hundred GeV. On the other hand, the existence of infrared singularities in the RG-invariant coupling $\alpha_s(Q^2)$ spoils the theoretical analysis of low energy hadron dynamics. Indeed, at 1-loop level $\alpha_s(Q^2)$, as given by Eq. (1.8), has a pole-type singularity at $Q^2 = \Lambda^2$, and the effect of including higher order contributions does not overcome the problem and only amounts to modifying the singularity structure. On the contrary, physical observables are known to be analytic in the entire q^2 complex plane aside from a cut on the real positive (time-like) axis, and their exact expressions should be free of these singularities.

Many strategies have been suggested to get rid of unphysical singularities within PT calculations, so as to handle the strong interaction processes at

⁴Actually, according to the process, more than one scale can be involved, and this can be spacelike ($q^2 < 0$ and $Q^2 = -q^2$) or timelike ($q^2 > 0$ and $s = q^2$).

⁵Some care is required for timelike observables since the PT coefficients, in this case, are modified by non negligible corrections, proportional to powers of $\beta_0\pi$, due to the analytic continuation from the space-like to the time-like domain (see Sec. 1.6).

low energies. Some of such methods, reviewed e.g. in Ref. [6], originate in the general properties of the perturbative power series for the QCD observables in the framework of the RG formalism, such as the arbitrariness of the renormalization scheme and scale. One can remind, for instance, the Brodsky-Lepage-Mackenzie criterion [7], the “Optimal conformal mapping method” [8] (see also Ref. [9]), and the so-called “Fastest Apparent Convergence” technique [10]. The latter, e.g. amounts to setting the scale so that all the higher (than LO) coefficients vanish. It is related to the *effective charges*, [11]-[13], i.e. alternative definitions of the QCD coupling, straightforwardly related to a physical observable, either of spacelike or time-like argument.

In this context it is also worth mentioning the “Optimized Perturbation Theory” approach [14, 15], with the aim of improving the convergence of PT expansions by a proper choice of the scale and of RS parameters (such as β_2 and β_3), on the basis of a minimum sensitivity criterion.

However, all these definitions can be related to each other by referring back to the conventional $\overline{\text{MS}}$. Most of these techniques yield theoretical predictions on the low energy behavior of the RG-invariant coupling which are in qualitative agreement, suggesting in all cases an IR finite limit.

Furthermore, recent results of lattice simulations testify to the absence of spurious IR singularities in the QCD coupling [16, 17].

The ghost-pole issue gives rise to severe complications, in particular, as far as the bound states problem is concerned, since the characteristic scale Q involved (i.e., the momentum transfer in the quark-antiquark interaction for mesons) is typically below 1 GeV, according to the state and the mass of quarks involved.

Among the many potential inspired attempts to modify the expression of α_s in the low energy domain, there exist either trivial tricks as the truncation prescription ⁶, as well as more sophisticated models. For instance, one can remind the 1-loop definition of the QCD coupling in connection with the momentum representation of the Cornell-like potential [18]

$$\alpha_V(Q^2) = \frac{1}{\beta_0 \ln(1 + Q^2/\Lambda^2)}, \quad \tilde{V}(Q) = -\frac{1}{2\pi^2} \frac{4}{3} \frac{\alpha_V(Q^2)}{Q^2}; \quad (1.12)$$

as $Q \rightarrow \infty$, the usual 1-loop coupling (1.8) is recovered from the first of Eqs.

⁶This simply amounts to assuming $\alpha_s(Q^2)$ frozen at a maximum finite value in the IR region.

(1.12), whereas as $Q \rightarrow 0$ the latter diverges as $\Lambda^2/\beta_0 Q^2$, incorporating non-perturbative effects ⁷. Estimation of higher order corrections and further developments along this line can be found in [19]. On the other hand, a number of analyses seems rather consistent with an IR finite coupling and a suitable modification of the quark-antiquark potential to encode confinement (see e.g. [20, 21, 22, 27]).

A reliable algorithm to get rid of Landau singularities is provided by the Analytic Perturbation Theory (APT) approach [23], which represents a next step, after RG summation, in improving the perturbative results. The APT method, as discussed to some extent in Sec. 2, is based on the causality condition which imposes the analyticity constraint on the RG-invariant coupling on the whole cut complex plane $\mathcal{C} - \{q^2 > 0\}$. PT is then used to evaluate the spectral function, i.e. the discontinuity of $\alpha_s(Q^2)$ across the cut. At 1-loop, e.g., it reads

$$\text{Im} [\alpha_s(-\sigma)] = \frac{\pi\beta_0\alpha_s^2(\mu_0^2)}{[1 + \beta_0\alpha_s(\mu_0^2)\ln(\sigma/\mu_0^2)]^2 + [\pi\beta_0\alpha_s(\mu_0^2)]^2}, \quad (1.14)$$

where Eq. (1.6) has been used. Indeed, within the causal approach, Landau singularities are suppressed at their very roots, and the IR-safe QCD coupling possesses a universal finite limit as $Q^2 \rightarrow 0$.

In what follows the basis of the derivation of the QCD coupling from the Renormalization Group equations are reviewed, both in the space-like and time-like domains.

⁷This can be seen by comparing the second of (1.12) with the usual Cornell potential in the momentum space representation

$$V(Q) = -\frac{1}{2\pi^2} \frac{4}{3} \frac{\alpha_s(\mu^2)}{Q^2} - \frac{1}{\pi^2} \frac{\sigma}{Q^4}, \quad (1.13)$$

and identifying the quantity $2\Lambda^2/3\beta_0$ with the string tension σ that controls the confining part of the potential.

1.2 QCD β function

The RG equation for the effective coupling is actually solved in PT with the aid of the relation

$$\beta(\alpha_s) = -\alpha_s \frac{\mu \partial}{\partial \mu} \ln Z_\alpha \quad (1.15)$$

where the limit $\varepsilon \rightarrow 0$ is understood. Thus one needs to compute the renormalization factor for the coupling Z_α and this can be accomplished in several ways. One can start from the quark-gluon vertex $Z_{\bar{q}qg}$ together with renormalization factors of quark and gluon propagators Z_q and Z_g to obtain $Z_\alpha = Z_{\bar{q}qg}^2 Z_q^{-2} Z_g^{-1}$, but other choices, as ghost-ghost-gluon vertex or trilinear and quartic gluon interactions, equally work. In a minimal subtraction prescription the four-dimensional β -function is entirely specified by the residuum of the simple pole in the ε -expansion of Z_α (1.1)

$$\beta(\alpha_s) = \frac{1}{2} \alpha_s^2 \frac{d}{d\alpha_s} Z_\alpha^{(1)}(\alpha_s). \quad (1.16)$$

Then the MS-coefficients in Eq. (1.5) reads [29]

$$\begin{aligned} \beta_0 &= \frac{1}{4\pi} \left[11 - \frac{2}{3} n_f \right] \\ \beta_1 &= \frac{1}{(4\pi)^2} \left[102 - \frac{38}{3} n_f \right] \\ \beta_2 &= \frac{1}{(4\pi)^3} \left[\frac{2857}{2} - \frac{5033}{18} n_f + \frac{325}{54} n_f^2 \right] \\ \beta_3 &= \frac{1}{(4\pi)^4} \left[\left(\frac{149753}{6} + 3564 \zeta_3 \right) - \left(\frac{1078361}{162} + \frac{6508}{27} \zeta_3 \right) n_f \right. \\ &\quad \left. + \left(\frac{50065}{162} + \frac{6472}{81} \zeta_3 \right) n_f^2 + \frac{1093}{729} n_f^3 \right] \end{aligned} \quad (1.17)$$

where ζ_ν is the Riemann zeta-function, $\zeta_3 \simeq 1.202057$. The coefficients β_j generally depend on the RS, whereas the first two are universal within massless schemes. Moreover, in the MS-scheme the β -function is gauge-independent in any order [30], and in an arbitrary mass-dependent scheme this feature is preserved only in the first order.

As already noted, the universal 1-loop coefficient [31] has a positive sign provided there is a small enough number of quark fields ($n_f \leq 33/2$); thus the

theory is asymptotically free, that is, the β -function has a stable UV fixed point as its argument decreases to zero. Indeed this coefficient is the sum of two contributions, the relevant one with respect to asymptotic freedom property being the first, which arises from pure gauge field effects i.e. from the nonlinear Yang-Mills interaction terms. The 2-loop coefficient has been computed for the first time in [32] and is positive up to $n_f = 8$.

Higher order approximations are scheme-sensitive, and it is common practice to perform computation within minimal subtraction prescriptions, in which the β -function is unchanged. The first calculation of 3-loop coefficient is due to [33], where the ghost-ghost-gluon vertex in the Feynman gauge was used, and it turns out to be negative for $6 \leq n_f \leq 40$. In a more recent work [34] the quark-gluon vertex was used instead, providing an independent check in an arbitrary covariant gauge of the previous result and its gauge-independence. Finally, the original 4-loop calculation [29] has been performed using the ghost-ghost-gluon vertex in a arbitrary covariant gauge, and for a generic semi-simple compact Lie symmetry group. The result turns out to be gauge-independent, and involves higher order group invariants such as quartic Casimir operators; specialized to the standard SU(3) symmetry, the 4-loop coefficient is a positive number for every positive n_f (see also [35]). Finally note that (except for β_2) all four coefficients are positive up to $n_f = 6$.

1.3 RG-invariant coupling

The formal solution of the first of Eq. (1.4) is easily worked out

$$\ln \frac{\mu^2}{\mu_0^2} = \int_{\alpha_s(\mu_0^2)}^{\alpha_s(\mu^2)} \frac{d\alpha_s}{\beta(\alpha_s)}, \quad (1.18)$$

and yields the evolution of the effective coupling as a function of two dimensionless arguments $t = \mu^2/\mu_0^2$ and $\alpha_0 = \alpha_s(\mu_0^2)$, where μ_0^2 can be viewed as a fixed reference scale and μ^2 as a sliding one. It is worth noting that by differentiating Eq. (1.18) with respect to α_0 one has

$$\left(t \frac{\partial}{\partial t} - \beta(\alpha_0) \frac{\partial}{\partial \alpha_0} \right) \alpha_s(t, \alpha_0) = 0, \quad (1.19)$$

namely the homogeneous RG equation satisfied by the effective coupling (or invariant charge).

The exact 1-loop solution (1.6) or (1.8) is obtained by retaining only the first term in (1.5). In Eq. (1.8), in particular, the dimensional scale Λ keeps track of the initial parametrization $(\mu_0, \alpha_s(\mu_0^2))$, and it is scale-invariant; its value is not predicted by the theory but must be extracted from a measurement of α_s at a given reference scale. Emergence of a scale parameter, sometimes referred to as dimensional transmutation, breaks naive scale invariance of the massless theory, and it is commonly believed to be associated with the typical hadron size i.e. to the energy scale where confinement effects set in. Roughly speaking, Λ is the scale at which the (1-loop) coupling diverges (Landau pole), and perturbation theory becomes meaningless. Further, Λ is scheme-dependent and receives further corrections at each loop level (but for simplicity the same notation is used throughout).

At the 2-loop level the integration of (1.18) leads to a transcendental equation, that is, starting from the 2-loop approximation to the β -function in (1.5), one has

$$\ln \frac{\mu^2}{\mu_0^2} = C + \frac{1}{\beta_0 \alpha_s} + B_1 \ln \alpha_s - B_1 \ln \left(1 + \frac{\beta_1}{\beta_0} \alpha_s \right) \quad (1.20)$$

where $B_1 = \beta_1/\beta_0^2$ and the constant term C from the lower end points can be again reabsorbed into the Λ -parametrization, with the commonly adopted prescription (see e.g.[36, 37])

$$\ln \frac{\Lambda^2}{\mu_0^2} = C - B_1 \ln \beta_0, \quad (1.21)$$

which fixes a specific choice for Λ . Thus one gets the 2-loop implicit solution

$$\ln \frac{\mu^2}{\Lambda^2} = \frac{1}{\beta_0 \alpha_s} - B_1 \ln \left(B_1 + \frac{1}{\beta_0 \alpha_s} \right), \quad (1.22)$$

from which the 2-loop scaling parameter is immediately read. To achieve an explicit expression for the running coupling at this level one should resort to the many-valued Lambert function $W(\zeta)$ implicitly defined by the equation

$$W(\zeta) \exp [W(\zeta)] = \zeta. \quad (1.23)$$

The function $W(\zeta)$ has an infinite number of branches $W_k(\zeta)$ $k = 0, \pm 1, \pm 2 \dots$ such that $W_n^*(\zeta) = W_{-n}(\zeta^*)$ (for more details see [38]). The exact solution

to Eq. (1.22) for $0 \leq n_f \leq 8$ reads ⁸ (see e.g. [39])

$$\alpha_{ex}^{(2)}(z) = -\frac{1}{\beta_0 B_1} \frac{1}{1 + W_{-1}(\zeta)} \quad \zeta = -\frac{1}{e B_1} \left(\frac{1}{z}\right)^{1/B_1} \quad (1.24)$$

where $z = \mu^2/\Lambda^2$, and $W_{-1}(\zeta)$ is the ‘‘physical’’ branch of the Lambert function, since it defines a real values function for $\zeta \in (-e^{-1}, 0)$ which fulfills the asymptotic freedom constraint. As $\varepsilon \rightarrow 0^+$ the asymptotic relations

$$W_{-1}(-\varepsilon) = \ln \varepsilon + O(\ln |\ln \varepsilon|) \quad (1.25)$$

$$W_{-1}\left(-\frac{1}{e} + \varepsilon\right) = -1 - \sqrt{2e\varepsilon} + O(\varepsilon) \quad (1.26)$$

hold. Outside this region of the real axis $W_{-1}(-\varepsilon)$ takes on complex values. Though not easy for practical aims, Eq. (1.24) yields the most accurate expression for investigating the IR behavior of the running coupling, since it has not been derived by means of deep perturbative approximations (aside from the truncation of the 2-loop β function).

Actually, a frequently used 2-loop approximate solution, known as the *iterative* solution [23], is obtained starting from Eq. (1.20) together with a single iteration of the 1-loop formula (1.8), that is

$$\alpha_{it}^{(2)}(z) = \frac{\beta_0^{-1}}{\ln z + B_1 \ln(1 + B_1^{-1} \ln z)}, \quad (1.27)$$

where $z = \mu^2/\tilde{\Lambda}^2$, and $\tilde{\Lambda}$ now defined in (1.20) by

$$\ln \frac{\tilde{\Lambda}^2}{\mu_0^2} = C - B_1 \ln \frac{\beta_1}{\beta_0}. \quad (1.28)$$

This definition is related to the standard one (1.21) by the factor

$$\ln(\Lambda/\tilde{\Lambda}) = \frac{1}{2} B_1 \ln B_1. \quad (1.29)$$

However, the commonly used 2-loop solution is an asymptotic formula which strictly relies on the smallness of α_s for fairly large μ^2 , since it amounts to

⁸Note that if $9 \leq n_f \leq 16$ the principal branch W_0 is involved, but here and throughout the discussion is focused on $n_f \leq 6$.

solving Eq. (1.20) (with the choice (1.21)) where the last term in the r.h.s. has been neglected. Again, after one iteration of the 1-loop formula, the result is then re-expanded in powers of $1/L$, where $L = \ln z$ and $z = \mu^2/\Lambda^2$ as before

$$\alpha_s^{(2)}(z) = \frac{1}{\beta_0 \ln z} \left[1 - \frac{\beta_1 \ln(\ln z)}{\beta_0^2 \ln z} \right]. \quad (1.30)$$

Eq.(1.30) is known as the standard 2-loop running coupling and works only in the deep UV regime, i.e. for $L \gg 1$. In Fig. 1(a) the fractional differences of the two approximate formulas Eqs. (1.27) and (1.30) with respect to the exact 2-loop coupling Eq. (1.24) are displayed.

Under the same assumptions of Eq. (1.30) one can easily derive the 3 and 4-loop asymptotic formulas. Starting with the approximate implicit solution at the 4-loop level, namely

$$\ln \frac{\mu^2}{\mu_0^2} = C + \frac{1}{\beta_0 \alpha_s} + \frac{\beta_1}{\beta_0^2} \ln \alpha_s + \frac{\beta_2 \beta_0 - \beta_1^2}{\beta_0^3} \alpha_s + \frac{\beta_1^3 - 2\beta_0 \beta_1 \beta_2 + \beta_0^2 \beta_3}{2\beta_0^4} \alpha_s^2 + O(\alpha_s^3), \quad (1.31)$$

the 4-loop coupling in the standard form of an expansion in inverse powers of the logarithm L for $L \gg 1$ (see e.g. [40]) reads

$$\alpha_s^{(4)}(\mu^2) = \frac{1}{\beta_0 L} \left\{ 1 - \frac{\beta_1 \ln L}{\beta_0^2 L} + \frac{1}{\beta_0^2 L^2} \left[\frac{\beta_1^2}{\beta_0^2} (\ln^2 L - \ln L - 1) + \frac{\beta_2}{\beta_0} \right] + \frac{1}{\beta_0^3 L^3} \left[\frac{\beta_1^3}{\beta_0^3} \left(-\ln^3 L + \frac{5}{2} \ln^2 L + 2 \ln L - \frac{1}{2} \right) - 3 \frac{\beta_1 \beta_2}{\beta_0^2} \ln L + \frac{\beta_3}{2\beta_0} \right] \right\}. \quad (1.32)$$

The 4-loop solution (1.32) turns out to be nearly indistinguishable from the 3-loop curve (see Fig. 1(b)). In Eq. (1.32) the 1-loop solution (1.8) has been emphasized, and being the leading UV term in (1.32), it defines the asymptotic behavior of the RG-invariant coupling. On the other hand, the 2 and 3-loop asymptotic expressions are easily read from Eq. (1.32) by keeping only the first two and three terms respectively.

Exact integration of the truncated 4 or 3-loop β -function leads to a more involved structure than Eq. (1.31). Nevertheless, in [39] a useful solution has been still worked out at 3-loop level via the real branch $W_{-1}(\zeta)$ of the Lambert function together with the Pade' Approximant of the related β -function. Moreover, in [41] a reliable approximation to the higher-loop coupling has been suggested, via a power expansion in the 2-loop exact coupling (1.24),

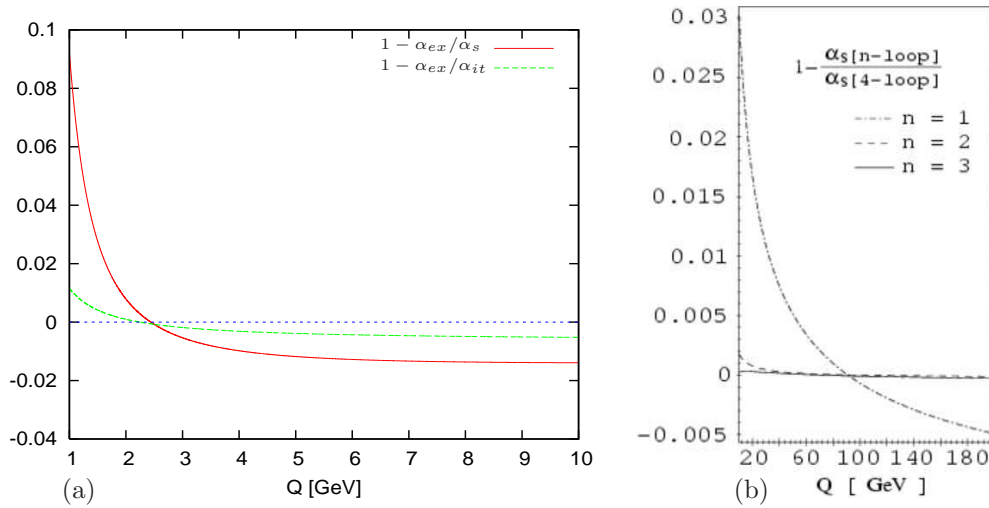


Figure 1.1: (a) Fractional difference between Eqs. (1.24), (1.30) and (1.27) (solid and dashed line respectively), with $\Lambda = 350$ MeV and $n_f = 4$. (b) From [1]: fractional difference between the 4-loop and the 1-, 2-, 3-loop approximations to Eq. (1.32), with $n_f = 5$ and normalization conditions at $\alpha_s(M_Z^2) = 0.119$.

of the form

$$\alpha_s^{(k)}(\mu^2) = \sum_{n \geq 1} p_n^{(k)} [\alpha_{ex}^{(2)}(\mu^2)]^n \quad (1.33)$$

with $k \geq 3$ the loop order, and $p_n^{(k)}$ proper functions of the coefficients β_j . Comparison [42] of these multi-loop approximants with the relative asymptotic formulas, Eq.(1.32) and the 3-loop analogue, reveals the better agreement of the former ones with the higher-loop exact coupling numerically estimated (i.e. starting from the exact implicit solution), even at rather low energy scales (see also [43]).

Finally, as far as the definition of the scaling constant Λ is concerned, few comments are in order. As already pointed out, starting from the 2-loop level an arbitrary constant has to be fixed for Λ to be uniquely defined; beside the commonly accepted convention (1.21) (or (1.28)), other prescriptions have been proposed [44] in order to optimize the $1/L$ -expansion, while (1.21) does remain the preferred one as no further terms of order $1/L^2$ appear in the 2-loop asymptotic formula (1.30). Thus, at higher-loop levels the scaling parameter is analogously related to the initial parameterization, and the 4-loop (and 3-loop) value reproducing the world average $\alpha_s(M_Z^2) = 0.119$ is $\Lambda_{\overline{\text{MS}}}^{(n_f=5)} = 220$ MeV [1].

Furthermore, with regard to the scheme-dependence of the coupling and the

scale parameter, restricting the discussion to mass-independent RS (as MS-like schemes or trivially any prescription in the massless theory), the renormalized couplings in two such different schemes can be related perturbatively at any fixed scale μ

$$\alpha'_s = \alpha_s \left[1 + v_1 \frac{\alpha_s}{\pi} + v_2 \left(\frac{\alpha_s}{\pi} \right)^2 + \dots \right]. \quad (1.34)$$

Then, it can be verified that the first two coefficients of the relative β -functions do not change as the renormalization prescription is changed, while, for instance, the 3-loop ones are related by $\beta'_2 = \beta_2 - v_1 \beta_1 + v_2 \beta_0 - \beta_0 v_1^2$. As a result, the running coupling at each loop-level (e.g. Eq. (1.32)) depends on the RS, through the coefficients β_j with $j \geq 2$ and the initial parameterization. The latter obviously amounts to suitably adjusting the Λ , and the relation is given by [45]

$$\ln(\Lambda'/\Lambda) = \frac{v_1}{2\pi\beta_0}, \quad (1.35)$$

which works through all orders (e.g. $\Lambda_{\overline{\text{MS}}}/\Lambda_{\text{MS}} = \exp[(\ln 4\pi - \gamma_e)/2] \simeq 2.66$).

1.4 Threshold matching

Quark mass effects reveal themselves in explicit corrections within higher order perturbation theory (see e.g. [46]), and in the energy dependence of the effective (running) quark masses as a result of the RG improvement [47]. A direct effect of the quark masses on the evolution of the coupling is through the dependence of the β coefficients on the number n_f of active quarks, i.e. satisfying $m_f \ll \mu$, where μ is the renormalization scale and m_f the $\overline{\text{MS}}$ quark mass (the definition can be also formulated in terms of the pole mass M_f that can be related to the former [48]).

Then, in order to have a continuous coupling on the whole domain, the two functions $\alpha_s^{(n_f)}(\mu^2)$ and $\alpha_s^{(n_f-1)}(\mu^2)$ must be matched at each heavy quark mass scale $\mu^{(n_f)} = O(m_f)$. As a result the scaling parameter Λ depends also on n_f (see e.g. [49, 40]).

The most straightforward way is to impose continuity of α_s by means of the matching condition $\alpha_s^{(n_f-1)}(m_f^2) = \alpha_s^{(n_f)}(m_f^2)$, which works up to next-to-

leading order. At 1-loop, it yields

$$\Lambda^{(n_f)} = \Lambda^{(n_f-1)} \left[\frac{\Lambda^{(n_f-1)}}{m_f} \right]^{2/(33-2n_f)}, \quad (1.36)$$

that can be extended up to 2-loop, and exhibits explicit dependence on m_f . Since trivial matching does not generally hold in higher orders within $\overline{\text{MS}}$ scheme, a more accurate formula is required in this case; specifically to obtain the global evolution of the 4-loop coupling the proper matching condition reads [40]

$$\alpha_s^{(n_f-1)} = \alpha_s^{(n_f)} \left[1 + k_2 \left(\frac{\alpha_s^{(n_f)}}{\pi} \right)^2 + k_3 \left(\frac{\alpha_s^{(n_f)}}{\pi} \right)^3 \right] \quad (1.37)$$

with

$$k_2 = \frac{11}{72}, \quad k_3 = \frac{564731}{124416} - \frac{82043}{27648} \zeta_3 - \frac{2633}{31104} (n_f - 1) \quad (1.38)$$

if $\mu^{(n_f)} = m_f$ is exactly assumed. With this convention, Eq. (1.37) yields the relationship between $\Lambda^{(n_f-1)}$ and $\Lambda^{(n_f)}$ in the $\overline{\text{MS}}$ scheme. One can equally fix $\mu^{(n_f)} = M_f$, that amounts to a proper adjustment of the coefficients in (1.37); for instance [1] starting with (1.32) and $\Lambda^{(n_f=5)} = 220$ MeV, the values $\Lambda^{(n_f=4)} = 305$ MeV and $\Lambda^{(n_f=3)} = 346$ MeV are obtained, with thresholds fixed at the pole masses $M_b = 4.7$ GeV and $M_c = 1.5$ GeV.

Note finally that Eq. (1.37) spoils continuity of α_s ; therefore, one can resort to a more sophisticated technique [50], which relies upon mass-dependent RS and yields a smooth transition across thresholds.

1.5 Landau singularities

As already noted, the 1-loop coupling (1.8) is affected by a spacelike pole at Λ with residue $1/\beta_0$. Adding multi-loop corrections does not overcome the hurdle; rather, the singularity structure is more involved due to the log-of-log dependence, so that a branch cut adds on to the 1-loop single pole in the IR domain of the spacelike axis.

Moreover, at a given loop level, Landau singularities sensibly depend on the

approximation used. For instance, the 2-loop iterative formula (1.27) has a pole at $z = 1$ ($\mu = \tilde{\Lambda}$, see Eqs. (1.28) and (1.29)) with residue $1/(2\beta_0)$, and a cut for $0 < z < \exp(-B_1)$ due to the double logarithm. On the other hand, in the 2-loop asymptotic expression Eq. (1.30), the singularity in $z = 1$ becomes stronger, namely

$$\alpha_s^{(2)}(z) \simeq -\frac{B_1 \ln(z-1)}{\beta_0 (z-1)^2} \quad z = \mu^2/\Lambda^2 \rightarrow 1 \quad (1.39)$$

and the cut now runs from 0 to 1. Analogously, the 3- and 4-loop asymptotic solutions, as given by Eq. (1.32), behave as

$$\alpha_s^{(3)}(z) \simeq \frac{B_1^2 \ln^2(z-1)}{\beta_0 (z-1)^3}, \quad \alpha_s^{(4)}(z) \simeq -\frac{B_1^3 \ln^3(z-1)}{\beta_0 (z-1)^4} \quad z \rightarrow 1, \quad (1.40)$$

and are equally affected by an unphysical cut. However, the cumbersome singularities structure of the leading Landau singularity, and of the unphysical cut as well, are an artifact of the UV approximations introduced. Therefore to deal with the IR behavior of the invariant coupling it is necessary to face with the exact solution, e.g. Eq. (1.24) at 2-loop; clearly it is singular when $W_{-1}(\zeta) = -1$ that is at $z = B_1^{-B_1}$ ($\mu^2 = B_1^{-B_1} \Lambda^2$), corresponding to the branch point $\zeta = -1/e$ of the Lambert function. In the neighborhood of this point, due to the asymptotic behavior (1.26) of $W_{-1}(\zeta)$, one has

$$\alpha_{ex}^{(2)}(z) \simeq \frac{1}{\beta_0} \sqrt{\frac{B_1^{-B_1-1}}{2}} [z - B_1^{-B_1}]^{-1/2}, \quad (1.41)$$

i.e., an integrable singularity (the factor $B_1^{-B_1}$ in front of Λ in the singular point can be reabsorbed into a proper redefinition of the integration constant, through Eq. (1.29)).

A more detailed investigation about the IR singularity structure of higher-order approximations of the QCD coupling has been performed in Ref. [43], on the basis of Eq. (1.33), where, in particular, the location of Landau singularities as a function of n_f are studied.

1.6 Time-like coupling

The evolution of the QCD coupling has been derived above in the space-like region. However, in order to parametrize observables of time-like arguments,

one needs an effective coupling defined on the whole real axis.

While this poses no special problems in high energy processes, at any finite energy the issue of which should be the most suitable parameter in the s-channel must be carefully considered. The standard practice is to merely take over to the time-like domain the space-like coupling at any loop level, regardless of the crossing between two disconnected regions, thus exporting the IR singular structure in the s-channel. Nevertheless, from many early works based upon analysis of e^+e^- -annihilation into hadrons (see [51] and references therein), it is known that this should not be the case except far in the asymptotic regime. This is because of the appearance of not negligible corrections (π^2 -terms) in the higher order coefficients of the $\alpha_s(s)$ -expansions, due to analytic continuation from space-like to time-like axis. The problem is related to the IR non analyticity of the invariant coupling, and it receives a satisfactory answer in the framework of Analytic Perturbation Theory, in which the space-like and time-like channels are treated in a unified description (see Sec. 2).

Referring for definiteness to the e^+e^- -annihilation ratio into hadrons

$$R(s) = \frac{\sigma(e^+e^- \rightarrow \text{hadrons})}{\sigma(e^+e^- \rightarrow \mu^+\mu^-)}, \quad (1.42)$$

where $s = q^2 > 0$, one can start with the hadronic contribution to the photon polarization tensor in (space-like) momentum space

$$\Pi_h^{\mu\nu}(q) = (g^{\mu\nu}q^2 - q^\mu q^\nu)\Pi_h(-q^2) \propto \int d^4x e^{iqx} \langle 0|T(j^\mu(x)j^\nu(0))|0 \rangle \quad (1.43)$$

j^μ being the quark electromagnetic current operator. As is known, exploiting the analytical properties of the two-point correlation function (1.43) in the cut complex plane $\mathbb{C} - \{q^2 > 0\}$, $R(s)$ can be straightforwardly related to the discontinuity of $\Pi_h(-q^2)$ across the cut

$$R(s) = \frac{1}{2\pi i} \lim_{\varepsilon \rightarrow 0} [\Pi_h(-s + i\varepsilon) - \Pi_h(-s - i\varepsilon)]. \quad (1.44)$$

In order to compute $\Pi_h(-q^2)$ on the space-like axis ($q^2 < 0$) one formally works with its first logarithmic derivative (thus avoiding subtraction constants), the Adler D -function [52]

$$D(-q^2) = -q^2 \frac{d\Pi_h(-q^2)}{dq^2}. \quad (1.45)$$

The RG improved PT expansion of the D -function reads

$$D_{\text{PT}}(Q^2) = 3 \sum_f Q_f^2 \left[1 + \frac{\alpha_s(Q^2)}{\pi} + d_2 \left(\frac{\alpha_s(Q^2)}{\pi} \right)^2 + d_3 \left(\frac{\alpha_s(Q^2)}{\pi} \right)^3 + \dots \right] \quad (1.46)$$

where $Q^2 = -q^2$, Q_f are the quark charges, and the coefficients in the $\overline{\text{MS}}$ scheme read [53]

$$d_2 \simeq 1.986 - 0.115n_f$$

$$d_3 \simeq 18.244 - 4.216n_f + 0.086n_f^2 - 1.24 \left(3 \sum_f Q_f^2 \right)^{-1} \left(\sum_f Q_f \right)^2 \quad (1.47)$$

Then, by integration, $\Pi_h(Q^2)$ is readily obtained⁹. The result for $R(s)$ is then usually recasted as a series in the effective parameter $\alpha_s(s)$, naively obtained by specular reflection, that is by replacing the space-like argument $Q^2 = -q^2 > 0$ with the time-like one $s = q^2 > 0$. Starting from $\mathcal{O}(\alpha_s^3)$ the series displays corrections proportional to π -powers, as a drawback of the analytic continuation of the hadronic tensor. Then the ordinary perturbative expansion for $R(s)$ (e.g. [54]) reads

$$R_{\text{PT}}(s) = 3 \sum_f Q_f^2 \left[1 + \frac{\alpha_s(s)}{\pi} + r_2 \left(\frac{\alpha_s(s)}{\pi} \right)^2 + r_3 \left(\frac{\alpha_s(s)}{\pi} \right)^3 + \dots \right] \quad (1.48)$$

$$r_2 = d_2; \quad r_3 = d_3 - \delta_3, \quad \delta_3 = \frac{\pi^2 b_0^2}{48} \quad (1.49)$$

with d_2 and d_3 the same as in (1.46), and $b_j = (4\pi)^{j+1} \beta_j$. The correction δ_3 gives to the $\mathcal{O}(\alpha_s^3)$ coefficient a strongly negative contribution for each n_f (roughly $\delta_3 \simeq 14.3$ for $n_f = 4$). Higher order π^2 -terms were analyzed in [55] and show a remarkable growth; for instance, the fourth order correction is

$$\delta_4 \equiv d_4 - r_4 = \frac{\pi^2 b_0^2}{16} \left(r_2 + \frac{5b_1}{24b_0} \right) \quad (1.50)$$

with $\delta_4 \simeq 120$ for $n_f = 4$. A similar treatment also holds for other s-channel observables [54], such as the normalized rate for τ -decay into hadrons. The

⁹In the massless case the cut spreads over the whole positive axis, while taking into account quark masses the cut starts at the two-pion threshold $4m_\pi^2$.

effects of analytic continuation then make the perturbative expansions in the time-like region different from Euclidean ones.

Since the π^2 -terms play a dominant role in higher order coefficients, expansion (1.48) works only asymptotically at large s , that is when the smallness of $\alpha_s(s)$ scales down these large contributions. Actually, as already noted in pioneer works [56, 57], the expression of $R(s)$, resulting from Eq. (1.44) exhibits no natural expansion parameter (since both real and imaginary parts of $\alpha_s(Q^2)$ enter into the expression of R), and its choice is essentially a matter of expediency.

Alongside less meaningful attempts, one can remind e.g. the analysis performed in Ref. [56] of the quantity

$$|\alpha_s(-s)| = \frac{1}{\beta_0} \left[\frac{1}{\ln^2(s/\Lambda^2) + \pi^2} \right]^{1/2} \quad (1.51)$$

as expansion parameter for $R(s)$. Among the main features, Eq. (1.51) turns out to be IR finite, thus avoiding the hurdle of Landau singularities on the time-like domain, whereas asymptotically, i.e. for $s \gg \Lambda^2 e^\pi$, it reads

$$|\alpha_s(-s)| = \frac{1}{\beta_0} \frac{1}{\ln(s/\Lambda^2)} \left[1 - \frac{\pi^2}{2} \frac{1}{\ln^2(s/\Lambda^2)} + \dots \right], \quad (1.52)$$

resembling the UV behavior of the related space-like coupling (1.8). However, Eq. (1.51) cannot entirely sum up the π^2 -terms.

In order to deal with these corrections, a somewhat different approach, known as RKP (Radyushkin-Krasnikov-Pivovarov) procedure, has been suggested [44, 58] (see also [59]), which is based upon the analytical properties of the polarization tensor $\Pi_h(-q^2)$ and of the related D -function (1.45), that can be summarized by the dispersion relations, respectively

$$\Pi_h(-q^2) = \int_0^\infty ds \frac{R(s)}{s - q^2}, \quad (1.53)$$

$$D(-q^2) = -q^2 \int_0^\infty ds \frac{R(s)}{(s - q^2)^2} \quad (1.54)$$

with $R(s)$ given by (1.44), and q^2 lying in $\mathbb{C} - \{q^2 = s > 0\}$. The key point here is the inverse of Eq. (1.54), given by the contour integral

$$R(s) = \frac{i}{2\pi} \int_{s-i\varepsilon}^{s+i\varepsilon} \frac{dq^2}{q^2} D(-q^2), \quad (1.55)$$

to be computed along a path in the analyticity region for the D -function. Eq. (1.55) can be then generalized to an integral transformation, mapping a space-like argument function into a time-like one

$$R(s) = \Phi [D(-q^2)] . \quad (1.56)$$

This can be straightforwardly applied to the perturbative expansion (1.46), provided that the integration contour is always kept far enough from IR space-like singularities. This yields $R(s)$ as an expansion into the images of $\alpha_s(Q^2)$ and of its powers, through the map Φ [44]

$$R(s) = 3 \sum_f Q_f^2 \left\{ 1 + \sum_{n \geq 1} d_n \Phi \left[\left(\frac{\alpha_s(Q^2)}{\pi} \right)^n \right] \right\} , \quad (1.57)$$

where the coefficients d_n are the same as in Eq. (1.46). Eq. (1.57) is to be compared with the standard perturbative expansion (1.48); here the π^2 -terms are entirely summed up, with the drawback that, within this framework, there is no uniquely defined expansion parameter. However, it is useful to work out its behavior to $\mathcal{O}(\alpha_s)$ for $R(s)$, namely

$$\tilde{\alpha}^{(1)}(s) \equiv \Phi [\alpha_s^{(1)}(Q^2)] = \frac{1}{\beta_0} \left\{ \frac{1}{2} - \frac{1}{\pi} \arctan \left[\frac{\ln(s/\Lambda^2)}{\pi} \right] \right\} \quad (1.58)$$

easily obtained by applying the integral transformation (1.55) to the 1-loop space-like coupling (1.8). The related time-like coupling (1.58) is free of unphysical singularities at low s (as Eq. (1.51)), and for $s \gg \Lambda^2 e^\pi$ can be expanded into powers of $\pi/\ln(s/\Lambda^2)$

$$\tilde{\alpha}^{(1)}(s) = \frac{1}{\pi\beta_0} \left[\frac{\pi}{\ln(s/\Lambda^2)} - \frac{1}{3} \frac{\pi^3}{\ln^3(s/\Lambda^2)} + \dots \right] , \quad (1.59)$$

Then Eq. (1.59) can be recasted as a power series in the 1-loop space-like coupling

$$\tilde{\alpha}^{(1)}(s) = \alpha_s^{(1)}(s) \left[1 - \frac{\pi^2 b_0^2}{48} \left(\frac{\alpha_s^{(1)}(s)}{\pi} \right)^2 + \dots \right] , \quad (1.60)$$

emphasizing that the space-like and time-like couplings differ at 3-loop level. The comparison between Eq. (1.60) and Eqs. (1.48) and (1.49) makes it clear the RKP resummation of the π^2 -terms into the time-like coupling (1.58).

The main shortcoming of this recipe is that by applying to Eq. (1.58) the inverse transformation Φ^{-1} , i.e. relation (1.54), the original input (1.8) is not recovered. Obviously, this is because integral transformations (1.55) and its inverse are well-behaved as long as the integrand possesses the correct analytical properties in the cut complex plane; actually this is not the case for the space-like coupling (1.8) and its higher-loop approximations, and one is then forced to compute the integral along a path large enough to avoid the IR space-like singularities.

Chapter 2

The APT theoretical scheme

2.1 The “Euclidean” ghost-free coupling

The analytic approach constitutes the next step, after the RG-summation, in improving the perturbative results. Specifically, in addition to the property of renormalizability, this method retains a general feature of local QFT, the property of causality. The analytic approach has first been devised in the context of Quantum Electrodynamics [60], and then extended to the QCD case about ten years ago [23]. The basic merits of the analytic approach to QCD are the absence of unphysical singularities of the invariant charge and the enhanced stability of outcoming results with respect to both higher loop corrections and the choice of renormalization scheme [61]. Besides, this method enables one to process the spacelike and timelike data in a congruent way [62]. A fresh review of the analytic approach to QCD and its applications can be found in the paper [63].

Usually, in the framework of RG-improved perturbation theory a QCD observable $D(Q^2)$ of a single argument $Q^2 = -q^2 \geq 0$ (spacelike momentum transfer squared) can be represented as a power series in the strong coupling $\alpha_s(Q^2)$ (cf. Eq. (1.46)):

$$D_{\text{PT}}(Q^2) = 1 + \sum_{n \geq 1} d_n [\alpha_s(Q^2)]^n, \quad (2.1)$$

where d_n are the relevant perturbative coefficients. However, in the IR domain this expansion becomes inapplicable due to the spurious singularities

of the running coupling $\alpha_s(Q^2)$. For example, the 1-loop expression (1.8) possesses both the physical cut along the negative real semiaxis $Q^2 \leq 0$ and the unphysical pole at $Q^2 = \Lambda^2$.

In the framework of the APT, the power series (2.1) for an ‘‘Euclidean’’ observable is replaced [65] by the nonpower expansion

$$D_{\text{APT}}(Q^2) = 1 + \sum_{n \geq 1} d_n \mathcal{A}_n(Q^2) \quad (2.2)$$

over the set of functions

$$\mathcal{A}_n(Q^2) = \int_0^\infty \frac{\rho_n(\sigma)}{\sigma + Q^2} d\sigma. \quad (2.3)$$

Here, the spectral function $\rho_n(\sigma)$ is defined as the discontinuity of the relevant power of the perturbative coupling $\alpha_s(Q^2)$ across the physical cut, namely

$$\rho_n(\sigma) = \frac{1}{\pi} \text{Im}[\alpha_s(-\sigma - i\varepsilon)]^n. \quad (2.4)$$

The APT representation (2.2) for a QCD observable $D(Q^2)$ is free of spurious singularities. Besides, it displays a better stability, in comparison with the perturbative parameterization (2.1), with respect to both, the higher-loop corrections and the choice of the renormalization scheme (see Ref. [63] for details). The first-order function $\mathcal{A}_1(Q^2)$ (2.3) plays the role of the effective Euclidean QCD coupling at a given loop level:

$$\alpha_E(Q^2) \equiv \mathcal{A}_1(Q^2) = \int_0^\infty \frac{\rho_1(\sigma)}{\sigma + Q^2} d\sigma. \quad (2.5)$$

The argument $Q^2 = -q^2 > 0$ now runs over the whole space-like axis, that is, $\alpha_E(Q^2)$ is free of any space-like unphysical singularities by construction; moreover, due to the asymptotically free nature of the perturbative input the spectral integral (2.5) needs no subtractions.

In the 1-loop case this equation can be integrated explicitly [23]

$$\alpha_E^{(1)}(Q^2) = \frac{1}{\beta_0} \left[\frac{1}{\ln(Q^2/\Lambda^2)} + \frac{\Lambda^2}{\Lambda^2 - Q^2} \right]. \quad (2.6)$$

The analytically generated non-perturbative contribution in Eq. (2.6) subtracts the pole in a minimal way, yielding a ghost-free behavior which avoids any adjustable parameter. Furthermore, for $Q^2 > \Lambda^2$ this non-perturbative term in Eq. (2.6) can be rewritten as

$$\Delta_p^{(1)}(Q^2) = -\frac{1}{\beta_0} \sum_1^{\infty} \left(\frac{\Lambda^2}{Q^2} \right)^n, \quad (2.7)$$

namely, as a series of power-suppressed corrections to the 1-loop perturbative coupling (1.8). Since the pure perturbative contribution dominates in the deep UV region, the asymptotic freedom constraint of the invariant coupling is preserved.

On the other hand, Eq. (2.6) exhibits the infrared finite limit $\alpha_E^{(1)}(0) = 1/\beta_0$ (roughly 1.4, if $n_f = 3$). This value turns out to be independent of the QCD scale Λ , and it is also universal with respect to higher-loop corrections, warranting a remarkably stable IR behavior of (2.6).

Obviously the scaling parameter has now to be re-defined as

$$\Lambda^2 = \mu_0^2 \exp \left[-\phi \left(\beta_0 \alpha_s(\mu_0^2) \right) \right], \quad (2.8)$$

where the function ϕ is the formal inverse of (2.6), that is, it satisfies the equation

$$\frac{1}{\phi(x)} + \frac{1}{1 - \exp \phi(x)} = x. \quad (2.9)$$

with $x = \beta_0 \alpha_E^{(1)}$ and $Q^2/\Lambda^2 = \exp \phi(x)$. In a similar way, the beta-function for the 1-loop coupling (2.6) reads [23]

$$\beta_E^{(1)}(x) = -\frac{1}{\phi^2(x)} + \frac{\exp \phi(x)}{[\exp \phi(x) - 1]^2} \quad (2.10)$$

with ϕ again given by Eq. (2.9). Despite the implicit form of (2.10), the symmetry property $\beta_E^{(1)}(x) = \beta_E^{(1)}(1 - x)$ reveals the existence of a IR fixed point at $x = 1$, corresponding to the IR finite limit (see also [66]).

2.2 Two-loop and higher orders

Actually, as discussed in Sec. 1.3, the RG equation for the invariant coupling has no simple exact solution beyond the 1-loop level, and asymptotic expressions are commonly used (Eq. (1.32)), with a cumbersome IR nonanalytical

structure. As a result, the spectral functions (2.4) become rather involved. At the 2-loop level, as already pointed out, to get the most accurate result in the IR domain, one needs to start with the exact RG solution as given by Eq. (1.24). In the framework of APT, this amounts to consider the discontinuity of (1.24) across the time-like cut [67, 66]

$$\rho_{ex}^{(2)}(\sigma) = \frac{1}{\pi} \text{Im} [\alpha_{ex}^{(2)}(-\sigma)] , \quad (2.11)$$

and the exact 2-loop analytic coupling then reads

$$\alpha_E^{(2)}(z) = \int_{-\infty}^{\infty} dt \frac{e^t}{e^t + z} \bar{\rho}_{ex}^{(2)}(t) \quad (2.12)$$

where $t = \ln(\sigma/\Lambda^2)$ and $z = Q^2/\Lambda^2$. In spite of its accuracy, Eq. (2.12) cannot be easily handled, and a slightly simpler expression can be obtained starting from the 2-loop iterative solution (1.27) which turns out to be a better approximation to the exact solution than the usual Eq. (1.30), as far as the IR domain is concerned (see Sec. 1.3). The related spectral density is then given by [23]

$$\rho_{it}^{(2)}(\sigma) = \frac{1}{\pi} \text{Im} \alpha_{it}^{(2)}(-\sigma) = \frac{1}{\pi\beta_0} \frac{I(t)}{I^2(t) + R^2(t)} \quad t = \ln(\sigma/\Lambda^2) \quad (2.13)$$

$$I(t) = \pi + B_1 \arccos \frac{B_1 + t}{\sqrt{(B_1 + t)^2 + \pi^2}}, \quad R(t) = t + B_1 \ln \frac{\sqrt{(B_1 + t)^2 + \pi^2}}{B_1}$$

that can be integrated numerically. Moreover, since the singularity structure of Eq. (1.27) is entirely removed by analytization, the iterative 2-loop analytic coupling can be straightforwardly obtained by merely adding to (1.27) two compensating terms, that cancel respectively the pole and the cut [61]

$$\alpha_{E,it}^{(2)}(z) = \alpha_{it}^{(2)}(z) + \Delta_p^{(2)} + \Delta_c^{(2)} \quad (2.14)$$

$$\Delta_p^{(2)}(z) = \frac{1}{2\beta_0} \frac{1}{1-z}$$

$$\Delta_c^{(2)}(z) = \frac{1}{\beta_0} \int_0^{\exp(-B_1)} \frac{d\xi}{\xi - z} \frac{B_1}{[\ln \xi + B_1 \ln(-1 - B_1^{-1} \ln \xi)]^2 + \pi^2 B_1^2}$$

with $\xi = \sigma/\Lambda^2$. From Eqs. (2.14) one can readily verify the IR limit $\alpha_{E,it}^{(2)}(0) = 1/\beta_0$; for general arguments concerning the universality of the freezing value

through all orders see for instance [61, 68] and [69].

An useful property of the 2-loop coupling (2.14) is the possibility to estimate its non-perturbative UV tail by expanding the two compensating terms into a power series of $1/z = \Lambda^2/Q^2$ for large z [70], in a way similar to Eq. (2.7), namely

$$\Delta_p^{(2)}(z) + \Delta_c^{(2)}(z) = \frac{1}{\beta_0} \sum_{n=1}^{\infty} \frac{c_n}{z^n} \quad (2.15)$$

$$c_n = -\frac{1}{2} - \int_0^{\infty} d\xi \frac{\exp[-nB_1(1+\xi)]}{(1+\xi - \ln \xi)^2 + \pi^2}.$$

If $n_f = 6$ is taken, the first coefficient, e.g., in Eq. (2.15) turns out to be $c_1 \simeq -0.54$. A numerical comparison between Eqs. (2.14) and (2.12), performed in [66] (see Tab.1), reveals that they differ of about 1.8% in the IR region.

Increasing difficulties arise when dealing with even higher-loop levels. Indeed, the exact 3- and 4-loop spectral densities (2.4) have a rather cumbersome structure in terms of the Lambert function. Nevertheless, an extensive numerical study of the analytic coupling (2.5) and its “effective powers” (2.3) up to 4-loop can be found in Ref. [42]. This analysis reveals that the exact 3-loop spectral density can be approximated to a high accuracy ($\sim 1\%$) by the discontinuity of the 3-loop perturbative coupling (as deduced by Eq. (1.32)) across the physical cut [71]:

$$\rho_1^{(3)}(\sigma) = \frac{1}{\beta_0} \frac{1}{(t^2 + \pi^2)^3} [t(3\pi^2 - t^2)J(t) - (3t^2 - \pi^2)R(t)]. \quad (2.16)$$

In this equation $t = \ln(\sigma/\Lambda^2)$,

$$\begin{aligned} J(t) &= 2t - B_1[tG_1(t) + G_2(t)] + B_1^2 G_1(t)[2G_2(t) - 1], \\ R(t) &= t^2 - \pi^2 - B_1[tG_2(t) - \pi^2 G_1(t)] + \\ &\quad B_1^2[G_2^2(t) - \pi^2 G_1^2(t) - G_2(t) - 1] + B_2, \\ G_1(t) &= \frac{1}{2} - \frac{1}{\pi} \arctan\left(\frac{t}{\pi}\right), \quad G_2(t) = \frac{1}{2} \ln(t^2 + \pi^2) \end{aligned} \quad (2.17)$$

with $B_j = \beta_j/\beta_0^{j+1}$ and β_j the expansion coefficients (1.17) of β function. The 4-loop analogue of Eqs. (2.16) and (2.17) turns out to be more involved

but of small usefulness, being the difference with respect to the 3-loop approximation negligible [63]. In Fig. 2.1 the analytic coupling up to 4-loop is compared to the perturbative counterpart.

One can then argue that the 3-loop analytic coupling obtained by integration of the spectral density (2.16), namely

$$\alpha_E^{(3)}(Q^2) = \int_0^\infty \frac{\rho_1^{(3)}(\sigma)}{\sigma + Q^2} d\sigma, \quad (2.18)$$

is a satisfactory improvement of the 1-loop result (2.6) for all practical aims. By normalizing Eq. (2.18) at the Z boson mass to the world average value $\alpha_s(M_Z^2) = 0.1176 \pm 0.0020$ [2], one finds $\Lambda_{n_f=5}^{(3)} \simeq 236$ MeV. Evolution at the crossing of heavy quark thresholds by continuous matching conditions then gives $\Lambda_{n_f=3}^{(3)} \simeq 417$ MeV. Eq. (2.18) with the spectral density given by Eqs. (2.16) and (2.17) is actually the expression used in the following analysis (see Sec. 3) for the comparison with the experimental values of the QCD coupling extracted from the Bethe-Salpeter approach.

Moreover, it should be noted that an integral representation, similar to Eq. (2.14) (and also Eq. (2.15)), of the non-perturbative terms accounting for the divergencies of the 3-loop asymptotic solution (1.32) (that is the leading singularity in $z = 1$ (1.40), and the IR log-of-log generated cut) also exists [70, 69]. It turns out [69] that the asymptotic behavior of $\alpha_E^{(3)}(Q^2)$ defined by Eq. (2.18), i.e. in the large Q^2 limit, is given by

$$\bar{\alpha}_E^{(3)}(z) \simeq \alpha_s^{(3)}(z) + \frac{1}{\beta_0} c_1 \frac{\Lambda^2}{Q^2} \quad (2.19)$$

$$c_1 = -1 + B_1(1 - \gamma_E) - \frac{B_1^2}{2} \left[B_2 - \frac{\pi^2}{6} + (1 - \gamma_E)^2 \right].$$

Here γ_E is the Euler constant, $B_2 = \beta_0\beta_2/\beta_1^2$, $\alpha_s^{(3)}(z)$ is the perturbative counterpart as given by (1.32), and $c_1 \simeq -0.52$ if $n_f = 6$ (see Ref. [69] for details).

Note finally that in Refs. [42, 43] high-accuracy 3- and 4-loop analytic coupling of the form

$$\alpha_E^{(k)}(Q^2) = \sum_{n \geq 1} p_n^{(k)} \left[\alpha_E^{(2)}(Q^2) \right]^n \quad (2.20)$$

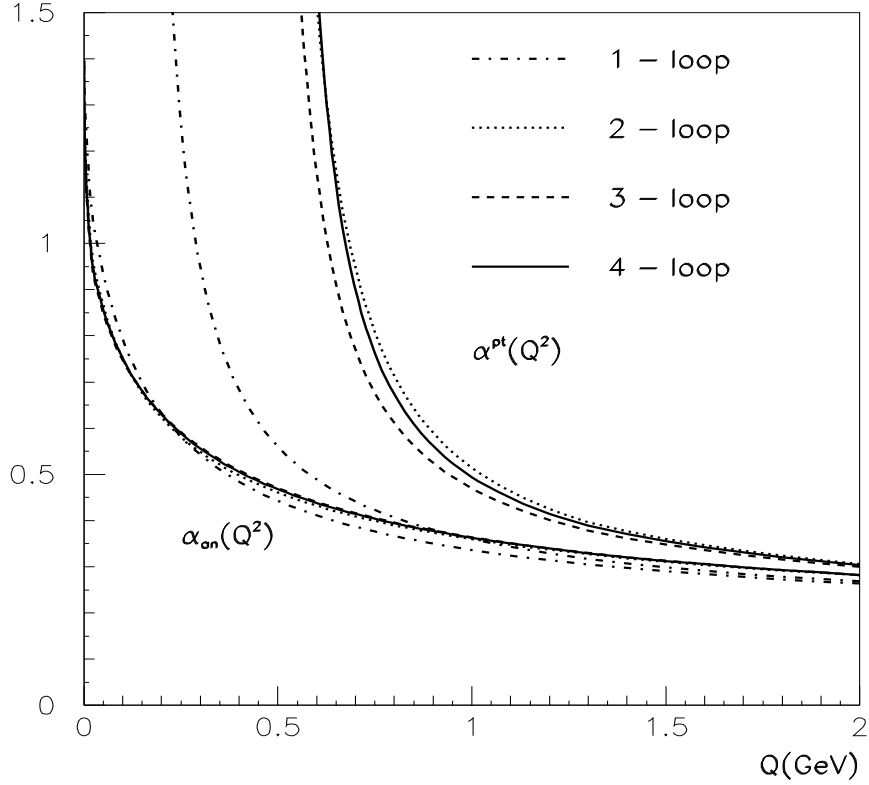


Figure 2.1: Analytic coupling taken from [69] up to 4-loop compared to perturbative counterparts (1.32).

has been also worked out, by exploiting the multi-loop approximation (1.33) as an input in the dispersion relation (2.5). Here $\alpha_E^{(2)}$ is given by Eq. (2.12) and the coefficients are the same as in (1.33). Numerical values at low scales can be found in [42].

For practical applications, one can even resort to simple expressions of the form of Eq. (2.6), with a special model argument. According to Ref. [72], the 3-loop Euclidean coupling can be approximated with reasonable accuracy by the “1-loop-like” model

$$\alpha_{\text{appr}}^{(3)}(Q^2) = \frac{1}{\beta_0} \left[\frac{1}{L_2(Q^2)} + \frac{1}{1 - \exp[L_2(Q^2)]} \right], \quad (2.21)$$

where

$$L_2(Q^2) = \ln\left(\frac{Q^2}{\Lambda^2}\right) + B_1 \ln \sqrt{\ln^2\left(\frac{Q^2}{\Lambda^2}\right) + 2\pi^2}, \quad B_1 = \frac{\beta_1}{\beta_0^2}. \quad (2.22)$$

The relative difference between the exact 3-loop analytic coupling (numerically evaluated via the Lambert function) and its approximation (2.21) is less than 3% for $Q \geq 500$ MeV (see Table 1 in Ref. [72] for the details). However, this error could reach 5-10% below 500 MeV and it is then unuseful in the deep IR domain. In this region the more precise expression (2.18) should be used. Moreover, its accuracy in the asymptotic region breaks down when taking into account flavor thresholds. Therefore, it has been suggested [73] to use Eqs. (2.21) and (2.22) provided that the scaling constant and the coefficient B_1 are replaced by adjustable parameters (see tab. III in Ref. [73]). This yields an accuracy within 1% in the whole space-like region down to $Q \geq 1$ GeV.

2.3 The “Minkowskian” domain in APT

As far as the definition of a reasonable expansion parameter in the time-like domain ($q^2 = s > 0$) is concerned, it should be noted that such a definition naturally arises in a self-consistent way within the framework of APT [74, 75]. Further, it can be regarded as the final step in the RKP-resummation for π^2 -terms outlined in Sec 1.6.

As already noted, Eq. (1.54) and its formal inverse (1.55) can be generalized to the proper tool for relating s- and t-channel observables. In the APT scheme, a standard power expansion for a space-like observables (2.1) is replaced by a nonpower one (2.2). A time-like observables, in turn, within this framework, can be also re-expressed as the nonpower expansion

$$R_{\text{APT}}(s) = 1 + \sum_{n \geq 1} d_n \mathfrak{A}_n(s) \quad (2.23)$$

over the set of functions

$$\mathfrak{A}_n(s) = \int_s^\infty \frac{d\sigma}{\sigma} \rho_n(\sigma), \quad (2.24)$$

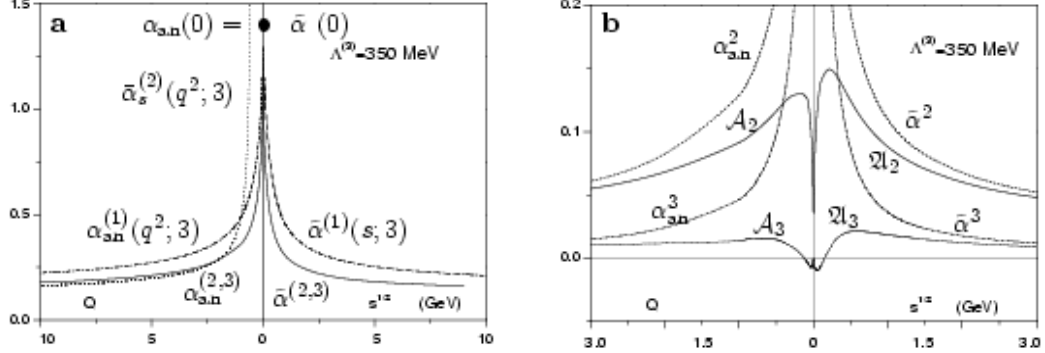


Figure 2.2: (a) Space-like and time-like global analytic couplings in a few GeV domain with $n_f = 3$ and $\Lambda = 350$ MeV; (b) “Distorted mirror symmetry” for global expansion functions, corresponding to exact 2-loop solutions.

where the n -th spectral density ρ_n is again given by Eq. (2.4). This recipe is manifestly quite analogous to the RKP non-power expansion (1.57). The key point here [76] is that, due to the forced analyticity of the coupling and its analytized powers (2.3), the two sets (2.3) and (2.24) are put into a one-to-one relation by the linear integral transformations (1.54) and (1.55), namely

$$\mathcal{A}_n(Q^2) = \mathbf{D}[\mathfrak{A}_n(s)], \quad \text{and} \quad \mathfrak{A}_n(s) = \mathbf{R}[\mathcal{A}_n(Q^2)]. \quad (2.25)$$

This eventually yields a closed theoretical scheme for representing observables of any real argument, both space-like and time-like (for technicalities see [77]).

The main features of the two functional sets are illustrated in Fig. 2.2 taken from [77]. For $n \geq 2$ both sets \mathcal{A}_n and \mathfrak{A}_n start with an IR zero and oscillate in the IR domain around $n - 1$ zeros; furthermore, they all display the UV asymptotic behavior $1/\ln^n z$, resembling the corresponding powers $\alpha_s^n(z)$. The recursion relations [72]

$$\frac{1}{n} \frac{d\mathcal{A}_n^{(l)}(Q^2)}{d \ln Q^2} = - \sum_{j=1}^l \beta_{j-1} \mathcal{A}_{n+j}^{(l)}(Q^2), \quad \frac{1}{n} \frac{d\mathfrak{A}_n^{(l)}(s)}{d \ln s} = - \sum_{j=1}^l \beta_{j-1} \mathfrak{A}_{n+j}^{(l)}(s), \quad (2.26)$$

where l is the loop level, allow one to relate different analytized powers within each set, albeit explicit expressions are available in a simple form only at 1-loop (see e.g. [72]). Nonetheless, the two sets (2.3) and (2.24) have been numerically evaluated for $n = 1, 2, 3$ in [67] up to 3-loop, via the Lambert

function (see also [42] and [43]). Furthermore, a generalization of APT to fractional powers of α_s was also implemented in Ref. [78].

As in the space-like domain, the first function of Eq. (2.24) plays the role of the effective coupling of time-like argument, namely

$$\alpha_M(s) = \int_s^\infty \frac{d\sigma}{\sigma} \rho_1(\sigma). \quad (2.27)$$

Note also that $\alpha_M(s)$ can be equally defined by the differential equation [11]

$$s \frac{d}{ds} \alpha_M(s) = -\rho_1(s) \quad \text{with} \quad \tilde{\alpha}(\infty) = 0, \quad (2.28)$$

as can be verified by differentiating the second of Eq. (2.25) with $n = 1$, i.e. ¹

$$\alpha_M(s) = \frac{i}{2\pi} \int_{s-i\varepsilon}^{s+i\varepsilon} \frac{dQ^2}{Q^2} \alpha_E(Q^2). \quad (2.29)$$

Moreover, Eq. (2.28) emphasizes the straightforward relation between the “time-like β -function” and the spectral density, thus reviving an old hypothesis due to Schwinger [79].

At 1-loop from Eq. (2.27) one finds again Eq. (1.58); however this now leads by inversion of Eq. (2.29) to the starting space-like coupling (2.6), being the analytic properties preserved within this framework.

The main feature [74] of Eqs. (2.27) and (2.5) is the common IR freezing value $\tilde{\alpha}(0) = \alpha_E(0) = 1/\beta_0$, independent of the loop level and of any adjustable parameter (see Fig. 4(a)). Moreover, they exhibit a similar leading UV behavior, constrained by asymptotic freedom. Nevertheless this approximate “mirror symmetry” is broken in the intermediate energy region ², the discrepancy being about 9% at 1-loop, and slightly less at a higher loop level (see Ref. [74] for numerical comparisons).

A last remark concerns thresholds effects, that can be included within the APT algorithm [76] by modifying the n -th spectral density (2.4) discontinuously at the heavy quark thresholds m_f , namely

$$\rho_n(\sigma) = \rho_n(\sigma, 3) + \sum_{n_f \geq 4} \theta(\sigma - m_f^2) [\rho_n(\sigma, n_f) - \rho_n(\sigma, n_f - 1)], \quad (2.30)$$

¹Note that this definition for the time-like coupling had been suggested also in [59, 74].

²In Ref. [80] an argument, on the basis of causality principle, against a possible exact symmetry ruling the “t-s dual” couplings, has been developed.

descending from the trivial matching condition (Sec. 1.4). The global functions resulting from densities (2.30), \mathcal{A}_n and \mathfrak{A}_n , can be obtained from the local ones with n_f fixed, by adding specific shift constants $c_n(n_f)$, not negligible in the $n_f = 3, 4$ region (technical details are given in [76]; for instance, in both the t- and s-channels it turns out $c_1(3) \simeq 0.02$).

The main tests of APT being obviously at low and intermediate scales, a number of applications to specific processes, both in the space-like and time-like (low and high energy) domains, have been quite recently performed (see for instance, Refs. [81, 72, 75, 61, 77, 73]). As a result, the main advantages of the APT approach are better convergence properties of the ghost-free non-power expansion with respect to the usual power one, and a reduced scheme and loop-dependence.

Finally, transition from Euclidean (space-like momentum) to the distance picture has been also developed in [82], involving a suitable modified sine-Fourier transformation, consistently with the APT logic.

2.4 Modifications of APT and the massive case

Different strategies to incorporate analyticity into the RG formalism, or even to implement the above device, exist as well. A number of approaches are based on non-perturbative constraints either on the invariant coupling (see e.g. Refs. [83, 84, 85]) or on the RG β function (see, e.g., Refs. [86, 71, 87] and also [88, 39]).

Among the many attempts to cure the Landau ghost problem it is remarkable the existence of models that suggest an IR enhancement of the QCD coupling, invoking analyticity as well. The most attractive feature is supposed to be a straightforward relation with quark confining potential (see Sec. 1.1). As an example, it can be reminded the ‘‘synthetic coupling’’ model recently developed in [85], which amounts to modify the analytically improved coupling (2.5) by additional non-perturbative pole-type terms; at 1-loop it reads

$$\alpha_{\text{syn}}(Q^2) = \frac{1}{\beta_0} \left[\frac{1}{\ln(Q^2/\Lambda^2)} + \frac{\Lambda^2}{\Lambda^2 - Q^2} + \frac{c\Lambda^2}{Q^2} + \frac{(1-c)\Lambda^2}{Q^2 + m_g^2} \right]. \quad (2.31)$$

where $m_g = \Lambda/\sqrt{c-1}$. The IR slavery, due to the pole term at $Q^2 = 0$, is controlled by one dimensionless parameter $c \in (1, \infty)$, which relates the

scaling constant Λ to the string tension σ of potential models (cf. Eq. (1.12)). The pole term at $Q^2 = -m_g^2 < 0$ corresponds to a non vanishing "dynamical" gluon mass, while leaving the analytical structure of eq.(2.6) along the space-like axis unchanged. The value of the m_g parameter has been estimated [85] as 400 – 600 MeV. Eq. (2.31) can be derived, analogously to (2.6), from a dispersion relation with a spectral density of the form (2.4) plus two δ -terms properly accounting for the poles. Along with the IR enhancement as $1/Q^2$, reproducing the linear confining part of the potential (1.12), construction of (2.31) is mainly motivated by the UV asymptotic behavior of its non-perturbative contribution, of the form $1/(Q^2)^3$, decreasing faster than (2.7) as $Q^2 \rightarrow \infty$ (see also [89]).

Actually, of some relevance to the following analysis (see Sec. 3), in particular, as far as the deep IR behavior of the QCD coupling is concerned (i.e. below 200 MeV), is the "massive" modification of the APT approach recently developed in [90]. In order to handle the QCD observables which do not satisfy the integral representation of the form of Eq. (2.3), the APT formalism has to be modified appropriately, by taking into account the effect of a non-vanishing mass threshold m in the dispersion relations. In this case the set of APT expansion functions (2.3) should be replaced by the set of "massive" ones with an adjustable parameter m

$$A_n(Q^2, m^2) = \frac{Q^2}{Q^2 + 4m^2} \int_{4m^2}^{\infty} \rho_n(\sigma) \frac{\sigma - 4m^2}{\sigma + Q^2} \frac{d\sigma}{\sigma}. \quad (2.32)$$

The APT expansion (2.2) should be then replaced by

$$D_{\text{MAPT}}(Q^2, m^2) = \frac{Q^2}{Q^2 + 4m^2} + \sum_{n \geq 1} d_n A_n(Q^2, m^2). \quad (2.33)$$

Obviously, in the massless limit Eqs. (2.33) and (2.32) coincide with the expressions (2.2) and (2.3), respectively.

Similarly to the case of Eq. (2.5) in the "massless" APT, the first-order function $A_1(Q^2, m^2)$ (2.32) plays the role of an effective "massive" running coupling at the relevant loop level, namely

$$\alpha(Q^2, m^2) \equiv A_1(Q^2, m^2) = \frac{Q^2}{Q^2 + 4m^2} \int_{4m^2}^{\infty} \rho_1(\sigma) \frac{\sigma - 4m^2}{\sigma + Q^2} \frac{d\sigma}{\sigma}. \quad (2.34)$$

It is worthwhile to note that irrespective of the loop level this coupling possesses the universal IR limiting value $\alpha(Q^2, m^2) \rightarrow 0$ at $Q^2 = 0$, in qualitative agreement with some results from lattice simulations [17, 16] (see Ref. [90] for details). Moreover, as discussed in Sec. 3, the IR behavior of the QCD coupling, in particular below 200 MeV, extracted from the meson spectrum in BS formalism, can be reasonably described within this “massive” modification of APT, that is, by Eq. (2.34) if a proper value of the adjustable parameter m is chosen.

Chapter 3

Bound states approach

3.1 QCD coupling from the meson spectrum

Below 1 GeV, as discussed in Sec. 1, the running coupling α_s is affected at any loop level by unphysical singularities that make the RG-improved pQCD useless.

In order to shed some light on the QCD coupling below this scale, one needs experimental information to be extracted with the aid of a suitable theoretical framework. The latter can be provided by the Bethe-Salpeter (BS) formalism developed in [24] for the study of the meson spectrum, since the scale involved (the momentum transfer in the $q\bar{q}$ interaction) is typically below 1 GeV. Many relativistic formalisms for the analysis of the meson properties have been developed in the context of QCD, that take confinement into account and evaluate the meson (and baryon) spectrum in the light and heavy quark sectors. Among the most recent works, one should remind for instance Refs. [25, 26, 27, 28, 91, 92, 93] and references therein.

In the present work the theoretical results on the meson spectrum within the framework of a Bethe-Salpeter (BS) formalism adjusted for QCD, have been exploited with the aim of extracting “experimental” values of the running coupling $\alpha_s^{\text{exp}}(Q^2)$ below 1 GeV by comparison with the data.

The *second order* BS formalism, developed in [24] and applied to the calculation of a rather complete quarkonium spectrum in Refs. [94, 95], is essentially derived from the QCD Lagrangian taking advantage of a Feynman-Schwinger

representation for the solution of the iterated Dirac equation in an external field. Confinement is encoded through an ansatz on the Wilson loop correlator (see Ref. [24] for details); indeed the expression $i \ln W$ is written as the sum of a one-gluon exchange (OGE) and an area terms

$$i \ln W = (i \ln W)_{\text{OGE}} + \sigma S . \quad (3.1)$$

By means of a three dimensional reduction, the original BS equation takes the form of the eigenvalue equation for a squared bound state mass

$$M^2 = M_0^2 + U_{\text{OGE}} + U_{\text{Conf}} , \quad (3.2)$$

where M_0 is the kinematic term $M_0 = w_1 + w_2 = \sqrt{m_1^2 + \mathbf{k}^2} + \sqrt{m_2^2 + \mathbf{k}^2}$, \mathbf{k} being the c.m. momentum of the quark, m_1 and m_2 the quark and the antiquark constituent masses, and $U = U_{\text{OGE}} + U_{\text{Conf}}$ the resulting potential. As a consequence of ansatz (3.1), the perturbative part of the potential U_{OGE} turns out to be proportional to $\alpha_s(Q^2)$, that should be regularized with a proper prescription.

Calculations have been performed in Refs. [94, 95] by using both a frozen and the 1-loop analytic coupling $\alpha_E^{(1)}(Q^2)$ as given by Eq. (2.6) with an effective scaling parameter $\Lambda_{n_f=3}^{(1,\text{eff})} \simeq 200 \text{ MeV}$.

The results of the two sets of calculations are relatively similar for the heavy-heavy quark states. However, for the 1S states involving light and strange quarks, quite different results have been obtained in the two cases. In the case of a frozen coupling the π and K masses turn out to be too high, irrespective of how small the light quark mass is taken (see Fig. 3.1); e.g., if the light and the strange quark masses are fitted to the ρ and the ϕ masses, one finds $m_\pi \sim 500 \text{ MeV}$ and $m_K \sim 700 \text{ MeV}$, respectively. On the contrary, if appropriate values for the quark masses are chosen, the π , ρ , K , K^* , ϕ masses can be rather well reproduced when the analytic coupling $\alpha_E^{(1)}(Q^2)$ is used. This occurrence strongly supports the use of the APT prescription, outlined in Sec. 2, within BS framework.

Indeed, the combined BS-APT theoretical scheme provides a substantial agreement of the calculated spin averaged c.o.g. masses with the data throughout the whole calculable spectrum, and in particular the correct splittings 1^3S_1 - 1^1S_0 is well reproduced at least in the light-light, light-strange and heavy-heavy sectors.

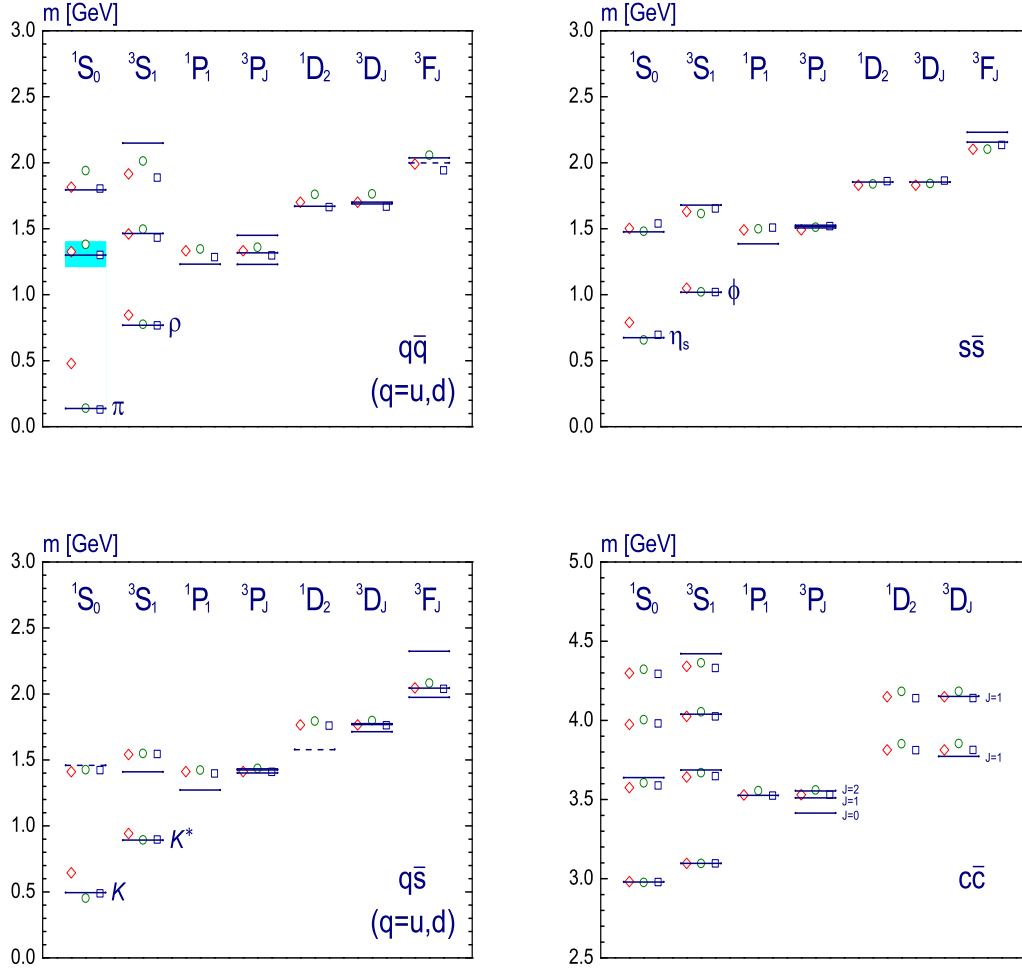


Figure 3.1: Quarkonium spectrum, three different calculations. Diamonds refer to the truncation prescription for the running coupling, squares and circles refer to the calculation with the 1-loop APT coupling (2.6) and two different expressions for running constituent masses of light quarks, a solution of the Dyson-Schwinger equation and a phenomenological function of the c.m. quark momentum respectively. Horizontal lines represent experimental data.

In this work a thorough analysis has been undertaken from the reversed point of view, that is by comparing theoretical results of the meson spectrum within the BS approach, obtained for a definite choice of the parameters, with the results of a similar calculation performed by means of a fixed value of α_s , for every quark-antiquark state. In what follows α_s^{th} denotes the value that reproduces the same theoretical result as by using $\alpha_E^{(1)}(Q^2)$, whereas α_s^{exp} the value that correctly reproduces the experimental mass. The value α_s^{th} is clearly an intermediate step object, used to identify an effective Q pertaining to each meson state, to be understood as the argument of the related “experimental” coupling $\alpha_s^{\text{exp}}(Q^2)$.

Since only the leading perturbative contribution in the BS kernel has been included, a rough estimate of NLO effects on the extracted α_s^{exp} values leads to a relative theoretical error which spans from 20% to much less than 1% throughout the spectrum, according to the quark masses involved. Furthermore, since coupling among different quark-antiquark channels has not been taken into account within BS formalism, the theoretical masses are expected to reproduce the experimental ones roughly within the half width $\Gamma/2$ of the state. If relevant, the experimental error, related to the uncertainty of the experimental masses, is added to the theoretical one.

The results are twofold. On the one hand, the 3-loop APT coupling, normalized at the world average $\alpha_s(M_Z^2) = 0.1176(20)$ and evolved across heavy quark thresholds, reasonably fits $\alpha_s^{\text{exp}}(Q^2)$ from 1 GeV down to 200 MeV, quantitatively confirming the relevance of the APT approach to IR phenomena down to 200 MeV. On the other hand, below this scale, with the limitation due to the large errors, the experimental points give a wee hint about the vanishing of $\alpha_s(Q^2)$ as $Q \rightarrow 0$. This could correlate with some results from lattice simulations [17], and can be theoretically discussed in the framework of a recent “massive” modification [90] of APT (see Sec. 2.4) which takes into account effects of a finite threshold in the dispersion relation ¹.

¹It should be noted, however, that the existence of a non vanishing finite limit lower than the universal Shirkov-Solovtsov freezing value, as suggested in [27], is still consistent with the above results.

3.2 BS-model for quarkonium states

As mentioned, in [94, 95] the meson spectrum is obtained by solving the eigenvalue equation for the squared mass operator (3.2), where the perturbative and the confinement parts of the potential are respectively

$$\begin{aligned}
\langle \mathbf{k} | U_{\text{OGE}} | \mathbf{k}' \rangle = & \\
& \frac{4}{3} \frac{\alpha_s(\mathbf{Q}^2)}{\pi^2} \sqrt{\frac{(w_1 + w_2)(w'_1 + w'_2)}{w_1 w_2 w'_1 w'_2}} \left[-\frac{1}{\mathbf{Q}^2} \left(q_{10} q_{20} + \mathbf{q}^2 - \frac{(\mathbf{Q} \cdot \mathbf{q})^2}{\mathbf{Q}^2} \right) \right. \\
& + \frac{i}{2\mathbf{Q}^2} \mathbf{k} \times \mathbf{k}' \cdot (\sigma_1 + \sigma_2) + \frac{1}{2\mathbf{Q}^2} [q_{20}(\alpha_1 \cdot \mathbf{Q}) - q_{10}(\alpha_2 \cdot \mathbf{Q})] + \\
& \left. + \frac{1}{6} \sigma_1 \cdot \sigma_2 + \frac{1}{4} \left(\frac{1}{3} \sigma_1 \cdot \sigma_2 - \frac{(\mathbf{Q} \cdot \sigma_1)(\mathbf{Q} \cdot \sigma_2)}{\mathbf{Q}^2} \right) + \frac{1}{4\mathbf{Q}^2} (\alpha_1 \cdot \mathbf{Q})(\alpha_2 \cdot \mathbf{Q}) \right] \quad (3.3)
\end{aligned}$$

and

$$\langle \mathbf{k} | U_{\text{Conf}} | \mathbf{k}' \rangle = \frac{\sigma}{(2\pi)^3} \sqrt{\frac{(w_1 + w_2)(w'_1 + w'_2)}{w_1 w_2 w'_1 w'_2}} \int d^3 \mathbf{r} e^{i\mathbf{Q} \cdot \mathbf{r}} J^{\text{inst}}(\mathbf{r}, \mathbf{q}, q_{10}, q_{20}) \quad (3.4)$$

with

$$\begin{aligned}
J^{\text{inst}}(\mathbf{r}, \mathbf{q}, q_{10}, q_{20}) = & \frac{r}{q_{10} + q_{20}} \left[q_{20}^2 \sqrt{q_{10}^2 - \mathbf{q}_\perp^2} + q_{10}^2 \sqrt{q_{20}^2 - \mathbf{q}_\perp^2} + \right. \\
& \left. + \frac{q_{10}^2 q_{20}^2}{|\mathbf{q}_\perp|} \left(\arcsin \frac{|\mathbf{q}_\perp|}{q_{10}} + \arcsin \frac{|\mathbf{q}_\perp|}{q_{20}} \right) \right] \\
& - \frac{1}{r} \left[\frac{q_{20}}{\sqrt{q_{10}^2 - \mathbf{q}_\perp^2}} (\mathbf{r} \times \mathbf{q} \cdot \sigma_1 + i q_{10} (\mathbf{r} \cdot \alpha_1)) \right. \\
& \left. + \frac{q_{10}}{\sqrt{q_{20}^2 - \mathbf{q}_\perp^2}} (\mathbf{r} \times \mathbf{q} \cdot \sigma_2 - i q_{20} (\mathbf{r} \cdot \alpha_2)) \right]. \quad (3.5)
\end{aligned}$$

Here α_j^k denote the usual Dirac matrices $\gamma_j^0 \gamma_j^k$, σ_j^k the 4×4 Pauli matrices $\begin{pmatrix} \sigma_j^k & 0 \\ 0 & \sigma_j^k \end{pmatrix}$ and $\mathbf{q} = \frac{\mathbf{k} + \mathbf{k}'}{2}$, $\mathbf{Q} = \mathbf{k} - \mathbf{k}'$, $q_{j0} = \frac{w_j + w'_j}{2}$, m_1 and m_2 are constituent masses.

Eqs. (3.3-3.5) have been derived from the ansatz (3.1) and a 3-dimensional

reduction of a Bethe-Salpeter like equation (see Refs. [24, 94, 95] and App. A for the details). Actually in the calculation of Refs. [94, 95] only the center of gravity (c.o.g.) masses of the fine multiplets were considered as a rule, and the spin dependent terms in (3.3-3.5) (spin-orbit and tensorial terms) were neglected with the exception of the hyperfine separation term in (3.3), proportional to $\frac{1}{6}\sigma_1 \cdot \sigma_2$. Within this limitation, a generally good reproduction of the spectrum was obtained for appropriate values of the parameters, as shown in Fig. 3.1. Here the results of three sets of calculations are displayed. Diamonds refer to the usual perturbative 1-loop coupling (to be replaced in Eq. (3.3)), frozen at a maximum value H , which has been taken as an additional adjustable parameter. Squares and circles both refer to the 1-loop APT coupling (2.6) with $\Lambda \simeq 200$ MeV. For light quarks a running constituent mass was used too.²

It should be stressed that only with the choice (2.6) the 1^1S_0 state has been correctly reproduced when light and strange quarks were involved, as in the case of π and the K mesons.

In the present work [3, 4] a similar calculation with the input (2.6) and a slight different choice of the parameters is made (preliminary results were given in [96]). First, the string tension has been fixed a priori to the value $\sigma = 0.18$ GeV² (consistent with hadron phenomenology and lattice simulations) and the scale constant to $\Lambda_{n_f=3}^{(1,\text{eff})} = 193$ MeV. The whole set of remaining parameters, all the quark masses, are then determined by fitting the π , ϕ , J/ψ and Υ masses. It turns out $m_u = m_d = 196$ MeV, $m_s = 352$ MeV, $m_c = 1.516$ GeV and $m_b = 4.854$ GeV. The results for the meson spectrum are given in the fourth column of the tables in App. B.

The effective value for the QCD scale $\Lambda_{n_f=3}^{(1,\text{eff})}$ has been dictated by the comparison with the 3-loop analytic coupling normalized at the Z boson mass (see Eqs. (2.16,2.17) and (2.18)) according to the world average. As displayed in Fig. 3.2, the relative difference between the two curves is no more than 1% in the region of momentum transfer $0.5 < Q < 1.2$ GeV, to which the bulk of the states used as an input in the calculation belongs.

Furthermore, as already noted, the set of equations (3.3-3.5) refer to a single definite quark-antiquark channels. So, having correct relativistic kinematics,

²Circles refer to a phenomenological running mass as function of the c.m. quark momentum $m_u^2 = m_d^2 = 0.17|\mathbf{k}| - 0.025|\mathbf{k}|^2 + 0.15|\mathbf{k}|^4$. Squares refer to a running constituent mass resulting from a solution of the Dyson-Schwinger equation with an analytic RG running current mass (see App. A for some details).

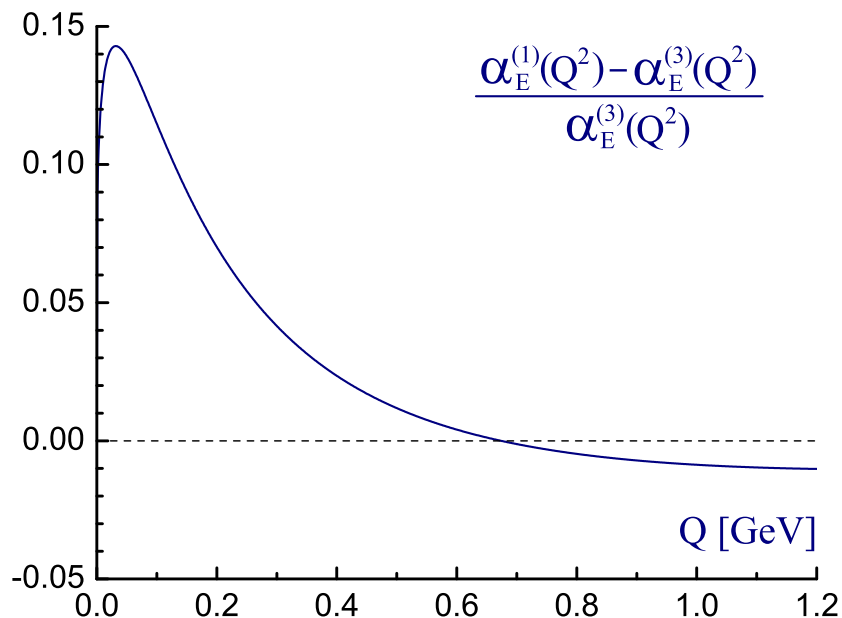


Figure 3.2: Relative difference between the one-loop analytic running coupling $\alpha_E^{(1)}(Q^2)$ with $\Lambda_{n_f=3}^{(1,\text{eff})} = 193 \text{ MeV}$ and three-loop $\alpha_E^{(3)}(Q^2)$ with $\Lambda_{n_f=3}^{(3)} = 417 \text{ MeV}$ in the range $0 < Q < 1.2 \text{ GeV}$.

they do not include coupling with other channels like any potential model (see App. A). Therefore, one can not expect to have any insight into the splitting of over-threshold complicated multiplets which involve mixture of different states. Even the position of the c.o.g. mass is expected to be reproduced only within one-half of the width of the state. This has been taken into account in the estimate of the theoretical error (see Sec. 4).

The resolution method of the eigenvalue equation for the operator (3.2, 3.3-3.5) used in [94, 95] and in the present work can be summarized as follows.

a) In the static limit the problem can be reduced to the corresponding one for the center of mass Hamiltonian (see App. A)

$$H_{\text{CM}} = w_1 + w_2 - \frac{4}{3} \frac{\alpha_s}{r} + \sigma r. \quad (3.6)$$

b) The eigenvalue equation for (3.6) is solved for a convenient fixed α_s by the Rayleigh-Ritz method, using the three dimensional harmonic oscillator

basis and diagonalizing a 30×30 matrix.

c) The square of the meson mass is evaluated as $\langle \phi_a | M^2 | \phi_a \rangle$, ϕ_a being the eigenfunction obtained in step b) (with a the whole set of quantum numbers) and the operator M^2 given by Eq. (3.2).

d) Prescription c) is equivalent to treat $M^2 - H_{\text{CM}}^2$ as a first order perturbation. Consistently the hyperfine separation should be given by

$$\begin{aligned} ({}^3m_{nl})^2 - ({}^1m_{nl})^2 = & \frac{32}{9\pi} \int_0^\infty dk k^2 \int_0^\infty dk' k'^2 \varphi_{nl}^*(k) \varphi_{nl}(k') \times \\ & \sqrt{\frac{w_1 + w_2}{w_1 w_2}} \sqrt{\frac{w'_1 + w'_2}{w'_1 w'_2}} \int_{-1}^1 d\xi \alpha_s(\mathbf{Q}^2) P_l(\xi), \end{aligned} \quad (3.7)$$

where φ_{nl} is the radial part of the complete eigenfunction ϕ_a .

For the quark masses and string tension σ in (3.6) the same values listed above have been used, and as far as α_s is concerned, that is supposed to be a constant in (3.6), the value $\alpha_s = 0.35$ has been used, which is the one typically used in non-relativistic calculations, and is also the freezing value adopted in [94].

3.3 Extracting $\alpha_s^{\text{exp}}(Q^2)$ from the data

One focus now on the reversed problem, i.e., the determination of the $\alpha_s^{\text{exp}}(Q^2)$ values at the characteristic scales of a selected number of ground and excited states.

In order to estimate $\alpha_s^{\text{exp}}(Q^2)$ at low energy one needs first to assign an effective Q -value to each state. To this end one first rewrites the squared mass, as given by point c) in Sec. 3.2, more explicitly as the sum of the unperturbed part, the perturbative and the confinement ones respectively

$$m_a^2 = \langle \phi_a | M_0^2 | \phi_a \rangle + \langle \phi_a | U_{\text{OGE}} | \phi_a \rangle + \langle \phi_a | U_{\text{Conf}} | \phi_a \rangle. \quad (3.8)$$

Here U_{OGE} is given by the second line of (3.3) and U_{Conf} by Eq. (3.4) and the first two lines of (3.5). From the OGE contribution one then extracts for each state the fixed coupling value α_a^{th} that leads to the same theoretical mass as by using $\alpha_E^{(1)}(Q^2)$ given by Eq. (2.6). This can be done by means of the relation

$$\langle \phi_a | U_{\text{OGE}} | \phi_a \rangle \equiv \langle \phi_a | \alpha_E^{(1)}(\mathbf{Q}^2) \mathcal{O}(\mathbf{q}; \mathbf{Q}) | \phi_a \rangle = \alpha_a^{\text{th}} \langle \phi_a | \mathcal{O}(\mathbf{q}; \mathbf{Q}) | \phi_a \rangle, \quad (3.9)$$

where $\mathcal{O}(\mathbf{q}; \mathbf{Q})$ can be drawn again by the second line of Eq. (3.3). The effective momentum transfer Q_a associated to each bound state is then identified by the equation

$$\alpha_E^{(1)}(Q_a^2) = \alpha_a^{\text{th}}. \quad (3.10)$$

The next step is to search for the correct (fixed) value of the coupling that exactly reproduces the experimental mass of each state. This is defined by the relation

$$\langle \phi_a | M_0^2 | \phi_a \rangle + \alpha_s^{\text{exp}}(Q_a^2) \langle \phi_a | \mathcal{O}(\mathbf{q}; \mathbf{Q}) | \phi_a \rangle + \langle \phi_a | U_{\text{Conf}} | \phi_a \rangle = m_{\text{exp}}^2, \quad (3.11)$$

so that, by combining Eqs. (3.8), (3.9) and (3.11) one finally obtains

$$\alpha_s^{\text{exp}}(Q_a^2) = \alpha_a^{\text{th}} + \frac{m_{\text{exp}}^2 - m_a^2}{\langle \phi_a | \mathcal{O}(\mathbf{q}; \mathbf{Q}) | \phi_a \rangle}. \quad (3.12)$$

This procedure has been applied to a number of light-light, light-heavy and heavy-heavy ground as well as excited states.

Before discussing the uncertainties related to the extracted $\alpha_s^{\text{exp}}(Q^2)$, few comments are in order.

First note that in the evaluation of Q_a in (3.9) the hyperfine splitting has been neglected, whereas it has been taken into account in (3.12), bringing possibly to different values of α_s^{exp} for the singlet and the triplet states (when there are reliable data for both).

Furthermore, the sensitivity of the effective Q 's derived as above from the specific coupling (2.6), has been checked by analyzing their deviation for a 25% shift of $\Lambda_{n_f=3}^{(1,\text{eff})}$ around the value 193 MeV, and one finds that the average change in the momentum scale amounts to 3%. This makes the resulting $\alpha_s^{\text{exp}}(Q^2)$ reliable, at least qualitatively, even in the deep IR region ($Q < 0.2$ GeV), where the discrepancy with respect to massless $\alpha_E^{(1)}(Q^2)$ is sizable.

Obviously the theoretical meson masses are sensitive to a variation of the quark mass parameters (particularly in the case of the π meson), whereas α_s^{exp} and the relative Q_a turn out to be much more stable. For instance, in the light-light sector, an increase in the light quark mass of 5% amounts to a change of about 2% in the value of α_s^{exp} and 0.2% in the relative Q_a .

Finally, a subtle point concerns the choice of the ‘‘unperturbed’’ α_s involved in the static Hamiltonian (3.6). Actually, the value adopted is very near to the α_a^{th} pertaining to the $b\bar{b}(1S)$ state, but definitively smaller than the typical

α_a^{th} 's. The point is that the hyperfine splitting is much more sensible than the c.o.g. mass to the behaviour of the unperturbed wave function at small distance (large momentum), which is specifically controlled by the value of the unperturbed α_s . As a result, the effective fixed value α_s in Eq. (3.6) that reproduces the same splitting as by using the coupling $\alpha_E^{(1)}(Q^2)$ turns out to be significantly smaller than α_a^{th} calculated from the c.o.g. mass. Essentially, it was chosen a phenomenological value for the unperturbed α_s in order to have a good reproduction of the hyperfine splitting so as to reasonably reconstruct the c.o.g. of the doublet when one component is missing. It was then used the position of the c.o.g. (which is rather stable w.r.t. the unperturbed α_s) to extract the final result $\alpha_s^{\text{exp}}(Q_a^2)$.

3.4 Theoretical uncertainties

First of all, it should be clearly addressed the unavoidable model dependence of the above results. Indeed, the formalism exploited in their derivation is based on the ansatz (3.1), consisting of the sum of two contributions that one knows to be asymptotically correct for small and large quark-antiquark distances. More sophisticated ansatz also exist (see e.g. [91], [92] or [93]), but they turn out to be difficult to implement within BS formalism.

In the context of the model in hand the sources of error are the instantaneous approximation implied by the three-dimensional reduction of the BS equation, the approximations introduced into the resolution of the eigenvalue equation, the inclusion of only the leading perturbative contribution in the BS kernel I , and finally having neglected the coupling between different quark antiquark channels.

Thus, aside from minor effects due to approximations in the resolution of the eigenvalue equation and from the three-dimensional reduction, the main sources of theoretical error in the whole procedure are expected to arise from neglecting the NLO contribution to the BS kernel as well as the coupling with other channels, and these have been explicitly estimates.

The NLO contribution to the perturbative part of the BS-kernel comes from four diagrams with two-gluon exchange; two triangular graphs containing a four-line vertex of the type $g^2\phi^*\phi A_\mu A^\mu$ and two three-line vertices $g\phi^*\partial_\mu\phi A^\mu$ (the spin independent part of the second order BS formalism is quite similar to scalar QED), one *fish diagram* with two four-line vertices, and a crossing

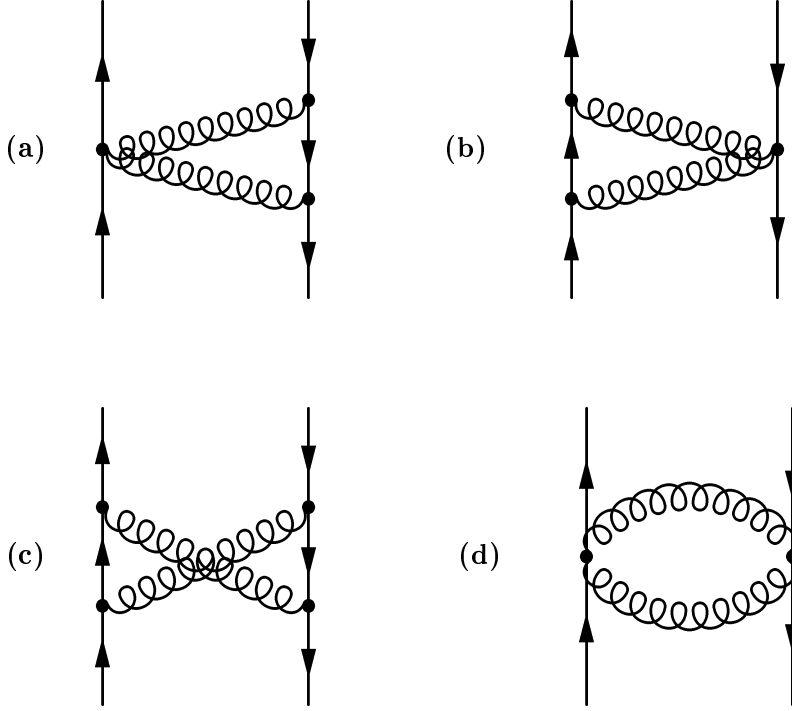


Figure 3.3: NLO contributions to the second order BS kernel I .

box with four three line vertices (see Fig. 3.3). If the renormalization scale is identified with the momentum transfer Q the fish graphs contribution is completely reabsorbed in the renormalization. On the other hand, a somewhat crude estimate of the contribution of each of the two triangular graphs yields

$$I_{\text{triang}} \sim 4 \left(\frac{4}{3} \alpha_s \right)^2 \frac{9m^2}{4Q^2 + 2m^2} \quad (3.13)$$

and for the crossing box graph, similarly

$$I_{\text{crsbox}} \sim \frac{64}{3} \left(\frac{4}{3} \alpha_s \right)^2 \frac{m^4}{(Q^2 + m^2 + k^2)^2}. \quad (3.14)$$

These expressions have to be compared with the leading one-gluon term used in the present calculation

$$I_{\text{OGE}} \sim 16\pi \frac{4}{3} \alpha_s \frac{m^2}{Q^2}. \quad (3.15)$$

Putting all things together, the overall error due to the omission of such NLO contributions to the BS kernel is then

$$\frac{\Delta I}{I} = \sqrt{\left(2 \frac{I_{\text{triang}}}{I_{\text{OGE}}}\right)^2 + \left(\frac{I_{\text{crsbox}}}{I_{\text{OGE}}}\right)^2}, \quad (3.16)$$

and this produces

$$\frac{\Delta \mathcal{O}}{\mathcal{O}} \sim \frac{\Delta I}{I}. \quad (3.17)$$

By using Eqs. (3.9-3.12), after some algebra it is easy to recognize that the NLO effects on α_s^{exp} turn out to be of the same order, that is

$$\Delta_{\text{NLO}} \alpha_s \sim \alpha_a^{\text{th}} \frac{\Delta I}{I}, \quad (3.18)$$

which is what is assumed in the foregoing. The NLO errors do not exceed 5% for heavy quark states whereas they are enhanced up to 20% when light and strange quarks are involved.

Finally, since the strength of the neglected coupling with other channels (OC) is obviously measured by the width Γ_a of the state, one roughly estimates an error of the order of $\Delta m_a \sim \Gamma_a/2$ in the evaluation of the theoretical meson mass m_a . On this basis, for each determination of $\alpha_s^{\text{exp}}(Q_a^2)$ the related theoretical error is given by

$$\Delta_{\Gamma} \alpha_s = \frac{m_a}{\langle \phi_a | \mathcal{O}(\mathbf{q}; \mathbf{Q}) | \phi_a \rangle} \Gamma_a. \quad (3.19)$$

Usually the error Δm_{exp} on the experimental mass m_{exp} is much smaller than $\Gamma_a/2$. When, however, this is not the case one has to consider also the experimental error $\Delta_{\text{exp}} \alpha_s$, obtained from (3.19) by replacing $m_a \Gamma_a$ with $2m_{\text{exp}} \Delta m_{\text{exp}}$.

All other sources of uncertainties aforementioned, that is, the errors implied by the three dimensional reduction, and by the approximations introduced in the resolution of the eigenvalue equation for M^2 , and the one due to the

model dependence, though difficult to be explicitly estimated, can be globally taken into account by means of a comparison between the calculated and the experimental spectrum. To this aim, one can restrict the considerations to a sample of better established data which exclude high orbital excitations (D and F states), and introduce an additional conventional error $\overline{\Delta}m$ on all the theoretical masses, defined by

$$\chi_m^2 = \frac{1}{N_{SP}} \sum_{a=1}^{N_{SP}} (m_a - m_{\text{exp}})^2 / [(\Delta_{\text{tot}}m_a)^2 + (\overline{\Delta}m)^2] \sim 1, \quad (3.20)$$

where $\Delta_{\text{tot}}m_a$ is the total error resulting from all the sources explicitly evaluated, i.e., $(\Delta_{\text{tot}}m_a)^2 = m_a^2 \Delta I/I + (\Gamma_a/2)^2 + (\Delta m_{\text{exp}})^2$, and the sum is restricted to the selected sample of data (namely, S and P states only). It turns out $\overline{\Delta}m \simeq 20$ MeV, and then it can be set $\overline{\Delta}\alpha_s = (2m_a \overline{\Delta}m) / \langle \phi_a | \mathcal{O}(\mathbf{q}; \mathbf{Q}) | \phi_a \rangle$. This uncertainty, that turns out to be about 5% on average, has not been included in the tables, but is used in the analysis of the following section.

3.5 BS-model results: concert of low and high energy data via APT

All results are displayed in details in tables I-VII of App. B, and pictorially in Fig. 3.4. The first three columns specify the state and its experimental mass as given by [2]. The fourth column gives theoretical results for the meson masses, and the last three give the effective Q 's, the relative 3-loop APT coupling $\alpha_E^{(3)}(Q^2)$ and the experimental coupling with errors (both theoretical and experimental).

In Fig. 3.4 values of α_s^{exp} at the same Q from triplet and singlet states have been combined through a weighted average according to their errors.

As one may infer from Fig. 3.4, the experimental points exhibit a remarkable evolution from 500 MeV down to 200 MeV, where only the safer S and P states are involved, in good agreement with the 3-loop analytic coupling $\alpha_E^{(3)}(Q^2)$ properly normalized, i.e., with $\Lambda_{n_f=3}^{(3)} = 417$ MeV, and discussed in Sec. 2 (cf. Eqs. (2.18) and (2.16), (2.17)).

Specifically, defining $\Delta_{\text{tot}}\alpha_s$ as the total error explicitly evaluated by means

of Eqs. (3.18) and (3.19), one finds

$$\chi_\alpha^2 = \frac{1}{N_{SP}} \sum_{a=1}^{N_{SP}} (\alpha_s^{\text{exp}}(Q_a^2) - \alpha_E^{(3)}(Q_a^2))^2 / [(\Delta_{\text{tot}}\alpha_s)^2 + (\overline{\Delta}\alpha_s)^2] \sim 0.8. \quad (3.21)$$

The agreement quantitatively supports the relevance of the APT approach to IR phenomena down to a few hundred MeV.

On the other hand, at energies below 200 MeV there seems to exist a general tendency of $\alpha_s^{\text{exp}}(Q^2)$ to deviate from the APT curve and to approach zero, or at least a finite limit, which is less than the universal APT freezing value. Note, however, that the analysis of such an extreme IR behaviour is based on high orbital excitations (D and F states), that lie well above the strong decay thresholds and possess large widths. As a consequence, the theoretical reliability of the method is lower at these scales, as apparent from the large estimated errors. Moreover, also the discrepancy between $\alpha_E^{(1)}(Q^2)$ (used in the calculation) and $\alpha_E^{(3)}(Q^2)$ (used as a reference term) rises above 10% at these scales. In fact, only two states $\pi_2(1670)$ (interpreted as $s\bar{s}(1^1D_2)$) and $f_2(2150)$ ($s\bar{s}(1^3F_2)$), corresponding to $Q \simeq 120$ MeV, generate $\alpha_s^{\text{exp}}(Q^2)$ (marginally) out of the error bands, and the state $f_2(2150)$, which has been observed only once, has never been confirmed.

Nevertheless, as already noted, such a deep IR behaviour could correlate with some lattice results [17], and could be discussed within theoretical models, in particular within the recently developed “massive” modification of APT, briefly discussed in Sec. 2.4. Specifically, as displayed in Fig. 3.4, the 1-loop coupling $\alpha(Q^2, m^2)$ (2.34) with an effective mass $m_{\text{eff}} \simeq (38 \pm 10)$ MeV reasonably fits all experimental points down to the deep infrared region.

Notice that in the selection of states irregular and incomplete multiplets have been excluded as a rule. Of this type, e.g., in the light quark sector, are the $3S$ states ($m_{3^3S_1} - m_{3^1S_0}$ is anomalously large and about twice as $m_{2^3S_1} - m_{2^1S_0}$), 1^3P ($m_{1^3P_0}$ being larger than $m_{1^3P_1}$), 1^3D , F , G , H (incomplete). If however included in the analysis, all these states would bring the results in agreement with the general tendency outlined.

As far as the renormalization scheme dependence is concerned, note that the coupling definition is implicitly embodied in ansatz (3.1). Specifically, here one assumes that after the area term subtraction, $i \ln W$ is dominated by the OGE term, with the fixed coupling α_s replaced by the running coupling $\alpha_s(Q^2)$. This amounts to including all the dressing effects into $\alpha_s(Q^2)$. It

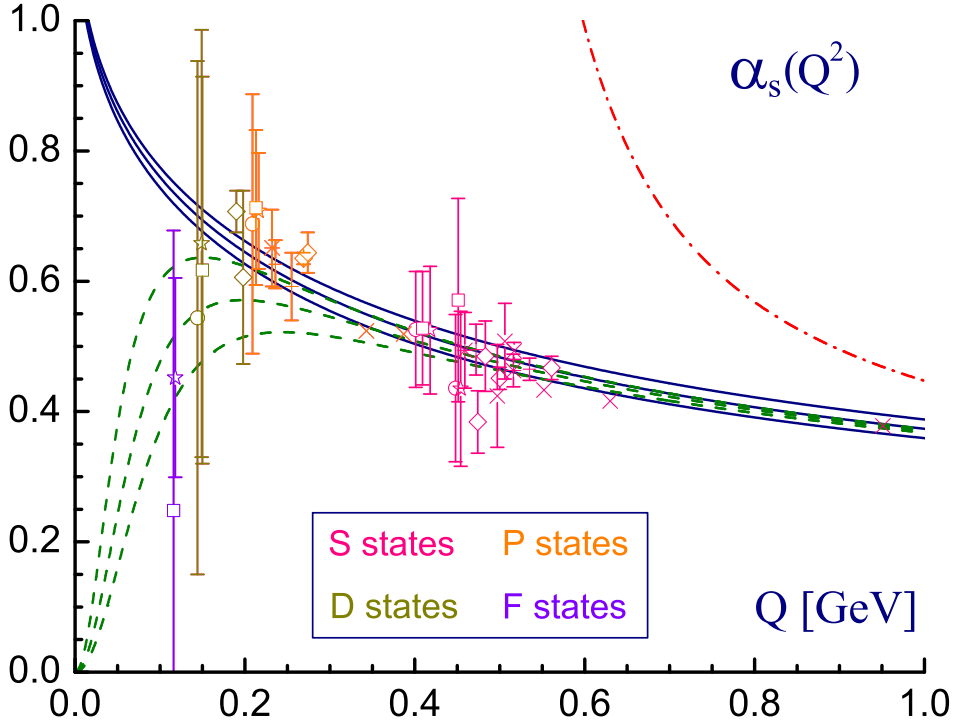


Figure 3.4: Extracted values of $\alpha_s^{\text{exp}}(Q^2)$ against the 3-loop APT coupling (2.3) with $\Lambda_{n_f=3}^{(3)} = (417 \pm 42) \text{ MeV}$ (solid), and its perturbative counterpart (dot-dashed). The “massive” 1-loop APT coupling ($n = 1$ in (2.32)) refers to $\Lambda_{n_f=3}^{(1,\text{eff})} = 204 \text{ MeV}$ and $m_{\text{eff}} = (38 \pm 10) \text{ MeV}$ (dashed). Circles, stars and squares refer respectively to $q\bar{q}$, $s\bar{s}$ and $q\bar{s}$ with $q = u, d$, diamonds and crosses to $c\bar{c}$ and $b\bar{b}$; asterisks stay for $q\bar{c}$ and $q\bar{b}$, whereas plus signs for $s\bar{c}$ and $s\bar{b}$.

is worth noting that the coupling defined in such way is free of unphysical singularities by construction.

At the same time, the 1-loop effective APT coupling $\alpha_E(Q^2)$, involved in the calculation of the meson spectrum, is remarkably stable with respect to both the higher loop corrections and the choice of renormalization scheme (see Sec. 2. and a detailed discussion of this issue in Ref. [63]). Thus one might expect that the same situation should also occur for $\alpha_{\text{exp}}(Q^2)$, with the possible exception for the deep infrared region, where other nonperturbative effects could be relevant.

Quark self-energy effects have been taken into account by a recursive resolu-

tion of the Dyson-Schwinger equation. In the second order BS formalism this simply amounts to replacing the current quark masses with the constituent masses [95].

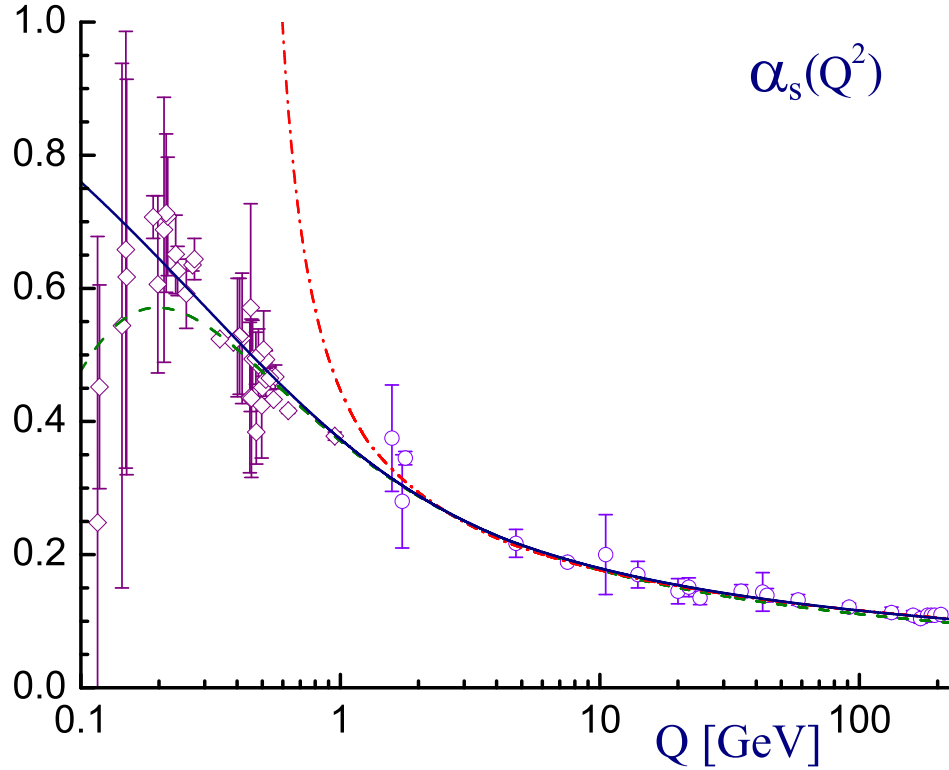


Figure 3.5: Summary of low (\diamond) and high energy (\circ) data against the 3-loop analytic coupling (2.5) (solid curve) and its perturbative counterpart (dot-dashed curve) both normalized at the Z boson mass. Also shown is the “massive” 1-loop analytic coupling (2.34) (dashed curve) same as in Fig. 3.4.

Finally, Fig. 3.5 displays a synthesis of the results for $\alpha_s(Q^2)$ extracted from the bound states calculation in the BS framework, with a sample of high energy data as given by S. Bethke [1], against the 3-loop APT coupling $\alpha_E^{(3)}(Q^2)$ (2.5) and its massive modification (2.34). Also shown in the figure is the common perturbative 3-loop coupling with IR singular behaviour that is ruled out by the data. As can be seen, the BS-APT theoretical scheme allows a rather satisfactory correlated understanding of very high and rather

low energy phenomena.

Chapter 4

Conclusive remarks

To summarize, as discussed in Sec. 1, straightforward application of the RG method to perturbative expansions in QCD eventually gives rise to unphysical singularities in both the running coupling and the physical observables, in the low energy domain. The Landau singularities severely complicate theoretical analyses of hadron dynamics.

Then, an useful prescription to eliminate unphysical singularities is provided by the APT approach, outlined in Sec. 2, which is based upon the analyticity requirement of the QCD coupling. This prescription has been used in previous works in the framework of a Bethe-Salpeter like formalism to compute the meson spectrum.

In this work, the point of view has been then somewhat reversed, namely, as discussed in Sec. 3, the comparison between the calculated meson spectrum within the BS framework and the experimental data is used, in order to extract information on the infrared behavior of the QCD running coupling.

The method consists in solving the eigenvalue equation for the squared mass operator as given by Eq. (3.2), obtained by a three dimensional reduction of the original BS equation. The relativistic potential U then follows from a proper ansatz (3.1) on the Wilson loop to encode confinement, and is the sum (3.2) of a one-gluon-exchange term U_{OGE} and a confining term U_{Conf} . The strong coupling occurring in the perturbative part of the potential needs to be IR finite since its argument has to be identified with the momentum transfer in the $q\bar{q}$ interaction, and this typically takes values down to few hundreds MeV.

As a first step, the common perturbative running coupling α_s has then been replaced by its 1-loop analytized counterpart $\alpha_E^{(1)}$ Eq. (2.6) as derived by the APT algorithm, which avoids the hurdle of the spurious singularities in the IR region [23], the whole theoretical scheme being extensively discussed in Sec. 2.

An effective QCD scale $\Lambda_{n_f=3}^{(1,\text{eff})} = 193$ MeV has been imposed in order to reasonably reproduce the 3-loop APT coupling, normalized at the Z boson mass along with world average [2] (i.e., $\Lambda_{n_f=5}^{(3)} = 236$ MeV and $\Lambda_{n_f=3}^{(3)} = 417$ MeV by continuous threshold matching), specifically in the neighborhood of 0.5 GeV, which is the typical scale of most of the input states.

Then, it has been taken advantage of the BS results for the meson spectrum, both in the light and heavy quark sector, to deduce within this framework the fixed coupling value for each state that exactly matches the theoretical and experimental mass.

A key point is finally the comparison of such experimental determinations α_s^{exp} with the “Euclidean” APT coupling $\alpha_E^{(3)}(Q^2)$ and its further “massive” development.

The results are twofold. On the one hand, as expected on the basis of the reasonable agreement between the theoretical and the experimental meson data, the 3-loop analytic coupling remarkably fits the extracted points $\alpha_s^{\text{exp}}(Q^2)$ from 1 GeV down to 200 MeV, within the evaluated errors, both theoretical and experimental. This confirms and yields a quantitative estimate of the relevance of the APT to IR phenomena down to 200 MeV.

Besides, below this scale, the experimental points exhibit a tendency to deviate with respect to the APT curve. Despite the sizable errors, this could give a hint on the vanishing of $\alpha_s(Q^2)$ as $Q \rightarrow 0$ in concert with some results from lattice simulations [17]. It should be emphasized, however, that the existence of a finite IR limit of $\alpha_s(Q^2)$, lower than the universal APT freezing value, can not be ruled out by these data.

Nevertheless, a vanishing QCD coupling at zero momentum transfer can be theoretically discussed in the framework of a recent “massive” modification [90] of the APT formalism, which takes into account effects of a finite threshold in the dispersion relations. Since in the extremely low Q region confinement forces play the dominant role, the overall reasonable agreement between the “massive” APT model and the results of the BS formalism would suggest a relation between the linear potential, arising from the area term in the ansatz (3.1), and the thresholds effects in the analytic properties of the

QCD coupling, that needs to be further investigated.

Appendix A: Second order Bethe-Salpeter formalism

In the QCD framework a *second order* four point quark-antiquark function and the full quark propagator can be defined as

$$H_4(x_1, x_2; y_1, y_2) = -\frac{1}{3} \text{Tr}_{\text{color}} \langle \Delta_1(x_1, y_1; A) \Delta_2(y_2, x_2; A) \rangle \quad (4.1)$$

and

$$H_2(x - y) = \frac{i}{\sqrt{3}} \text{Tr}_{\text{color}} \langle \Delta(x, y; A) \rangle, \quad (4.2)$$

where

$$\langle f[A] \rangle = \int DA M_F[A] e^{iS_G[A]} f[A], \quad (4.3)$$

$M_F[A] = \text{Det} \Pi_{j=1}^2 [1 + g\gamma^\mu A_\mu (i\gamma_j^\nu \partial_{j\nu} - m_j^{\text{curr}})^{-1}]$ and $\Delta(x, y; A)$ is the *second order* quark propagator in an external gauge field.

The quantity Δ is defined by the second order differential equation

$$(D_\mu D^\mu + m_{\text{curr}}^2 - \frac{1}{2} g \sigma^{\mu\nu} F_{\mu\nu}) \Delta(x, y; A) = -\delta^4(x - y), \quad (4.4)$$

($\sigma^{\mu\nu} = \frac{i}{2} [\gamma^\mu, \gamma^\nu]$ and $D_\mu = \partial_\mu + igA_\mu$) and it is related to the corresponding first order propagator by $S(x, y; A) = (i\gamma^\nu D_\nu + m_{\text{curr}}) \Delta(x, y; A)$, m_{curr} being the so-called current mass of the quark.

The advantage of considering second order quantities is that the spin terms are more clearly separated and it is possible to write for Δ a generalized Feynman-Schwinger representation, i.e., to solve Eq. (4.4) in terms of a quark path integral [24, 94]. Using the latter in (4.1) or (4.2) a similar representation can be obtained for H_4 and H_2 .

The interesting aspect of this final representation is that the gauge field appears in it only through a Wilson line correlator W . In the limit $x_2 \rightarrow x_1$, $y_2 \rightarrow y_1$ or $y \rightarrow x$ the Wilson lines close in a single Wilson loop Γ and if Γ stays on a plane, $i \ln W$ can be written according to (3.1) as

$$i \ln W = \frac{16\pi}{3} \alpha_s \oint dz^\mu \oint dz^{\nu'} D_{\mu\nu}(z - z') + \sigma \oint dz^0 \oint dz^{0'} \delta(z^0 - z^{0'}) |\mathbf{z} - \mathbf{z}'| \int_0^1 d\lambda \left\{ 1 - \left[\lambda \frac{d\mathbf{z}_\perp}{dz^0} + (1 - \lambda) \frac{d\mathbf{z}'_\perp}{dz^{0'}} \right]^2 \right\}^{\frac{1}{2}}. \quad (4.5)$$

The area term here is written as the algebraic sum of successive equal time strips and $d\mathbf{z}_\perp = d\mathbf{z} - (d\mathbf{z} \cdot \mathbf{r})\mathbf{r}/r^2$ denotes the transversal component of $d\mathbf{z}$. The basic assumption now is that, in the center of mass frame, (4.5) remains a good approximation even in the general case, i.e., for non flat curves and when $x_2 \neq x_1$, $y_2 \neq y_1$ or $y \neq x$. Then, by appropriate manipulations on the resulting expressions, an inhomogeneous Bethe-Salpeter equation for the 4-point function $H_4(x_1, x_2; y_1, y_2)$ and a Dyson-Schwinger equation for $H_2(x-y)$ can be derived in a kind of generalized ladder and rainbow approximation respectively. This should appear plausible, even from the point of view of graph resummation, for the analogy between the perturbative and the confinement terms in (4.5). In momentum representation, the corresponding homogeneous BS-equation becomes

$$\begin{aligned} \Phi_P(k) = & -i \int \frac{d^4u}{(2\pi)^4} \hat{I}_{ab} \left(k-u; \frac{1}{2}P + \frac{k+u}{2}, \frac{1}{2}P - \frac{k+u}{2} \right) \times \\ & \times \hat{H}_2^{(1)} \left(\frac{1}{2}P + k \right) \sigma^a \Phi_P(u) \sigma^b \hat{H}_2^{(2)} \left(-\frac{1}{2}P + k \right), \end{aligned} \quad (4.6)$$

where $\sigma^0 = 1$; $a, b = 0, \mu\nu$; the c.m. frame has to be understood, $P = (m_B, \mathbf{0})$; $\Phi_P(k)$ denotes the appropriate *second order* wave function, that in terms of the second order field $\phi(x) = (i\gamma^\mu D_\mu + m_{\text{curr}})^{-1}\psi(x)$ can be defined as the Fourier transform of $\langle 0|\phi(\frac{\xi}{2})\bar{\psi}(-\frac{\xi}{2})|P\rangle$.

Similarly, in terms of the irreducible self-energy, defined by $\hat{H}_2(k) = i(k^2 - m_{\text{curr}}^2)^{-1} + i(k^2 - m_{\text{curr}}^2)^{-1} i \Gamma(k) \hat{H}_2(k)$, the Dyson-Schwinger equation can be written

$$\hat{\Gamma}(k) = \int \frac{d^4l}{(2\pi)^4} \hat{I}_{ab} \left(k-l; \frac{k+l}{2}, \frac{k+l}{2} \right) \sigma^a \hat{H}_2(l) \sigma^b. \quad (4.7)$$

The kernels are the same in the two Eqs. (4.6) and (4.7), consistently with the requirement of chiral symmetry limit [25], being given by

$$\begin{aligned} \hat{I}_{0;0}(Q; p, p') &= 16\pi \frac{4}{3} \alpha_s p^\alpha p'^\beta \hat{D}_{\alpha\beta}(Q) + \\ &+ 4\sigma \int d^3\zeta e^{-i\mathbf{Q}\cdot\zeta} |\zeta| \epsilon(p_0) \epsilon(p'_0) \int_0^1 d\lambda \{ p_0^2 p_0'^2 - [\lambda p'_0 \mathbf{p}_T + (1-\lambda) p_0 \mathbf{p}'_T]^2 \}^{\frac{1}{2}} \\ \hat{I}_{\mu\nu;0}(Q; p, p') &= 4\pi i \frac{4}{3} \alpha_s (\delta_\mu^\alpha Q_\nu - \delta_\nu^\alpha Q_\mu) p'_\beta \hat{D}_{\alpha\beta}(Q) - \\ &- \sigma \int d^3\zeta e^{-i\mathbf{Q}\cdot\zeta} \epsilon(p_0) \frac{\zeta_\mu p_\nu - \zeta_\nu p_\mu}{|\zeta| \sqrt{p_0^2 - \mathbf{p}_T^2}} p'_0 \end{aligned}$$

$$\begin{aligned}
\hat{I}_{0;\rho\sigma}(Q; p, p') &= -4\pi i \frac{4}{3} \alpha_s p^\alpha (\delta_\rho^\beta Q_\sigma - \delta_\sigma^\beta Q_\rho) \hat{D}_{\alpha\beta}(Q) + \\
&\quad + \sigma \int d^3\zeta e^{-i\mathbf{Q}\cdot\zeta} p_0 \frac{\zeta_\rho p'_\sigma - \zeta_\sigma p'_\rho}{|\zeta| \sqrt{p_0'^2 - \mathbf{p}'^2}} \epsilon(p'_0) \\
\hat{I}_{\mu\nu;\rho\sigma}(Q; p, p') &= \pi \frac{4}{3} \alpha_s (\delta_\mu^\alpha Q_\nu - \delta_\nu^\alpha Q_\mu) (\delta_\rho^\alpha Q_\sigma - \delta_\sigma^\alpha Q_\rho) \hat{D}_{\alpha\beta}(Q), \quad (4.8)
\end{aligned}$$

where in the second and in the third equation $\zeta_0 = 0$ has to be understood. Notice that, due to the privileged role given to the c.m. frame, the terms proportional to σ in (4.8) formally are not covariant.

In fact, it can be checked that $\Gamma(k)$ can be consistently assumed to be spin independent and Eq. (4.7) can be rewritten in the simpler form

$$\Gamma(k) = i \int \frac{d^4l}{(2\pi)^4} \frac{R(k, l)}{l^2 - m^2 + \Gamma(l)}, \quad (4.9)$$

with

$$\begin{aligned}
R(k, l) &= 4\pi \frac{4}{3} \alpha_s [(k+l)^\mu (k+l)^\nu D_{\mu\nu}(k-l) + \\
&\quad (k-l)_\nu (k-l)^\nu D_\mu^\mu(k-l) - (k-l)^\mu (k-l)^\nu D_{\mu\nu}(k-l)] + \\
&\quad + \sigma \int d^3\mathbf{r} e^{-i(\mathbf{k}-\mathbf{l})\cdot\mathbf{r}} r (k_0 + l_0)^2 \sqrt{1 - \frac{(\mathbf{k}_\perp + \mathbf{l}_\perp)^2}{(k_0 + l_0)^2}}, \quad (4.10)
\end{aligned}$$

\mathbf{k}_\perp and \mathbf{l}_\perp denoting as above the transversal part of \mathbf{k} and \mathbf{l} . Eq. (4.9) can be solved by iteration resulting in an expression of the form $\Gamma(k^2, \mathbf{k}^2)$, since (4.10) is not formally covariant. Then the constituent (pole) mass m is defined by the equation

$$m^2 - m_{\text{curr}}^2 + \Gamma(m^2, \mathbf{k}^2) = 0 \quad (4.11)$$

and the dependence on \mathbf{k}^2 , being an artifact of the ansatz (3.1), is eliminated by extremizing $m(\mathbf{k}^2)$ in \mathbf{k}^2 .

The 3-dimensional reduction of Eq. (4.6) can be obtained by a usual procedure of replacing $H_2(k)$ with $i(k^2 - m^2)^{-1}$ and \hat{I}_{ab} with its so-called instantaneous approximation $\hat{I}_{ab}^{\text{inst}}(\mathbf{k}, \mathbf{u})$. In this way, one can explicitly integrate over u_0 and arrive to a 3-dimensional equation in the form of the eigenvalue equation for a squared mass operator Eq. (3.2), with [24]

$$\langle \mathbf{k} | U | \mathbf{k}' \rangle = \frac{1}{(2\pi)^3} \sqrt{\frac{w_1 + w_2}{2w_1 w_2}} \hat{I}_{ab}^{\text{inst}}(\mathbf{k}, \mathbf{k}') \sqrt{\frac{w'_1 + w'_2}{2w'_1 w'_2}} \sigma_1^a \sigma_2^b. \quad (4.12)$$

Finally by using Eq. (4.8) one obtains Eqs. (3.3-3.5).

Alternatively, in more usual terms, one could look for the eigenvalue of the mass operator or center of mass Hamiltonian $H_{\text{CM}} \equiv M = M_0 + V$ with V defined by $M_0V + VM_0 + V^2 = U$. Neglecting term V^2 the linear form potential V can be obtained from U by the replacement $\sqrt{\frac{(w_1+w_2)(w'_1+w'_2)}{w_1w_2w'_1w'_2}} \rightarrow \frac{1}{2\sqrt{w_1w_2w'_1w'_2}}$. The resulting expression is particularly useful for a comparison with models based on potential. In particular, in the static limit V reduces to the Cornell potential

$$V_{\text{stat}} = -\frac{4}{3} \frac{\alpha_s}{r} + \sigma r. \quad (4.13)$$

Note that it is necessary to introduce a cut-off B in Eq. (4.9). As a consequence the constituent mass turns out to be a function of the current mass and of B , $m = m(m_{\text{curr}}, B)$. Then if one uses a running current mass $m_{\text{curr}}(Q^2)$, a running constituent mass $m(Q^2)$ is obtained, as it has been done in [95]. However the singular expression used there

$$m_{\text{curr}}(Q^2) = \hat{m} \left(\frac{Q^2/\Lambda^2 - 1}{Q^2/\Lambda^2 \ln(Q^2/\Lambda^2)} \right)^{\gamma_0/2\beta_0} \quad (4.14)$$

is not consistent with Eq. (2.6), and if a more consistent assumption is taken, e.g.,

$$m_{\text{curr}}(Q^2) = \hat{m} \left(\alpha_{\text{E}}^{(1)}(Q^2) \right)^{\gamma_0/2\beta_0}, \quad (4.15)$$

or the other resulting from the analytization of a similar expression with $\alpha_{\text{E}}^{(1)}(Q^2)$ replaced with the ordinary perturbative $\alpha_{\text{s}}^{(1)}(Q^2)$, the dependence of m on Q^2 is strongly reduced. For this reason even the light quark mass is here treated as a constants to be adjusted with the the data¹.

¹In this way the only role that is left to the DS equation is to justify the difference between the constituent and the current masses.

Appendix B: Numerical results

The tables below display the complete set of results as explained in Sec. 3.5. The values of all the parameters are $\sigma = 0.18 \text{ GeV}^2$, $\Lambda_{n_f=3}^{(1,\text{eff})} = 193 \text{ MeV}$, $m_q = 196 \text{ MeV}$ ($q = u, d$), $m_s = 352 \text{ MeV}$, $m_c = 1.516 \text{ GeV}$ and $m_b = 4.854 \text{ GeV}$. Meson masses are given in MeV. The last column displays the experimental coupling $\alpha_s^{\text{exp}}(Q_a^2)$ with the theoretical error Δ_{NLO} due to the next-to-leading order terms neglected, the theoretical error Δ_Γ from the half width $\Gamma/2$ and the experimental error Δ_{exp} respectively.

† Center of gravity masses of the incomplete multiplets estimated in analogy with other multiplets.

Table 4.1: $q\bar{q}$ ($q = u, d$)

States	(MeV)	m_{exp}	m_{th}	Q	$\alpha_E^{(3)}$	$\alpha_s^{\text{exp}} \pm \Delta_{\text{NLO}} \pm \Delta_\Gamma \pm \Delta_{\text{exp}}$	
1^1S_0	$\left\{ \begin{array}{l} \pi^0 \\ \pi^\pm \end{array} \right.$	$\left. \begin{array}{l} 134.9766 \pm 0.0006 \\ 139.57018 \pm 0.00035 \end{array} \right\}$	138	136	401	0.522	$0.534 \pm 0.122 \pm - \pm -$
1^3S_1	$\rho(770)$	775.5 ± 0.4	749				$0.517 \pm 0.122 \pm 0.048 \pm -$
$1\Delta\text{SS}$		638	613				
2^1S_0	$\pi(1300)$	1300 ± 100	1223	448	0.502		$0.451 \pm 0.114 \pm 0.152 \pm 0.081$
2^3S_1	$\rho(1450)$	1459 ± 11	1363				$0.427 \pm 0.114 \pm 0.062 \pm 0.010$
$2\Delta\text{SS}$		159	139				
1^1P_1	$b_1(1235)$	1229.5 ± 3.2	1234	209	0.637		$0.688 \pm 0.155 \pm 0.124 \pm 0.006$
1^1D_2	$\pi_2(1670)$	1672.4 ± 3.2	1595	144	0.701		$0.544 \pm 0.151 \pm 0.364 \pm 0.009$

Table 4.2: $s\bar{s}$

States	(MeV)	m_{exp}	m_{th}	Q	$\alpha_E^{(3)}$	$\alpha_s^{\text{exp}} \pm \Delta_{\text{NLO}} \pm \Delta_\Gamma \pm \Delta_{\text{exp}}$	
1^3S_1	$\phi(1020)$	1019.460 ± 0.019	1019	418	0.514		$0.525 \pm 0.098 \pm 0.002 \pm -$
2^3S_1	$\phi(1680)$	1680 ± 20	1602	454	0.500		$0.435 \pm 0.096 \pm 0.068 \pm 0.019$
1^1P_1	$h_1(1380)$	1386 ± 19	1472	216	0.631		$0.824 \pm 0.098 \pm 0.083 \pm 0.032$
1^3P_2	$f'_2(1525)$	1525 ± 5	1521	1484			$0.603 \pm 0.098 \pm 0.070 \pm 0.009$
1^3P_1	$f_1(1510)$	1518 ± 5					
1^3P_0	$f_0(1500)$	1507 ± 5					
1^1D_2	$\eta_2(1870)$	1842 ± 8					
1^3F_4		2156 ± 11	2165†	2070	118	0.733	$0.452 \pm 0.064 \pm 0.137 \pm 0.024$
1^3F_3							
1^3F_2	$f_2(2150)$						

Table 4.3: $q\bar{s}$ ($q = u, d$)

States	(MeV)	m_{exp}	m_{th}	Q	$\alpha_E^{(3)}$	$\alpha_s^{\text{exp}} \pm \Delta_{\text{NLO}} \pm \Delta_\Gamma \pm \Delta_{\text{exp}}$	
1^1S_0	$\left\{ \begin{array}{l} K^0 \\ K^\pm \end{array} \right.$	$\left. \begin{array}{l} 497.648 \pm 0.022 \\ 493.677 \pm 0.016 \end{array} \right\}$	495	491	409	0.518	$0.529 \pm 0.122 \pm - \pm -$
1^3S_1	$\left\{ \begin{array}{l} K^*(892)^0 \\ K^*(892)^\pm \end{array} \right.$	$\left. \begin{array}{l} 896.00 \pm 0.25 \\ 891.66 \pm 0.26 \end{array} \right\}$	893.11	887			$0.526 \pm 0.122 \pm 0.017 \pm -$
$1\Delta_{SS}$		398	396				
2^3S_1	$K^*(1410)$	1414 ± 15	1485	451	0.501		$0.571 \pm 0.117 \pm 0.102 \pm 0.013$
1^1P_1	$K_1(1270)$	1272 ± 7	1355	213	0.634		$0.820 \pm 0.129 \pm 0.081 \pm 0.012$
1^3P_2	$\left\{ \begin{array}{l} K_2^*(1430)^0 \\ K_2^*(1430)^\pm \end{array} \right.$	$\left. \begin{array}{l} 1432.4 \pm 1.3 \\ 1425.6 \pm 1.5 \end{array} \right\}$	1417.7	1367			$0.583 \pm 0.129 \pm 0.133 \pm 0.007$
1^3P_1	$K_1(1400)$	1402 ± 7					
1^3P_0	$K_0^*(1430)$	1414 ± 6					
1^3D_3	$K_3^*(1780)$	1776 ± 7	1763	1712	150	0.694	$0.617 \pm 0.113 \pm 0.273 \pm 0.031$
1^3D_2	$K_2(1770)$	1773 ± 8					
1^3D_1	$K^*(1680)$	1717 ± 27					
1^3F_4	$K_4^*(2045)$	2045 ± 9	2121	1973	116	0.736	$0.248 \pm 0.095 \pm 0.413 \pm 0.071$
1^3F_3	$K_3(2320)$	2324 ± 24					
1^3F_2	$K_2^*(1980)$	1973 ± 25					

Table 4.4: $c\bar{c}$

States	(MeV)	m_{exp}	m_{th}	Q	$\alpha_{\text{E}}^{(3)}$	$\alpha_{\text{s}}^{\text{exp}} \pm \Delta_{\text{NLO}} \pm \Delta_{\Gamma} \pm \Delta_{\text{exp}}$
1^1S_0	$\eta_c(1\text{S})$	2980.4 ± 1.2	2980	561	0.464	$0.467 \pm 0.025 \pm 0.008 \pm 0.001$
1^3S_1	$J/\psi(1\text{S})$	3096.916 ± 0.011	3097			$0.467 \pm 0.025 \pm - \pm -$
$1\Delta\text{SS}$		117	118			
2^1S_0	$\eta_c(2\text{S})$	3638 ± 4	3595	500	0.483	$0.446 \pm 0.023 \pm 0.007 \pm 0.004$
2^3S_1	$\psi(2\text{S})$	3686.093 ± 0.034	3653			$0.455 \pm 0.023 \pm - \pm -$
$2\Delta\text{SS}$		48	58			
3^3S_1	$\psi(4040)$	4039 ± 1	4030	483	0.489	$0.485 \pm 0.022 \pm 0.049 \pm 0.001$
4^3S_1	$\psi(4415)$	4421 ± 4	4337	474	0.492	$0.384 \pm 0.022 \pm 0.042 \pm 0.006$
1^1P_1	$h_c(1\text{P})$	3525.93 ± 0.27	3532	269	0.592	$0.631 \pm 0.012 \pm - \pm -$
1^3P_2	$\chi_{c2}(1\text{P})$	3556.20 ± 0.09	3525.3	3537		$0.640 \pm 0.012 \pm 0.002 \pm -$
1^3P_1	$\chi_{c1}(1\text{P})$	3510.66 ± 0.07				
1^3P_0	$\chi_{c0}(1\text{P})$	3414.76 ± 0.35				
2^3P_2	$\chi_{c2}(2\text{P})$	3929 ± 5	3915 [†]	3929	274	0.589
2^3P_1						
2^3P_0	$X(3872)$	3871.2 ± 0.5				$0.644 \pm 0.013 \pm 0.027 \pm 0.009$
1^3D_3	$\psi(3770)$	3771.1 ± 2.4	3820 [†]	3822	190	0.654
1^3D_2						
1^3D_1						
2^3D_3	$\psi(4160)$	4153 ± 3	4183 [†]	4150	198	0.646
2^3D_2						
2^3D_1						

Quantum numbers of $h_c(1\text{P})$ and $X(3872)$ mesons are not well established.

Table 4.5: $b\bar{b}$

States	(MeV)	m_{exp}	m_{th}	Q	$\alpha_{\text{E}}^{(3)}$	$\alpha_{\text{s}}^{\text{exp}} \pm \Delta_{\text{NLO}} \pm \Delta_{\Gamma} \pm \Delta_{\text{exp}}$	
1^3S_1	$\Upsilon(1\text{S})$	9460.30 ± 0.26	9461	951	0.381	$0.378 \pm 0.006 \pm - \pm -$	
2^3S_1	$\Upsilon(2\text{S})$	10023.26 ± 0.31	9987	630	0.445	$0.416 \pm 0.004 \pm - \pm -$	
3^3S_1	$\Upsilon(3\text{S})$	10355.2 ± 0.5	10321	552	0.466	$0.433 \pm 0.003 \pm - \pm -$	
4^3S_1	$\Upsilon(4\text{S})$	10579.4 ± 1.2	10588	517	0.478	$0.493 \pm 0.003 \pm 0.013 \pm 0.002$	
5^3S_1	$\Upsilon(10860)$	10865 ± 8	10820	497	0.484	$0.424 \pm 0.003 \pm 0.078 \pm 0.011$	
6^3S_1	$\Upsilon(11020)$	11019 ± 8	11034	506	0.481	$0.508 \pm 0.003 \pm 0.057 \pm 0.012$	
1^3P_2	$\chi_{b2}(1\text{P})$	$9912.21 \pm 0.26 \pm 0.31$	9899.87	9880	387	0.528	$0.519 \pm 0.002 \pm - \pm -$
1^3P_1	$\chi_{b1}(1\text{P})$	$9892.78 \pm 0.26 \pm 0.31$					
1^3P_0	$\chi_{b0}(1\text{P})$	$9859.44 \pm 0.42 \pm 0.31$					
2^3P_2	$\chi_{b2}(2\text{P})$	$10268.65 \pm 0.22 \pm 0.50$	10260.24	10231	343	0.549	$0.524 \pm 0.002 \pm - \pm 0.001$
2^3P_1	$\chi_{b1}(2\text{P})$	$10255.46 \pm 0.22 \pm 0.50$					
2^3P_1	$\chi_{b1}(2\text{P})$	$10255.46 \pm 0.22 \pm 0.50$					
2^3P_0	$\chi_{b0}(2\text{P})$	$10232.5 \pm 0.4 \pm 0.50$					

Table 4.6: Light-heavy quarkonium systems

States	(MeV)	m_{exp}	m_{th}	Q	$\alpha_{\text{E}}^{(3)}$	$\alpha_{\text{s}}^{\text{exp}} \pm \Delta_{\text{NLO}} \pm \Delta_{\Gamma} \pm \Delta_{\text{exp}}$	
$q\bar{c}$							
1^1S_0	$\left\{ \begin{array}{l} D^\pm \\ D^0 \end{array} \right.$	1869.3 ± 0.4 1864.5 ± 0.4	1867.7	1843	459	0.498	$0.488 \pm 0.082 \pm - \pm -$
1^3S_1	$\left\{ \begin{array}{l} D^*(2010)^\pm \\ D^*(2007)^0 \end{array} \right.$	2010.0 ± 0.4 2006.7 ± 0.4					
$1\Delta\text{SS}$		141 ± 1					157
1P_2	$\left\{ \begin{array}{l} D_2^*(2460)^\pm \\ D_2^*(2460)^0 \end{array} \right.$	2459 ± 4 2461.1 ± 1.6	2443	232	0.619	$0.651 \pm 0.051 \pm 0.028 \pm 0.005$	
1P_1	$\left\{ \begin{array}{l} D_1(2420)^\pm \\ D_1(2420)^0 \end{array} \right.$	2423.4 ± 3.1 2422.3 ± 1.3					
$q\bar{b}$							
1^1S_0	$\left\{ \begin{array}{l} B^\pm \\ B^0 \end{array} \right.$	5279.0 ± 0.5 5279.4 ± 0.5	5279.1	5246	516	0.478	$0.456 \pm 0.036 \pm - \pm -$
1^3S_1	B^*	5325.0 ± 0.6					
$1\Delta\text{SS}$		46 ± 3					64

Table 4.7: Light-heavy quarkonium systems

States	(MeV)	m_{exp}	m_{th}	Q	$\alpha_{\text{E}}^{(3)}$	$\alpha_s^{\text{exp}} \pm \Delta_{\text{NLO}} \pm \Delta_{\Gamma} \pm \Delta_{\text{exp}}$
$s\bar{c}$						
1^1S_0	D_s^\pm	1968.2 ± 0.5	1959	472	0.493	$0.494 \pm 0.055 \pm - \pm -$
1^3S_1	$D_s^{*\pm}$	2112.0 ± 0.6	2109			$0.497 \pm 0.055 \pm - \pm -$
$1\Delta\text{SS}$		144 ± 1	149			
1P_2	$D_{s2}(2573)^\pm$	2573.5 ± 1.7	2545	236	0.616	$0.626 \pm 0.036 \pm 0.009 \pm 0.002$
1P_1	$D_{s1}(2536)^\pm$	$2535.35 \pm 0.34 \pm 0.5$				
$s\bar{b}$						
1^1S_0	B_s^0	5367.5 ± 1.8	5343	535	0.472	$0.457 \pm 0.024 \pm - \pm 0.001$
1^3S_1	B_s^*	5412.8 ± 1.7	5408			$0.473 \pm 0.024 \pm - \pm 0.001$
$1\Delta\text{SS}$		47 ± 4	65			
1P	$B_{sJ}^*(5850)$	5853 ± 15	5830	255	0.602	$0.592 \pm 0.013 \pm 0.042 \pm 0.027$

Bibliography

- [1] S. Bethke, Prog. Part. Nucl. Phys. **58**, 351 (2007) [arXiv:hep-ex/0606035]; Nucl. Phys. Proc. Suppl. **135** (2004) 345; **121** (2003) 74; J. Phys. G **26** (2000) R27.
- [2] S. Eidelman *et al.* [Particle Data Group], Phys. Lett. B **592** (2004) 1.
- [3] M. Baldicchi, A. V. Nesterenko, G. M. Prospero, D. V. Shirkov and C. Simolo, Phys. Rev. Lett. **99** (2007) 242001 [arXiv:0705.0329 [hep-ph]].
- [4] M. Baldicchi, A. V. Nesterenko, G. M. Prospero and C. Simolo, arXiv:0705.1695 [hep-ph], to appear on Phys. Rev. D.
- [5] D. V. Shirkov, V. F. Kovalev, Phys. Rept. **352**, 219 (2001).
- [6] G. M. Prospero, M. Raciti and C. Simolo, Prog. Part. Nucl. Phys. **58** (2007) 387 [arXiv:hep-ph/0607209].
- [7] S. J. Brodsky, G. P. Lepage and P. B. Mackenzie, Phys. Rev. D **28** (1983) 228; S. J. Brodsky, C. R. Ji, A. Pang and D. G. Robertson, Phys. Rev. D **57** (1998) 245; G. Grunberg, Phys. Rev. D **46** (1992) 2228.
- [8] S. Ciulli and J. Fischer, Nucl. Phys. **24**, 465 (1961); J. Fischer, Fortschr. Phys. **42**, 665 (1994); I. Caprini and J. Fischer, Phys. Rev. D **60**, 054014 (1999); **62**, 054007 (2000); **68**, 114010 (2003); **71**, 094017 (2005); arXiv:hep-ph/0612274.
- [9] D.M. Howe and C.J. Maxwell, Phys. Rev. D **70**, 014002 (2004); P.M. Brooks and C.J. Maxwell, *ibid.* D **74**, 065012 (2006); C.J. Maxwell, arXiv:hep-ph/0610183.

- [10] G. Grunberg, Phys. Rev. D **29** (1984) 2315; Phys. Lett. B **95** (1980) 70 [Erratum-ibid. B **110** (1982) 501]; Phys. Rev. D **40** (1989) 680.
- [11] Yu. L. Dokshitzer, G. Marchesini and B. R. Webber, Nucl. Phys. B **469** (1996) 93.
- [12] S. J. Brodsky, S. Menke, C. Merino and J. Ratsham, Phys. Rev. D **67** (2003) 055008 and references therein.
- [13] (ALEPH Collaboration), R. Barate et al. Eur. Phys. J. C **4** (1998) 409; (OPAL Collaboration), K. Ackerstaff et al. Eur. Phys. J. C **7** (1999) 571. E. Braaten, S. Narison and A. Pich, Nucl. Phys. B **373** (1992) 581.
- [14] A. C. Mattingly and P. M. Stevenson, Phys. Rev. D **49** (1994) 437; P. M. Stevenson, Phys. Rev. D **23** (1981) 2916; Nucl. Phys. B **231** (1984) 65; J. Kubo, S. Sakakibara, and P. M. Stevenson, Phys. Rev. D **29** (1984) 1682; A. C. Mattingly and P. M. Stevenson, Phys. Rev. Lett. **69** (1992) 1320.
- [15] A. L. Kataev, S. A. Larin, and L. R. Surguladze, Phys. Rev. D **43** (1991) 1633; J. Chýla, A. Kataev, and S. Larin, Phys. Lett. B **267** (1991) 269.
- [16] D.V. Shirkov, Teor. Mat. Fiz. **136**, 3 (2003) [Theor. Math. Phys. **136**, 893 (2003)].
- [17] R. Alkofer and L. von Smekal, Phys. Rept. **353**, 281 (2001); P. Boucaud *et al.*, Nucl. Phys. Proc. Suppl. **106**, 266 (2002); J. Skullerud, A. Kizilersu, and A.G. Williams, Nucl. Phys. Proc. Suppl. **106**, 841 (2002).
- [18] J. L. Richardson, Phys. Lett. B **82** (1979) 272.
- [19] W. Buchmüller, G. Grunberg and S.-H. H. Tye, Phys. Rev. Lett. **45** (1980) 103; Phys. Rev. Lett. **45** (1980) 587; W. Fischler, Nucl. Phys. B **129** (1977) 157; A. Billoire, Phys. Lett. B **92** (1980) 343; M. Peter, Phys. Rev. Lett. **78** (1997) 602; Y. Schroder, Phys. Lett. B **447** (1999) 321.

- [20] E. Eichten and F. Feinberg, Phys. Rev. D **23** (1989) 2724; N. Brambilla, P. Consoli and G. M. Prosperi, Phys. Rev. D **50** (1994) 5878; Yu. A. Simonov, Nucl. Phys. B **324** (1989) 67.
- [21] S. Godfrey and N. Isgur, Phys. Rev. D **32** (1985) 189; T. Barnes, F. E. Close and S. Monaghan, Nucl. Phys. B **198** (1983) 380; G. M. Prosperi and M. Baldicchi, Fizika B **8** (1999) 251; T. Zhang and R. Koniuk, Phys. Lett. B **261** (1991) 311.
- [22] P. Ball, M. Beneke and V. M. Braun, Nucl. Phys. B **452** (1995) 563; J. Papavassiliou and J. M. Cornwall, Phys. Rev. D **44** (1991) 1285; J. H. Field, Phys. Rev. D **66** (2002) 013013;
- [23] D.V. Shirkov and I.L. Solovtsov, JINR Rapid Comm. **2**, 5 (1996); arXiv:hep-ph/9604363; Phys. Rev. Lett. **79**, 1209 (1997).
- [24] N. Brambilla, E. Montaldi, and G.M. Prosperi, Phys. Rev. D **54**, 3506 (1996); G.M. Prosperi, *Problems of Quantum Theory of Fields*, p. 381, B.M. Barbashov, G.V. Efimov, A.V. Efremov Eds. JINR Dubna 1999, arXiv:hep-ph/9906237.
- [25] M. B. Hecht, C. D. Roberts and S. M. Schmidt, Phys. Rev. C **63** (2001) 025213
- [26] F. Jugeau and H. Sazdjian, Nucl. Phys. B **670** (2003) 221; J. Mourad and H. Sazdjian, J. Phys. G **21** (1995) 267; J. Math. Phys. **35** (1994) 6379.
- [27] A. M. Badalian, B. L. G. Bakker and Yu. A. Simonov, Phys. Rev. D **75** (2007) 116001; A. M. Badalian and D. S. Kuzmenko, Phys. Rev. D **65** (2002) 016004.
- [28] D. Ebert, R. N. Faustov and V. O. Galkin, Mod. Phys. Lett. A **20** (2005) 1887; Eur. Phys. J. C **47** (2006) 745.
- [29] T. van Ritbergen, J. A. M. Vermaseren and S. A. Larin, Phys. Lett. B **400** (1997) 379.
- [30] W. E. Caswell and F. Wilczek, Phys. Lett. B **49** (1974) 291.
- [31] D. J. Gross and F. Wilczek, Phys. Rev. Lett. **30** (1973) 1343.

- [32] W. E. Caswell, Phys. Rev. Lett. **33** (1974) 244; D. R. T. Jones, Nucl. Phys. B **75** (1974) 531.
- [33] O. V. Tarasov, A. A. Vladimirov and A. Y. Zharkov, Phys. Lett. B **93** (1980) 429.
- [34] S. A. Larin and J. A. M. Vermaseren, Phys. Lett. B **303** (1993) 334.
- [35] M. Czakon, Nucl. Phys. B **710** (2005) 485; T. R. Morris and O. J. Rosten, arXiv:hep-th/0606189.
- [36] W. A. Bardeen, A. J. Buras, D. W. Duke and T. Muta, Phys. Rev. D **18** (1978) 3998.
- [37] J. C. Collins, *Renormalization*, Cambridge University Press (1984).
- [38] R. M. Corless, G. H. Gonnet, D. E. G. Hare, D. J. Jeffrey, and D. E. Knuth, Advances in Computation Mathematics, V **5** (1996) 329.
- [39] E. Gardi, G. Grunberg and M. Karliner, JHEP **9807** (1998) 007.
- [40] K. G. Chetyrkin, B. A. Kniehl and M. Steinhauser, Phys. Rev. Lett. **79** (1997) 2184.
- [41] D. S. Kurashev, arXiv:hep-ph/9912410.
- [42] D. S. Kurashev and B. A. Magradze, Theor. Math. Phys. **135** (2003) 531 [Teor. Mat. Fiz. **135** (2003) 95]; B. A. Magradze, arXiv:hep-ph/0305020.
- [43] B. A. Magradze, Few Body Syst. **40**, 71 (2006); arXiv:hep-ph/0512374.
- [44] A. V. Radyushkin, JINR Rapid Commun. **78** (1996) 96 [arXiv:hep-ph/9907228].
- [45] W. Celmaster and R. J. Gonsalves, Phys. Rev. D **20** (1979) 1420.
- [46] W. Bernreuther, A. Brandenburg and P. Uwer, Phys. Rev. Lett. **79** (1997) 189; K. G. Chetyrkin and J. H. Kuhn, Phys. Lett. B **406** (1997) 102.

- [47] J. A. M. Vermaseren, S. A. Larin and T. van Ritbergen, Phys. Lett. B **405** (1997) 327; K. G. Chetyrkin and A. Retey, Nucl. Phys. B **583** (2000) 3.
- [48] K. Melnikov and T. v. Ritbergen, Phys. Lett. B **482** (2000) 99.
- [49] S. A. Larin, T. van Ritbergen and J. A. M. Vermaseren, Nucl. Phys. B **438** (1995) 278; K. G. Chetyrkin, B. A. Kniehl and M. Steinhauser, Nucl. Phys. B **510** (1998) 61; G. Rodrigo, A. Pich and A. Santamaria, Phys. Lett. B **424** (1998) 367; G. Rodrigo and A. Santamaria, Phys. Lett. B **313** (1993) 441.
- [50] D. V. Shirkov, Nucl. Phys. B **371** (1992) 467; D. V. Shirkov and S. V. Mikhailov, Z. Phys. C **63** (1994) 463.
- [51] R. G. Moorhouse, M. R. Pennington and G. G. Ross, Nucl. Phys. B **124** (1977) 285.
- [52] S. L. Adler, Phys. Rev. D **10** (1974) 3714.
- [53] K. G. Chetyrkin, A. L. Kataev and F. V. Tkachov, Phys. Lett. B **85** (1979) 277; W. Celmaster, R. J. Gonsalves, Phys. Rev. Lett. **44** (1980) 560; M. Dine, J. R. Sapirstein, Phys. Rev. Lett. **43** (1979) 668; S. G. Gorishnii, A. L. Kataev and S. A. Larin, Phys. Lett. B **259** (1991) 144; L. R. Surguladze and M. A. Samuel, Phys. Rev. Lett. **66** (1991) 560 [Erratum-ibid. **66** (1991) 2416].
- [54] A. L. Kataev and V. V. Starshenko, Mod. Phys. Lett. A **10** (1995) 235.
- [55] J. D. Bjorken, SLAC-PUB-5103 *Invited lectures given at 1989 Cargese Summer Inst. in Particle Physics, Cargese, France, Jul 18 - Aug 4, 1989.*
- [56] M. R. Pennington and G. G. Ross, Phys. Lett. B **102** (1981) 167.
- [57] M. R. Pennington, R. G. Roberts and G. G. Ross, Nucl. Phys. B **242** (1984) 69.
- [58] N. V. Krasnikov and A. A. Pivovarov, Phys. Lett. B **116** (1982) 168.
- [59] H. F. Jones and I. L. Solovtsov, Phys. Lett. B **349** (1995) 519.

- [60] P.J. Redmond, Phys. Rev. **112**, 1404 (1958); P.J. Redmond and J.L. Uretsky, Phys. Rev. Lett. **1**, 147 (1958); N.N. Bogoliubov, A.A. Logunov, and D.V. Shirkov, Zh. Eksp. Teor. Fiz. **37**, 805 (1959) [Sov. Phys. JETP **37**, 574 (1960)].
- [61] D.V. Shirkov and I.L. Solovtsov, Phys. Lett. B **442**, 344 (1998); arXiv:hep-ph/9711251; Teor. Mat. Fiz. **120**, 482 (1999) [Theor. Math. Phys. **120**, 1220 (1999)]; arXiv:hep-ph/9909305.
- [62] K.A. Milton and I.L. Solovtsov, Phys. Rev. D **55**, 5295 (1997); **59**, 107701 (1999).
- [63] D.V. Shirkov and I.L. Solovtsov, Theor. Math. Phys. **150**, 132 (2007); arXiv:hep-ph/0611229.
- [64] A.P. Bakulev, S.V. Mikhailov and N.G. Stefanis, Phys. Rev. D **75**, 056005 (2007); arXiv:hep-ph/0607040.
- [65] D.V. Shirkov, Teor. Mat. Fiz. **119**, 55 (1999) [Theor. Math. Phys. **119**, 438 (1999)]; arXiv:hep-th/9810246; Lett. Math. Phys. **48**, 135 (1999).
- [66] B. A. Magradze, Int. J. Mod. Phys. A **15** (2000) 2715; arXiv:hep-ph/9808247.
- [67] B. A. Magradze, arXiv:hep-ph/0010070.
- [68] K. A. Milton, I. L. Solovtsov and O. P. Solovtsova, Phys. Lett. B **415** (1997) 104.
- [69] A. I. Alekseev, Few Body Syst. **32** (2003) 193.
- [70] A. I. Alekseev, Phys. Rev. D **61** (2000) 114005; A. I. Alekseev, Phys. Atom. Nucl. **65** (2002) 1678 [Yad. Fiz. **65** (2002) 1722]; J. Phys. G **27** (2001) L117.
- [71] A.V. Nesterenko, Int. J. Mod. Phys. A **18**, 5475 (2003); Int. J. Mod. Phys. A **19** (2004) 3471.
- [72] D.V. Shirkov and A.V. Zayakin, Yad. Fiz. **70**, 808 (2007) [Phys. Atom. Nucl. **70**, 775 (2007)]; arXiv:hep-ph/0512325.

- [73] A. P. Bakulev, K. Passek-Kumericki, W. Schroers and N. G. Stefanis, Phys. Rev. D **70** (2004) 033014 [Erratum-ibid. D **70** (2004) 079906].
- [74] K. A. Milton and O. P. Solovtsova, Phys. Rev. D **57** (1998) 5402; K. A. Milton and I. L. Solovtsov, Phys. Rev. D **55** (1997) 5295.
- [75] I. L. Solovtsov and D. V. Shirkov, Phys. Lett. B **442** (1998) 344.
- [76] D. V. Shirkov, Theor. Math. Phys. **127** (2001) 409; arXiv:hep-ph/0003242.
- [77] D. V. Shirkov, Eur. Phys. J. C **22** (2001) 331.
- [78] A. P. Bakulev, S. V. Mikhailov and N. G. Stefanis, Phys. Rev. D **75** (2007) 056005 [arXiv:hep-ph/0607040]; A. P. Bakulev, A. I. Karanikas and N. G. Stefanis, Phys. Rev. D **72** (2005) 074015.
- [79] J. S. Schwinger, Proc. Nat. Acad. Sci. **71**, 5047 (1974); K. A. Milton, Phys. Rev. D **10** (1974) 4247.
- [80] K. A. Milton and I. L. Solovtsov, Phys. Rev. D **59** (1999) 107701.
- [81] K. A. Milton, I. L. Solovtsov and O. P. Solovtsova, Phys. Lett. B **439** (1998) 421; Phys. Rev. D **60** (1999) 016001; K. A. Milton, I. L. Solovtsov, O. P. Solovtsova and V. I. Yasnov, Eur. Phys. J. C **14** (2000) 495; K. A. Milton, I. L. Solovtsov and O. P. Solovtsova, Phys. Rev. D **64** (2001) 016005; O. P. Solovtsova, Theor. Math. Phys. **134** (2003) 365 [Teor. Mat. Fiz. **134** (2003) 416]; B. V. Geshkenbein, B. L. Ioffe and K. N. Zyablyuk, Phys. Rev. D **64** (2001) 093009.
- [82] D. V. Shirkov, Theor. Math. Phys. **136** (2003) 893 [Teor. Mat. Fiz. **136** (2003) 3]; D. V. Shirkov, arXiv:hep-ph/0408272.
- [83] G. Cvetič and C. Valenzuela, J. Phys. G **32**, L27 (2006); Phys. Rev. D **74**, 114030 (2006); G. Cvetič, C. Valenzuela, and I. Schmidt, Nucl. Phys. Proc. Suppl. **164**, 308 (2007).
- [84] F. Schrempp, J. Phys. G **28** (2002) 915.
- [85] A. I. Alekseev and B. A. Arbuzov, Mod. Phys. Lett. A **20** (2005) 103; Mod. Phys. Lett. A **13** (1998) 1747; A. I. Alekseev, Theor. Math. Phys. **145** (2005) 1559 [Teor. Mat. Fiz. **145** (2005) 221]; Few Body Syst. **40**, 57 (2006); arXiv:hep-ph/0503242.

- [86] A. V. Nesterenko and I. L. Solovtsov, *Mod. Phys. Lett. A* **16** (2001) 2517; A. V. Nesterenko, *Phys. Rev. D* **62** (2000) 094028.
- [87] P.A. Raczka, *Nucl. Phys. Proc. Suppl.* **164**, 211 (2007); arXiv:hep-ph/0602085; arXiv:hep-ph/0608196.
- [88] N. V. Krasnikov and A. A. Pivovarov, *Phys. Atom. Nucl.* **64** (2001) 1500 [*Yad. Fiz.* **64** (2001) 1576].
- [89] B. R. Webber, *JHEP* **9810** (1998) 012.
- [90] A.V. Nesterenko and J. Papavassiliou, *J. Phys. G* **32**, 1025 (2006); arXiv:hep-ph/0507320; A. C. Aguilar, A. V. Nesterenko and J. Papavassiliou, *J. Phys. G* **31** (2005) 997.
- [91] Y. Nambu, *Phys. Lett. B* **80** (1979) 372. For recent developments see e.g. H. G. Dosch, M. Luscher and P. Weisz, *JHEP* **0207** (2002) 049; M. Billo, M. Caselle and L. Ferro, *JHEP* **0602** (2006) 070, and references therein.
- [92] H. G. Dosch, *Phys. Lett. B* **190** (1987) 177; H. G. Dosch and Yu. A. Simonov, *Phys. Lett. B* **205** (1988) 339.
- [93] M. Baker, J. S. Ball and F. Zachariasen, *Phys. Rev. D* **51** (1995) 1968; M. Baker, J. S. Ball, N. Brambilla, G. M. Prospero and F. Zachariasen, *Phys. Rev. D* **54** (1996) 2829 [Erratum-ibid. *D* **56** (1997) 2475]
- [94] M. Baldicchi and G.M. Prospero, *Phys. Rev. D* **66**, 074008 (2002); **62**, 114024 (2000); *Fizika B* **8**, 251 (1999); *Phys. Lett. B* **436**, 145 (1998).
- [95] M. Baldicchi and G.M. Prospero, *AIP Conf. Proc.* **756**, 152 (2005); *Color Confinement and Hadrons in Quantum Chromodynamics*, p. 183, H. Suganuma, *et al.* eds. World Scientific 2004, arXiv:hep-ph/0310213.
- [96] M. Baldicchi, G.M. Prospero, and C. Simolo, *AIP Conf. Proc.* **892** (2007) 340 [arXiv:hep-ph/0611087].

Part II

Progress in the determination of the gluon polarization

Chapter 5

Polarized parton distributions from DIS

One of the fundamental properties of the nucleon structure is the spin distribution among its quark and gluon constituents. The spin structure of the nucleon has been extensively investigated by inclusive polarized lepton scattering off polarized protons and neutrons, since the discovery of the EMC spin effect [1]. Despite the naive expectation that the nucleon spin is carried by quarks, the experimental results revealed that only a small fraction is actually due to quarks (the so-called “proton spin crisis”). Considerable efforts, both experimentally and theoretically, have subsequently gone into understanding where the remaining fraction of the nucleon spin resides (see e.g. Ref. [2] for a recent review).

To this end, the determination of the first moments of the polarized parton distribution functions (pdfs) is necessary. Attention is currently devoted to the reconstruction of pdfs at all values of the Bjorken x and the momentum transfer Q^2 . Of special interest is the determination of the gluon polarization, in order to evaluate the total contribution carried by the gluons to the nucleon spin.

The possibility of inferring the polarized gluon density from scaling violations has been extensively studied. However, phenomenological analyses of the current inclusive DIS data only yield weak constraints on the gluon first moment, and leave the x -shape completely undetermined. This issue has been thoroughly investigated in the present work, by performing a NLO

analysis in perturbative QCD of world data from inclusive DIS experiments, as discussed in detail in Sec. 6.

Actually, some light may be shed on the gluon content of the nucleon by observing specific events that receive leading contributions from gluon initiated subprocesses, that is, by directly measuring the polarized gluon density. In particular, as discussed in Sec. 7, in polarized fixed target experiments, the gluon polarization can be probed through the photon-gluon fusion process, by selecting open-charm events or hadron pairs with high transverse momentum, and both strategies are currently used at the COMPASS experiment (CERN). Indeed charmed mesons in the final states provide a clean tag of photon-gluon fusion, since there are essentially no competing processes and a clean perturbative analysis is possible. Therefore, a phenomenological study of open-charm photoproduction from deep-inelastic muon scattering off nucleons, with longitudinally polarized beam and target, has been also performed, with reference to upcoming results on experimental asymmetries from COMPASS. The results are presented in Sec. 7 and, specifically, the constraints that can be obtained on the polarized gluon density at the COMPASS kinematics are discussed.

In what follows the main theoretical tools are briefly reviewed. Specifically Sec. 5.1 recalls the basic ingredients for the study of polarized lepton-nucleon scattering, i.e. the polarized structure functions g_1 and g_2 . In Sec. 5.2 the expectations of the naive quark-parton model are summarized, whereas Sec. 5.3 is devoted to the main aspects of the perturbative QCD analysis, that is, the relations between structure functions and polarized parton distributions. In Sec. 5.4 the way experimental information on the relevant structure function g_1 are extracted from the experimentally measured quantities is described, and, finally Sec 5.5 sketches how target mass corrections are taken into account in the present analysis.

5.1 Structure functions and their moments

Polarized structure functions are the form factors which parametrize the cross section for deep-inelastic scattering of polarized leptons off a polarized hadronic target. If the momentum transfer Q^2 involved is much smaller than the Z boson mass, the antisymmetric part of the hadronic tensor can

be expressed in terms of two spin-dependent structure functions, g_1 and g_2 , i.e. [3, 4]

$$\begin{aligned} iW_A^{\mu\nu} &\equiv \frac{1}{4\pi} \int d^4x e^{iqx} \langle p, s | J^{[\mu}(x) J^{\nu]}(0) | p, s \rangle \\ &= im\varepsilon^{\mu\nu\rho\sigma} q_\rho \left[\frac{s_\sigma}{pq} g_1(x, Q^2) + \frac{s_\sigma pq - p_\sigma qs}{(pq)^2} g_2(x, Q^2) \right] \end{aligned} \quad (5.1)$$

where p^μ , m and s^μ are, respectively, the target four-momentum, mass, and spin (normalized as $s^\mu s_\mu = -1$). Neglecting weak interaction effects, J^μ in Eq. (5.1) is the electric current. The deeply inelastic region is identified by the Bjorken limit

$$Q^2 = -q^2 \rightarrow \infty, \quad \text{with } x = \frac{Q^2}{2pq} \text{ fixed}, \quad (5.2)$$

in which the invariant mass of the hadronic system in the final state is much larger than the nucleon mass, namely

$$W^2 = m^2 + Q^2 \frac{1-x}{x} \gg m^2. \quad (5.3)$$

In the case when the nucleon spin s is purely longitudinal, that is,

$$s = s_L = \lambda \left(p - \frac{m^2}{pq} q \right), \quad \lambda = \pm \frac{1}{m\sqrt{1 + 4m^2x^2/Q^2}}, \quad (5.4)$$

the antisymmetric tensor Eq. (5.1) can be written as

$$W_A^{\mu\nu} = \lambda m \varepsilon^{\mu\nu\rho\sigma} \frac{q_\rho p_\sigma}{pq} \left[g_1(x, Q^2) - \frac{4m^2x^2}{Q^2} g_2(x, Q^2) \right]. \quad (5.5)$$

In the Bjorken limit the product $\lambda m \rightarrow 1$, thus leaving a finite residue as $m \rightarrow 0$. Furthermore, the factor $4m^2x^2/Q^2$ vanishes, and the structure function g_2 decouples. As a result only g_1 is asymptotically relevant.

In case of transverse polarization both structure functions equally contribute, but the whole cross section is strongly suppressed by an overall target mass factor.

The light-cone expansion of the current product in Eq. (5.1) implies that the first moment of the relevant structure function g_1 for a nucleon target, at

leading twist, is given by [5]

$$\Gamma_1(Q^2) \equiv \int_0^1 dx g_1(x, Q^2) = \frac{1}{2} \left[\sum_{i=1}^{n_f} e_i^2 C_i(Q^2) a_i \right], \quad (5.6)$$

where a_i are given by matrix elements of the axial current for the i -th flavor, namely

$$ma_i s_\mu \equiv \langle p, s | \bar{\psi}_i \gamma_\mu \gamma_5 \psi_i | p, s \rangle, \quad (5.7)$$

e_i is the electric charge, and $C_i(Q^2)$ are perturbatively calculable coefficient functions. Then, assuming that only the three lightest flavors are activated, Eq. (5.6) can be recast as

$$\Gamma_1^{p,n}(Q^2) = \frac{1}{12} \left[C_{\text{NS}}(Q^2) \left(\pm a_3 + \frac{1}{3} a_8 \right) + \frac{4}{3} C_{\text{S}}(Q^2) a_0 \right], \quad (5.8)$$

where the plus (minus) sign refers to a proton (neutron) target, and the singlet and nonsinglet matrix elements are defined by

$$\begin{aligned} a_0 &= a_u + a_d + a_s \\ a_3 &= a_u - a_d, \quad a_8 = a_u + a_d - 2a_s \end{aligned} \quad (5.9)$$

respectively. $C_{\text{S}}(Q^2)$ and $C_{\text{NS}}(Q^2)$ are Q^2 -dependent singlet and nonsinglet QCD coefficient functions; to order α_s , in the $\overline{\text{MS}}$ scheme e.g., one has

$$C_{\text{S}}(Q^2) = C_{\text{NS}}(Q^2) = 1 - \frac{\alpha_s}{\pi} + \mathcal{O}(\alpha_s^2), \quad (5.10)$$

whereas $C_{\text{S}} \neq C_{\text{NS}}$ at higher orders [6]. QCD corrections turn out to be sizable in the Q^2 -range of the present experiments and are thus relevant for the comparison with the data [7].

The singlet and nonsinglet components of Γ_1 can be then extracted using Eq. (5.8). Indeed, the triplet and octet currents are conserved and therefore scale invariant, and the related matrix elements can be derived from any other process. The triplet axial charge is equal to the axial coupling measured in nucleon β -decay

$$a_3 = \frac{g_A}{g_V} = F + D = 1.2601 \pm 0.0025 \quad (5.11)$$

where F and D are weak hyperon decay constants in flavor SU(3) symmetry [8, 9]. The octet matrix element is then given by

$$a_8 = 3F - D = 0.588 \pm 0.033. \quad (5.12)$$

On the other hand, the singlet axial charge a_0 is scale dependent due to the anomalous nonconservation of the singlet axial current [10], and can be determined from a measurement of the proton first moment, by rewriting Eq. (5.8) as

$$C_S(Q^2)a_0(Q^2) = 9\Gamma_1^p(Q^2) - \frac{1}{2}C_{\text{NS}}(Q^2)(3F + D). \quad (5.13)$$

Since the two terms on the right hand side are roughly of the same order (typically $\Gamma_1 \sim 0.1$), the value of a_0 arises from a large cancellation between them (see e.g. [4]). Present data indeed indicate that a_0 is compatible with zero, but values as large as $a_0(10 \text{ GeV}^2) \sim 0.3$ are not excluded.

Finally, a fundamental prediction of the theory is the Bjorken sum rule

$$\Gamma_1^p(Q^2) - \Gamma_1^n(Q^2) = \frac{1}{6}C_{\text{NS}}(Q^2) a_3, \quad (5.14)$$

that was originally derived from current algebra and isospin symmetry [11]. Eq. (5.14) relates the integral over all x of the nonsinglet polarized structure function $g_1^p - g_1^n$, at fixed Q^2 , to the well-measured β -decay coupling a_3 . A comparison with the data, using the computed $C_{\text{NS}}(Q^2)$ thus allows a direct test of isospin in this channel, as well as the predicted scale dependence. In addition, it is possible to use the measurements to extract a relatively accurate determination of the strong coupling $\alpha_s(Q^2)$ [12].

5.2 The parton model predictions

In the naive quark-parton model the spin-dependent structure function g_1 can be simply expressed as the charge-weighted difference between momentum distributions for quark helicities aligned parallel (q^\uparrow) and antiparallel (q^\downarrow) to the longitudinally polarized parent nucleon

$$g_1(x) = \frac{1}{2} \sum_{i=1}^{n_f} e_i^2 \Delta q^+(x), \quad \Delta q^+(x) = \Delta q_i(x) + \Delta \bar{q}_i(x). \quad (5.15)$$

The polarized quark distributions are defined as

$$\Delta q_i(x) = q_i^\uparrow(x) - q_i^\downarrow(x), \quad (5.16)$$

and similarly for antiquarks. Assuming $n_f = 3$, one can define the flavor singlet and nonsinglet combinations of polarized quark densities, namely

$$\begin{aligned}\Delta\Sigma &= \Delta u^+ + \Delta d^+ + \Delta s^+ \\ \Delta q_3 &= \Delta u^+ - \Delta d^+ \\ \Delta q_8 &= \Delta u^+ + \Delta d^+ - 2\Delta s^+.\end{aligned}\tag{5.17}$$

Then the structure function g_1 can be cast into the form

$$g_1^{p,n}(x) = \frac{\langle e^2 \rangle}{2} \left[\Delta\Sigma(x) \pm \frac{3}{4}\Delta q_3(x) + \frac{1}{4}\Delta q_8(x) \right],\tag{5.18}$$

where the plus (minus) sign stays for a proton (neutron) target, and the average charge is $\langle e^2 \rangle = 2/9$ for $n_f = 3$.

In the naive parton model gluons do not contribute to the nucleon spin, and the first moments of singlet and nonsinglet quark densities are straightforwardly related to the matrix elements of axial currents, such that

$$a_0 = \int_0^1 dx \Delta\Sigma(x), \quad a_3 = \int_0^1 dx \Delta q_3(x) \quad \text{and} \quad a_8 = \int_0^1 dx \Delta q_8(x).\tag{5.19}$$

In this context, the first moments of $\Delta q_i^+(x)$ can be interpreted as the contribution of the quark flavor i to the nucleon spin, and thus the singlet axial charge a_0 as the net quark helicity.

Then, under the assumption that the strange sea in the nucleon is unpolarized, namely

$$\left| \int_0^1 dx \Delta s^+(x) \right| \ll \left| \int_0^1 dx \Delta q^+(x) \right|_{q=u,d},\tag{5.20}$$

the quark helicity coincides with the nonsinglet (octet) axial charge, $a_0 \simeq a_8$. Thus, from Eq. (5.12) one roughly has

$$a_0 \simeq 0.6,\tag{5.21}$$

whereas the value extracted from the data (see Eq. (5.13)) is compatible with zero. The Ellis-Jaffe sum rules [13] then give the parton model predictions for the proton and neutron first moments

$$\Gamma_1^{p,n} = \pm \frac{1}{12}a_3 + \frac{5}{36}a_8,\tag{5.22}$$

that are not consistent with the measured values, at the level of several standard deviations. Thus, against the Ellis-Jaffe prediction and intuition, quarks seem to carry a very small fraction of the total nucleon helicity. Actually, it is only at the naive parton level that the first moment of the singlet part of the structure function g_1 corresponds to the total helicity fraction carried by quarks.

5.3 Polarized structure functions and pdfs in QCD

When including QCD corrections, also the gluon density contributes and the structure function g_1 is related to the scale-dependent polarized quark and gluon distributions by the convolution with appropriate coefficient functions [17, 18]

$$g_1(x, Q^2) = \frac{\langle e^2 \rangle}{2} [C_{\text{NS}} \otimes \Delta q_{\text{NS}} + C_{\text{S}} \otimes \Delta \Sigma + 2n_f C_g \otimes \Delta g], \quad (5.23)$$

where $\langle e^2 \rangle = n_f^{-1} \sum_{i=1}^{n_f} e_i^2$, n_f being the number of active flavors with electric charge e_i , and \otimes denotes the convolution product with respect to x

$$f \otimes g = \int_x^1 \frac{dy}{y} f\left(\frac{x}{y}\right) g(y). \quad (5.24)$$

In Eq. (5.23) $\Delta g(x, Q^2)$ is the polarized gluon distribution, whereas the singlet and nonsinglet quark distributions are defined as

$$\begin{aligned} \Delta \Sigma(x, Q^2) &\equiv \sum_{i=1}^{n_f} (\Delta q_i + \Delta \bar{q}_i) \\ \Delta q_{\text{NS}}(x, Q^2) &\equiv \sum_{i=1}^{n_f} \left(\frac{e_i^2}{\langle e^2 \rangle} - 1 \right) (\Delta q_i + \Delta \bar{q}_i), \end{aligned} \quad (5.25)$$

where Δq_i and $\Delta \bar{q}_i$ are the scale-dependent quark and antiquark polarized densities of flavor i , defined as in Eq. (5.16).

The perturbative part of the Q^2 -dependence of the polarized parton densities is given by the Altarelli-Parisi evolution equations [19]. The singlet quark

and gluon distributions mix according to

$$\frac{\partial}{\partial \ln t} \begin{pmatrix} \Delta \Sigma \\ \Delta g \end{pmatrix} = \frac{\alpha_s(t)}{2\pi} \begin{pmatrix} \Delta P_{qq}^S & 2n_f \Delta P_{qg}^S \\ \Delta P_{gq}^S & \Delta P_{gg}^S \end{pmatrix} \otimes \begin{pmatrix} \Delta \Sigma \\ \Delta g \end{pmatrix}, \quad (5.26)$$

while the nonsinglet quark evolves independently as

$$\frac{\partial}{\partial \ln t} \Delta q_{\text{NS}} = \frac{\alpha_s(t)}{2\pi} \Delta P_{qq}^{\text{NS}} \otimes \Delta q_{\text{NS}}. \quad (5.27)$$

In Eqs. (5.26) and (5.27) $\Delta P(x, Q^2)$ denote the spin-dependent splitting functions, and $t = \ln(Q^2/\Lambda^2)$ with Λ the QCD scale parameter. The factorization and renormalization scales are both taken equal to Q^2 , so that all the scale dependence appears through t .

Eqs. (5.26) and (5.27) are valid for all orders of perturbative QCD; the coefficient functions C and the evolution kernels ΔP may each be expanded in powers of α_s . At NLO

$$C(x, \alpha_s) = C^{(0)}(x) + \frac{\alpha_s(t)}{2\pi} C^{(1)}(x) + \mathcal{O}(\alpha_s^2) \quad (5.28)$$

$$\Delta P(x, \alpha_s) = \Delta P^{(0)}(x) + \frac{\alpha_s(t)}{2\pi} \Delta P^{(1)}(x) + \mathcal{O}(\alpha_s^2). \quad (5.29)$$

It is also convenient to introduce anomalous dimensions

$$\gamma(n, \alpha_s) \equiv \int_0^1 dx x^{n-1} \Delta P(x, \alpha_s) \quad (5.30)$$

i.e. the Mellin transforms of the splitting functions. One can analogously define moment-space coefficient functions $C(n, \alpha_s)$ and parton distributions $\Delta q_{\text{NS}}(n, Q^2)$, $\Delta \Sigma(n, Q^2)$ and $\Delta g(n, Q^2)$.

In accordance with the partonic picture, in Eq. (5.28) $C_{\text{NS}}^{(0)}(x) = C_{\text{S}}^{(0)}(x) = \delta(1-x)$, while $C_g^{(0)}(x) = 0$, so that at order α_s^0 g_1 decouples from Δg , and is just a linear combination of polarized quark distributions, whose Q^2 dependence is entirely specified by Eqs. (5.26) and (5.27) (the leading order splitting functions are calculated in Ref. [19]).

Beyond leading order, splitting functions and coefficient functions are no longer universal, hence even though the scale dependence of the observable structure function g_1 is determined uniquely, at least up to higher order corrections, its separation into contributions due to quarks and gluons is scheme

dependent and thus essentially arbitrary. The NLO coefficient functions may be modified by a change of the factorization scheme which is partially compensated by a corresponding change in the NLO anomalous dimensions, hence both are required in a full NLO order computation. The complete set of NLO coefficient functions and splitting functions can be found in Ref. [6]. The modified minimal subtraction ($\overline{\text{MS}}$) factorization scheme is commonly used in the analysis of polarized parton distributions. In the $\overline{\text{MS}}$ scheme the first moment of the gluon coefficient function vanishes, the gluon density does not contribute to the first moment of g_1 and the scale dependent singlet axial charge is thus equal to the singlet quark first moment

$$a_0(Q^2) = \Delta\Sigma_{\overline{\text{MS}}}(1, Q^2). \quad (5.31)$$

Alternatively, one can define a different scheme, the Adler-Bardeen (AB) scheme [10], such that the singlet quark first moment is conserved at all orders and can be identified with the total quark helicity, whereas the polarized gluon density is defined as in the $\overline{\text{MS}}$ scheme. In the AB scheme the gluon polarization directly contributes to the singlet axial charge (and thus to the first moment of g_1), which is now written as

$$a_0(Q^2) = \Delta\Sigma_{\text{AB}}(1) - n_f \frac{\alpha_s(Q^2)}{2\pi} \Delta g(1, Q^2). \quad (5.32)$$

Eqs. (5.31) and (5.32) then yield the relation between the first moments of the singlet quark distributions in the two schemes. They differ by the product $\alpha_s(Q^2)\Delta g(1, Q^2)$, which is due to the anomalous nonconservation of the singlet axial current [10], and is scale invariant at leading order; this implies that $\Delta g(1, Q^2)$ increases as $1/\alpha_s(Q^2)$ with Q^2 , and the gluon contribution in Eq. (5.32) is not asymptotically suppressed by powers of α_s . As a result, this scheme dependence does not vanish at large Q^2 , and the definition of the singlet quark first moment is therefore maximally ambiguous.

In the AB scheme, which will be adopted in the following phenomenological analysis (see Sec. 6), the first moment of the gluon coefficient function at NLO reads [10]

$$C_g(1, \alpha_s) = -\frac{\alpha_s}{4\pi} + \mathcal{O}(\alpha_s^2), \quad (5.33)$$

and the first moment of the structure function g_1 is given at NLO by

$$\Gamma_1(Q^2) \equiv \int_0^1 dx g_1(x, Q^2) = \quad (5.34)$$

$$\frac{\langle e^2 \rangle}{2} \left[\left(1 - \frac{\alpha_s}{\pi}\right) (\Delta q_{\text{NS}}(1, Q^2) + \Delta \Sigma(1, Q^2)) - n_f \frac{\alpha_s}{2\pi} \Delta g(1, Q^2) \right].$$

Different factorization schemes were also discussed in Refs. [20], and the dependence of the results of phenomenological analyses of spin-dependent pdfs on the choice of the scheme was studied.

It should be finally noted that a number of theoretical models attempt to explain the quark helicity distribution within the nucleon and the unexpected smallness of the singlet axial charge. A possible interpretation is to assume a large and negative contribution from the strange sea polarization Δs^+ . This suppression of the axial charge might be explained by invoking nonperturbative mechanisms based on instanton-like vacuum configuration [14]. In this case $\Delta s = \Delta \bar{s}$. Another scenario is possible, where the smallness of the singlet axial charge is due to the intrinsic strangeness, i.e. the C-even strange combination is large, but Δs differs significantly from $\Delta \bar{s}$. Specifically, in the Skyrme models of the nucleon [16] the strange distribution (in particular its first moment) is large, while the antistrange distribution is much smaller and does not sizably contribute to the axial charge [15].

Finally, another possible mechanism has been proposed to understand the nucleon spin structure (see [12] and references therein), which includes the gluon contribution. Indeed, in the Adler-Bardeen scheme, one can assume, on the basis of Eq. (5.32), that a cancellation between a large (scale-independent) singlet quark distribution and a large gluon polarization takes place. In this case $\Delta s^+ \ll \Delta u^+, \Delta d^+$, as expected in the parton model.

5.4 Phenomenology of g_1

Experimental information on the structure functions $g_1(x, Q^2)$ and $g_2(x, Q^2)$ are extracted from measurements of spin-asymmetries. Longitudinally polarized leptons are scattered off a hadronic target that is polarized either longitudinally or transversely. The longitudinal (A_{\parallel}) and transverse (A_{\perp}) asymmetries are formed by combining data taken with opposite beam helicity

$$A_{\parallel} = \frac{\sigma^{\uparrow\downarrow} - \sigma^{\uparrow\uparrow}}{\sigma^{\uparrow\downarrow} + \sigma^{\uparrow\uparrow}}, \quad A_{\perp} = \frac{\sigma^{\downarrow\rightarrow} - \sigma^{\uparrow\rightarrow}}{\sigma^{\downarrow\rightarrow} + \sigma^{\uparrow\rightarrow}}. \quad (5.35)$$

The symbols $\sigma^{\uparrow\uparrow}$ and $\sigma^{\uparrow\downarrow}$ denote the cross sections for the lepton-nucleon scattering with their parallel and antiparallel helicity states, respectively,

whereas $\sigma^{\uparrow\rightarrow}$ and $\sigma^{\downarrow\rightarrow}$ represent the scattering cross sections for transversely polarized nucleon targets.

The asymmetries A_{\parallel} and A_{\perp} are related to the photon absorption cross section asymmetries A_1 and A_2 by the relations

$$A_{\parallel} = D(A_1 + \eta A_2), \quad A_{\perp} = d(A_2 - \zeta A_1), \quad (5.36)$$

where

$$A_1(x, Q^2) = \frac{\sigma_{1/2}^T - \sigma_{3/2}^T}{\sigma_{1/2}^T + \sigma_{3/2}^T}, \quad A_2(x, Q^2) = \frac{2\sigma^{LT}}{\sigma_{1/2}^T + \sigma_{3/2}^T}. \quad (5.37)$$

Here, $\sigma_{1/2}^T$ and $\sigma_{3/2}^T$ represent the absorption cross sections of virtual transverse photons for the total helicity of the photon-nucleon system of 1/2 and 3/2 respectively; σ^{LT} denotes the interference term between the transverse and longitudinal photon-nucleon amplitudes.

The factor D in the first of Eqs. (5.36) is interpreted as the depolarization of the photon with respect to the primary lepton beam

$$D = \frac{y(1 + \gamma^2 y/2)(2 - y)}{y^2(1 + \gamma^2) + 2(1 + R)(1 - y - \gamma^2 y^2/4)}, \quad (5.38)$$

and depends upon the kinematic factors

$$y = 1 - \frac{E'}{E} \quad \text{and} \quad \gamma = \frac{2mx}{\sqrt{Q^2}} \quad (5.39)$$

where y is the fractional energy lost by the lepton. The depolarization factor also depends on the ratio $R(x, Q^2)$ of the cross sections for the longitudinally polarized photon to the transverse one, and is experimentally measured. Moreover,

$$\eta = \frac{\gamma(1 - y - \gamma^2 y^2/4)}{(1 + \gamma^2 y/2)(1 - y/2)}. \quad (5.40)$$

The kinematic factors in the second of Eqs. (5.36) are given respectively by

$$d = \frac{D\sqrt{1 - y - \gamma^2 y^2/4}}{1 - y/2}, \quad \zeta = \frac{\gamma(1 - y/2)}{1 + \gamma^2 y/2}. \quad (5.41)$$

Then, the asymmetries A_1 and A_2 can be related to the polarized structure functions g_1 and g_2 by

$$A_1(x, Q^2) = \frac{g_1(x, Q^2) - \gamma^2 g_2(x, Q^2)}{F_1(x, Q^2)}, \quad A_2(x, Q^2) = \frac{\gamma(g_1(x, Q^2) + g_2(x, Q^2))}{F_1(x, Q^2)}, \quad (5.42)$$

where $F_1(x, Q^2)$ is the unpolarized structure function of the nucleon. If both the longitudinal and transverse asymmetries, A_{\parallel} and A_{\perp} , are measured, one can extract both structure functions, $g_1(x, Q^2)$ and $g_2(x, Q^2)$ from experimental data with minimal assumptions, using the relations

$$g_1(x, Q^2) = \frac{F_1(x, Q^2)}{(1 + \gamma^2)(1 + \eta\zeta)} \left[(1 + \gamma\zeta) \frac{A_{\parallel}}{D} - (\eta - \gamma) \frac{A_{\perp}}{d} \right], \quad (5.43)$$

$$g_2(x, Q^2) = \frac{F_1(x, Q^2)}{(1 + \gamma^2)(1 + \eta\zeta)} \left[\left(\frac{\zeta}{\gamma} - 1 \right) \frac{A_{\parallel}}{D} + \left(\eta + \frac{1}{\gamma} \right) \frac{A_{\perp}}{d} \right] \quad (5.44)$$

Actually, the transverse asymmetry is generally poorly determined, and in most cases only the longitudinal asymmetry A_{\parallel} is measured. In this case, the relevant structure function g_1 can be expressed via the observable A_{\parallel} and the unknown structure function g_2 , namely

$$g_1(x, Q^2) = \frac{F_1(x, Q^2) A_{\parallel}}{(1 + \gamma\eta) D} + \frac{\gamma(\gamma - \eta)}{\gamma\eta + 1} g_2(x, Q^2). \quad (5.45)$$

An experimental determination of g_1 thus relies on a theoretical assumption on g_2 . In Eq. (5.45) F_1 is expressed in terms of the unpolarized structure function F_2 , usually extracted from unpolarized DIS experiments, i.e.

$$F_1(x, Q^2) = \frac{F_2(x, Q^2)}{2x(1 + R(x, Q^2))} (1 + \gamma^2). \quad (5.46)$$

Then, as discussed in Sec. 6, parametrizations for the unpolarized structure function $F_2(x, Q^2)$ and the ratio $R(x, Q^2)$ of longitudinal and transverse virtual photo-absorption cross sections must be used in order to extract experimental information on the structure function $g_1(x, Q^2)$.

Finally, the experimentally measured counting rate asymmetry A_{exp} is related to the cross section asymmetry A_{\parallel} by

$$A_{\text{exp}} = f_t P_t P_b A_{\parallel}, \quad (5.47)$$

where P_b is the beam polarization, P_t the polarization of the target nucleon, and f_t the target dilution factor, i.e. the fraction of polarized nucleons in the target material.

Relations (5.45) and (5.46) simplify if the nucleon mass m is neglected. Indeed, in this case the kinematic factor $\gamma \simeq 0$, and the structure function g_2

decouples. This is generally a reasonable approximation in the small- x or large- Q^2 region, where the factor γ^2 is of the order of $10^{-2} - 10^{-3}$. Then, one simply has

$$g_1(x, Q^2) \simeq \frac{F_2(x, Q^2)}{2x(1 + R(x, Q^2))} A_1, \quad \text{with} \quad A_1 \simeq \frac{A_{\parallel}}{D}. \quad (5.48)$$

It should be finally noted that some of the experimental measurements concern the asymmetry A_1 (or A_{\parallel}), while others concern values of the combination of A_{\parallel} and A_{\perp} which corresponds to g_1/F_1 . The two quantities coincide for $m = 0$ (aside from the depolarization factor in the case of A_{\parallel}), but they do not when mass corrections are included. Then, in the case A_1 is measured, the related theoretical asymmetry is given by $[g_1 - (4m^2x^2/Q^2)g_2]/F_1$ (or by the similar relation obtained by Eq. (5.45) if A_{\parallel} is measured), in the second case simply by g_1/F_1 .

5.5 Target mass corrections

A large part of experimental data in polarized deep-inelastic scattering are taken at relatively low values of Q^2 . Specifically, Q^2 is usually around few GeV^2 for data points in the small- x region (data at $Q^2 < 1\text{GeV}^2$ are also available, but they are usually not included in perturbative analyses). In this kinematical region, contributions suppressed by inverse powers of Q^2 arise when taking into account the finite value of the nucleon mass m , and could play a relevant role.

Another source of power-suppressed terms originate from the operator product expansion of the hadronic tensor $W_A^{\mu\nu}$ in Eq. (5.1), i.e. from matrix elements of operators of non-leading twist (see e.g. [5]). These contributions are usually referred to as dynamical higher twist, and their effect can not be calculated in perturbation theory, so that it is difficult to assess their relevance in any phenomenological analysis of polarized pdfs.

When considering target mass corrections, in order to obtain experimental information on g_1 from the measured asymmetry A_{\parallel} , the complete relation Eq. (5.45) must be used (or the first of Eq. (5.42) if the data concern A_1), that is, all the kinematical factors must be retained. Moreover, also the structure function g_2 now contributes when comparing the theoretically predicted

observable g_1 to the data. However, experimental data on the structure function g_2 are restricted to a limited range in the (x, Q^2) -plane and are affected by large uncertainties (see e.g. [21]). Therefore, a model for g_2 is usually invoked in phenomenological analyses.

To take target mass corrections into account, following Ref. [22], the moments of the polarized structure functions g_1 and g_2 can be expressed in terms of the matrix elements of the twist-2 and 3 operators appearing in the light-cone expansion of the forward scattering amplitude. Specifically, at the first order in m^2/Q^2 , the n -th moments of g_1 and g_2 read [22]

$$\begin{aligned} g_1^n(Q^2) &= a_n + \frac{m^2}{Q^2} \frac{n(n+1)}{(n+2)^2} (n a_{n+2} + 4 d_{n+2}) + \mathcal{O}\left(\frac{m^4}{Q^4}\right) \\ g_2^n(Q^2) &= \frac{n-1}{n} (d_n - a_n) + \frac{m^2}{Q^2} \frac{n(n-1)}{(n+2)^2} [n d_{n+2} - (n+1) a_{n+2}] + \mathcal{O}\left(\frac{m^4}{Q^4}\right). \end{aligned} \quad (5.49)$$

Here, a_n and d_n are given by matrix elements of the twist-2 and 3 polarized operators

$$\begin{aligned} \langle p, s | i^{n-1} [\bar{\psi} \gamma_5 \gamma^\sigma D^{\mu_1} \dots D^{\mu_{n-1}} \lambda_i \psi]_S | p, s \rangle &= -m a_n M_1^{\sigma \mu_1 \dots \mu_{n-1}} \\ \langle p, s | i^{n-1} [\bar{\psi} \gamma_5 \gamma^\lambda D^\sigma D^{\mu_1} \dots D^{\mu_{n-2}} \lambda_i \psi]_{S'} | p, s \rangle &= m d_n M_2^{\lambda \sigma \mu_1 \dots \mu_{n-2}} \end{aligned} \quad (5.50)$$

where m, p and s are mass, four-momentum and spin of the target nucleon, the symbol $[\dots]_S$ means complete symmetrization in the indices $\sigma, \mu_1 \dots \mu_{n-1}$, whereas $[\dots]_{S'}$ denotes antisymmetrization with respect to λ and σ and symmetrization over the other indices. The symbol $M_1^{\sigma \mu_1 \dots \mu_{n-1}}$ denotes the most general rank- n tensor which can be formed with one spin four-vector s and $n-1$ momentum four-vectors p ; similarly $M_2^{\lambda \sigma \mu_1 \dots \mu_{n-2}}$ is antisymmetric in λ and σ and symmetric in all other indices.

If $m=0$ is taken in Eqs. (5.49) the n -th moments of the structure functions (aside from QCD perturbative corrections) reduce to the simple form [23]

$$\begin{aligned} g_{10}^n(Q^2) &= a_n + \mathcal{O}\left(\frac{m^2}{Q^2}\right) \\ g_{20}^n(Q^2) &= \frac{n-1}{n} (d_n - a_n) + \mathcal{O}\left(\frac{m^2}{Q^2}\right). \end{aligned} \quad (5.51)$$

One can then use Eq.s (5.51) to eliminate the matrix elements a_n and d_n from Eq.s (5.49) in favour of the n -th moments of the structure functions at

zero nucleon mass, i.e. g_{10}^n and g_{20}^n . Then, to order $\mathcal{O}(m^2/Q^2)$ one has [22]

$$\begin{aligned} g_1^n(Q^2) &= g_{10}^n(Q^2) + \frac{m^2}{Q^2} \frac{n(n+1)}{(n+2)^2} \left[(n+4)g_{10}^{n+2}(Q^2) + \frac{4(n+2)}{(n+1)}g_{20}^{n+2}(Q^2) \right] \\ g_2^n(Q^2) &= g_{20}^n(Q^2) + \frac{m^2}{Q^2} \frac{n(n-1)}{(n+2)^2} \left[\frac{n(n+2)}{(n+1)}g_{20}^{n+2}(Q^2) - g_{10}^{n+2}(Q^2) \right]. \end{aligned} \quad (5.52)$$

If $d_n = 0$, the structure functions obey the so-called Wandzura-Wilczek relation [24]

$$g_2^n(Q^2) = -\frac{n-1}{n} g_1^n(Q^2). \quad (5.53)$$

Actually, twist-3 contributions are not power-suppressed with respect to the leading twist; however, if $d_n \ll a_n$ is assumed, one can then use Eq. (5.53) to express g_1^n and g_2^n in Eqs. (5.52) in terms of the zero-mass structure function g_{10}^n alone, namely

$$g_{20}^{n+2}(Q^2) = -\frac{n+1}{n+2} g_{10}^{n+2}(Q^2), \quad (5.54)$$

with g_{10} given by Eq. (5.23). Thus, when including mass corrections in the analysis, the theoretically predicted structure function g_1 (or its n -th moment) as given by Eq. (5.23) is corrected by the first of Eqs. (5.52), together with the hypothesis (5.54) on the structure function g_2 at zero mass.

Chapter 6

Global analysis of inclusive DIS data

The problem of extracting relevant physical quantities from the existing inclusive DIS data is considered here in detail. The analysis is mainly aimed at assessing the relevance of inclusive measurements to the determination of the spin-dependent gluon density, its first moment and the x -shape.

To begin with, some details on the analysis method are given in Sec. 6.1, and the boundary conditions for parton distribution functions are discussed in Sec. 6.2. Sec. 6.3 is devoted to the study of the impact of the most recent inclusive DIS data on the extraction of polarized pdfs. In particular, the effect of very low-energy data is studied in Sec. 6.4, in connection with higher-twist corrections.

The results on the gluon distribution function are given in Sec. 6.5., and their dependence upon input densities extensively investigated. Finally, the main consequences of the above analysis on the structure function g_1 and moments of quark and gluon polarizations are summarized in Sec. 6.6.

6.1 Analysis method

The nucleon structure function g_1 is constructed at the measured points in the (x, Q^2) plane by convoluting the hard coefficient functions with the solutions of the NLO evolution equations. A parametrization for the polarized

pdfs in the singlet, nonsinglet and gluon sectors defined in Sec. 5, namely $\Delta\Sigma$, Δq_{NS} and Δg , as a function of a number of parameters is thus assigned at a given initial scale Q_0^2 . The whole set of parameters is then optimized by minimizing ¹ the total χ^2 , namely

$$\chi^2 = \sum_i \left(\frac{g_1(x, Q^2) - g_1^{\text{data}}(x, Q^2)}{\delta g_1^{\text{data}}(x, Q^2)} \right)^2, \quad (6.1)$$

where the sum runs over the available data points. Experimental data for g_1 are derived from the measured longitudinal spin asymmetry as discussed in Sec. 5.4, and are usually given along curves $Q^2(x)$ in a restricted region of the final-state invariant mass for each experimental set of data. The uncertainty δg_1^{data} includes both statistical and systematic errors added in quadrature, and $g_1(x, Q^2)$ denotes the theoretically predicted observable.

A full next-to-leading order analysis of the available experimental data on the polarized structure function g_1 of the nucleon has been performed in the Adler-Bardeen factorization scheme, as discussed in Sec. 5.3.

The AP evolution is performed in the Mellin space of the n -th moments, and, by the inverse transformation, the structure function g_1 in terms of the Bjorken- x is finally recovered for the fitting procedure, i.e. the χ^2 -minimization.

In order to extract g_1 data from the experimental asymmetries, as discussed in Sec. 5.4, one needs a parametrization for both the ratio $R = \sigma_L/\sigma_T$ of the photoabsorption cross sections, and the unpolarized structure function F_2 . Because of the slightly better coverage of the small- x region, due to the COMPASS data (see Sec. 6.3 below), the parametrization R1990 [47] used in previous analyses [12, 39] for the ratio $R = \sigma_L/\sigma_T$ has been replaced by the most recent one R1998 [48]. The latter parametrization indeed extends the kinematic range to lower and higher values of x ($0.005 \lesssim x \lesssim 0.86$), by adding to the fit a considerable number of data [49] on $R(x, Q^2)$.

Furthermore, the commonly used parametrization of the unpolarized structure function F_2 , which also enters into the experimental determination of g_1 , given by NMC [50] has been replaced by the unbiased one [51], obtained by training sets of neural networks on the experimental data (see [52]).

However, no sizable effects are observed as a result of both these implemen-

¹The χ^2 minimization procedure is performed by the CERN program library MINUIT [25].

tations, that is, all the parameters of pdfs turned out to be always largely consistent within the errors, and the quality of the fit essentially unchanged.

Finally, it should be noted that target mass corrections have been included as a rule up to the first order in m^2/Q^2 , as explained in Sec. 5.5, throughout this analysis. Indeed, when considering the finite size of the nucleon mass m , also the structure function g_2 enters into the theoretical determination of g_1 . Then, due to the lack of precise experimental data on g_2 , the Wandzura-Wilczek hypothesis has been invoked in the calculations (see Sec. 5.5).

6.2 Parametrization of pdfs

The functional form of spin-dependent parton distribution functions at the initial scale Q_0^2 is fixed according to the conventional parametrization

$$\Delta f(x, Q_0^2) = N_f \eta_f x^{\alpha_f} (1-x)^{\beta_f} (1 + \gamma_f x^{\delta_f}) \quad (\text{type-A}) \quad (6.2)$$

where Δf denotes $\Delta\Sigma$, Δq_{NS} , and Δg . The overall factor N_f is defined by the normalization condition

$$\int_0^1 dx \Delta f(x, Q_0^2) = \eta_f, \quad (6.3)$$

i.e. such that the parameters η_f , fitted to the data, directly reflect the value of the first moment of pdfs at the initial scale, which is taken as a rule at $Q_0^2 = 1 \text{ GeV}^2$.

The nonsinglet quark density at $Q_0^2 = 1 \text{ GeV}^2$ is defined by the linear combination of the triplet and octet distributions

$$\Delta q_{\text{NS}}(x, Q_0^2) = \pm \frac{3}{4} \Delta q_3(x, Q_0^2) + \frac{1}{4} \Delta q_8(x, Q_0^2), \quad (6.4)$$

where the plus (minus) sign stays for a proton (neutron) target. The distributions Δq_3 and Δq_8 are assumed to have the same x -dependence, while the parameter η_8 , corresponding to the first moment of Δq_8 , is fixed to the value $\eta_8 = 0.588 \pm 0.025$ by using SU(3) symmetry and octet baryon decay constants [8]. The parameter η_3 is instead fitted to the data. At higher scales, new contributions are generated dynamically as heavy quark thresholds are crossed.

Since the large- x behavior of the polarized gluon distribution can not be determined by inclusive DIS data, i.e. by scaling violations, the value of β_g needs to be fixed a priori. Typical values of β_g examined in the following analysis are restricted to the range $4 \leq \beta_g \leq 10$, and a correlation with the gluon first moment at the initial scale η_g is observed, in that increasing the (fixed) value of β_g leads to a slight decrease of η_g . Then, both parameters have been followed out as new data are included and the whole fit improved. Moreover, all the exponents δ_f in the last factor of Eq. (6.2) have been fixed, as in Ref. [12], respectively to the values ²

$$\delta_\Sigma = \delta_g = 1 \quad \text{and} \quad \delta_{\text{NS}} = 0.75. \quad (6.5)$$

A different functional form has been also adopted for the initial parametrizations, to evaluate the impact of the input densities on the final results. Specifically, while keeping the initial scale at $Q_0^2 = 1 \text{ GeV}^2$, the less singular input

$$\begin{aligned} \Delta\Sigma &= N_\Sigma \eta_\Sigma x^{\alpha_\Sigma} (\ln 1/x)^{\beta_\Sigma} && \text{(type-B)} && (6.6) \\ \Delta f &= N_f \eta_f \left[(\ln 1/x)^{\alpha_f} + \gamma_f x^{\delta_f} (\ln 1/x)^{\beta_f} \right] && \Delta f = \Delta q_{\text{NS}}, \Delta g \end{aligned}$$

is used for an alternative fit, with the same normalization condition (6.3). Similarly to the standard parametrization, the exponents δ_f are fixed to the values $\delta_g = 1$ and $\delta_{\text{NS}} = 0.75$. At variance with the initial densities (6.2), in Eq. (6.6) the rise at small x is at most logarithmic, and then softer than any power. Since $\ln 1/x \sim (1-x)$ as $x \rightarrow 1$, the large- x behavior in Eq. (6.6) is similar to Eq. (6.2) for the singlet distribution, whereas both terms contribute in the gluon and nonsinglet cases.

The total number of parameters determined from the fit amounts, in both cases, to at most eleven, and no limits are imposed on their variation. Also the sign of all parameters are left free, including the first moment at the initial scale, although the data always choose η_f to be positive.

Finally note that, in order to avoid any bias produced by further constraints, the input densities Eqs. (6.2) and (6.6) are not explicitly forced by the positivity condition $|\Delta f(x, Q^2)| \leq f(x, Q^2)$, at variance with many recent analyses

²The choice for δ_{NS} in particular is discussed in [26], and is made in order to avoid asymptotic behaviors in the nonsinglet channel more singular than $x^{-0.5}$ as $x \rightarrow 0$, corresponding to the maximum saturation of the partonic constraint $|\Delta q_{\text{NS}}(x, Q^2)| \lesssim q_{\text{NS}}(x, Q^2)$. Indeed, a correlation between the parameters δ_{NS} and α_{NS} has been pointed out in [26], such that α_{NS} approaches zero as δ_{NS} decreases from unity.

(see e.g. [27, 28]), where, on the other hand, the initial parametrizations for the polarized gluon, valence and sea quark distributions are taken proportional to the related unpolarized quantities, with proportionality factors given by powers of x . However, the positivity bound has been checked a posteriori, and, in the case of fits of type-A, turns out to be always largely fulfilled (see also [29]).

6.3 Update

The main purpose of the following analysis is to investigate the impact of the recent experimental data on the polarized parton distributions, with a special focus on the gluon polarization. The whole analysis is performed at NLO in the Adler-Bardeen factorization scheme, and the normalization of the strong coupling $\alpha_s(M_Z^2) = 0.118$ is assumed throughout.

The starting point is a global fit of type-A (Eq. (6.2)), of inclusive DIS data, on the basis of 176 experimental points used in the previous analyses [12, 39], as summarized in Tab. 1.

Data set (target)	x -range	Q^2 -range (GeV ²)	No. data	Ref.
SMC (p)	0.005 - 0.479	1.3 - 58	12	[30]
E143 (p,d)	0.031 - 0.749	1.27 - 9.52	56	[31]
E155 (p)	0.015 - 0.75	1.22 - 34.72	24	[32]
HERMES (p)	0.023 - 0.66	1.01 - 7.36	20	[33]
SMC (d)	0.005 - 0.480	1.3 - 54.8	12	[30]
E155 (d)	0.015 - 0.75	1.22 - 34.79	24	[34]
E142 (n)	0.035 - 0.466	1.1 - 5.5	8	[35]
HERMES (n)	0.033 - 0.464	1.22 - 5.25	9	[36]
E154 (n)	0.014 - 0.564	1.2 - 15	11	[37]

Tab. 1 Initial set of inclusive DIS data (176 experimental points).

Note that the effects of the E155 proton data [32] alone have been analyzed in recent works [38], and the conclusion was reached that their accuracy significantly contributes to reducing the statistical errors of pdfs.

As can be seen by the scatter plot in Fig. 6.1, the covered region of the (x, Q^2) -plane is roughly restricted to $0.01 \lesssim x \lesssim 0.8$ for the Bjorken x (with the exception of very few SMC points at lower x), and to $1 \leq Q^2 \lesssim 58 \text{ GeV}^2$ for the momentum transfer. Indeed the cut $Q^2 \geq 1 \text{ GeV}^2$ is imposed as a rule to all the data.

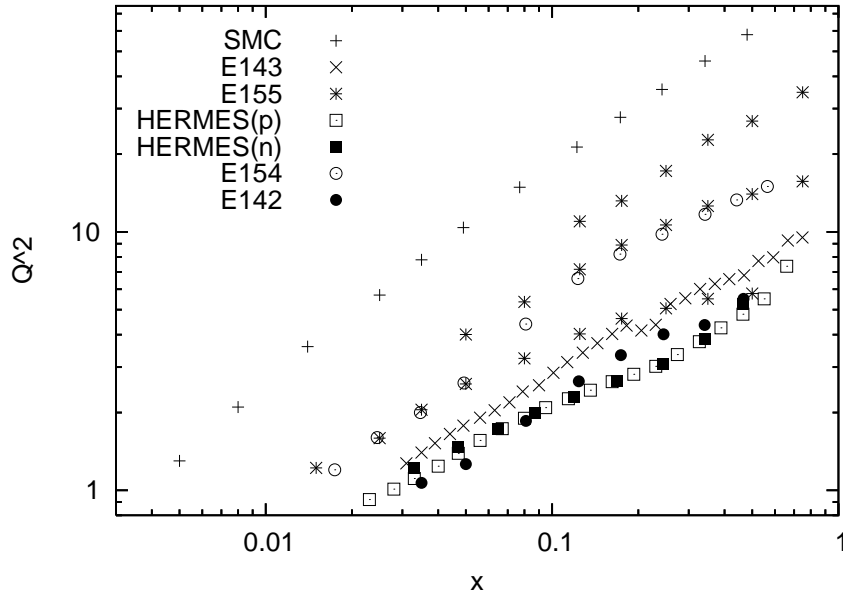


Figure 6.1: Distribution in the (x, Q^2) -plane of the set of 176 DIS data up to 2000, as summarized in Tab. 1.

The results of a fit of type-A on this set of data are shown in the second column of Tab. 3. By comparing such results with those of the previous analyses [12, 39], globally the same picture arises, and, in particular, the x -shapes of pdfs are similar to those of Refs. [12, 39], and likewise not very precisely determined.

A sizable first moment of the polarized gluon density at the initial scale is found, and, both the gluon and the nonsinglet quark distributions rise as $x \rightarrow 0$, whereas a flat behavior is observed in the singlet sector.

Note that the parameters γ_g and γ_Σ , which control the shape of the gluon and singlet distributions at intermediate x , can not be disentangled in this

analysis. As observed in [20], this is due to the mixing of Δg and $\Delta\Sigma$ in the AP evolution. Therefore $\gamma_g = \gamma_\Sigma$ is taken, thus leaving ten parameters to be determined by the χ^2 minimization. Finally, the errors given here are statistical errors from the fit.

A bulk of more precise data has become recently available. These are in particular 15 points at rather high energy from COMPASS³, and a number of lower energy points from HERMES and JLAB as summarized in Tab. 2. Furthermore, a set of complementary data from SMC has been also included, that was not considered in the previous analyses [12, 39]. A large amount of very low-energy data from CLAS [45, 46] will be considered separately, in connection with higher-twist effects (see Sec. 6.3).

Data set (target)	x -range	Q^2 -range (GeV ²)	No. data	Ref.
COMPASS (d)	0.0046 - 0.566	1.10 - 55.3	15	[41]
HERMES (p,d)	0.0264 - 0.7311	1.12 - 14.29	74	[42]
JLAB	0.33 - 0.60	2.71 - 4.83	3	[43]
SMC (p,d)	0.0043 - 0.121	1.09 - 23.1	16	[44]

Tab. 2. New set of inclusive DIS data up to 2006.

As shown in Figs. 6.2 and 6.3, such data slightly improve the coverage of the (x, Q^2) -plane, and in particular the low- x region down to $x \gtrsim 0.0046$ (COMPASS).

The results of a fit of type-A, including all these most recent data is displayed in the third column of Tab. 3. Due to the increased number of experimental points and their accuracy, an overall reduction of the statistical errors from the fit is observed. Aside from a somewhat flatter behavior at small- x of the polarized singlet distribution, essentially the same shape of pdfs turns out in both the singlet and nonsinglet sectors, which are displayed at the initial scale in Fig. 6.4. In particular, the new small- x data points confirm the rise of the nonsinglet distribution Δq_{NS} , already determined in the previous analyses [12, 26]. The singlet and nonsinglet first moments are fairly unaffected by the new experimental data.

³Note that the latest COMPASS data [40] at very low x and Q^2 have been excluded altogether in this analysis, all lying below the cut $Q^2 \geq 1 \text{ GeV}^2$ imposed to the data set.

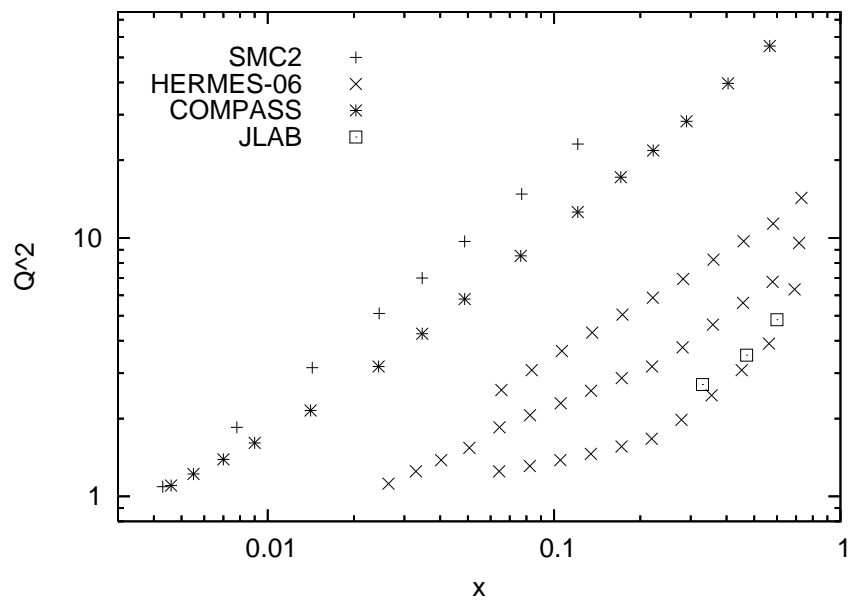


Figure 6.2: Distribution in the (x, Q^2) -plane of the new set of DIS data up to 2006, as summarized in Tab. 2.

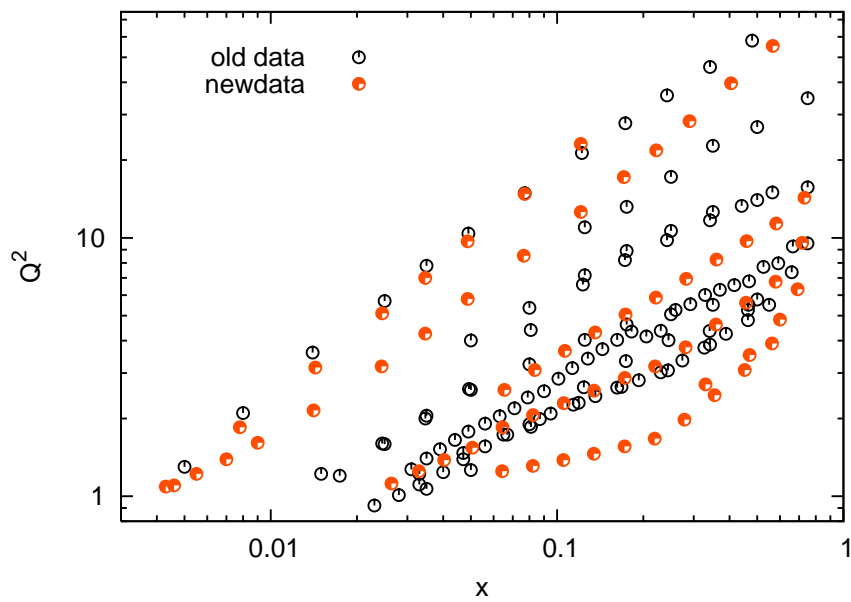


Figure 6.3: Distribution in the (x, Q^2) -plane of the complete set of data.

Parameters ($Q_0^2 = 1 \text{ GeV}^2$)	176 data	284 data
η_Σ	0.347 ± 0.025	0.344 ± 0.011
α_Σ	0.732 ± 0.504	1.421 ± 0.167
β_Σ	4.307 ± 0.626	3.212 ± 0.918
γ_Σ	10.044 ± 16.356	-0.673 ± 0.805
η_g	0.856 ± 0.666	0.402 ± 0.062
α_g	-0.772 ± 0.443	-0.300 ± 0.194
β_g	4. (fixed)	10. (fixed)
γ_g	10.044 ± 16.356	-0.673 ± 0.805
η_3	1.119 ± 0.035	1.095 ± 0.024
α_{NS}	-0.364 ± 0.307	-0.276 ± 0.165
β_{NS}	2.982 ± 0.291	3.186 ± 0.157
γ_{NS}	9.749 ± 15.426	7.356 ± 6.271
$\chi^2/\text{d.o.f}$	0.936	0.879
$a_0(10 \text{ GeV}^2)$	0.142 ± 0.023	0.234 ± 0.010
$\Gamma_1^p(10 \text{ GeV}^2)$	0.113 ± 0.002	0.121 ± 0.001

Tab. 3. Fits of type-A, respectively to the set of 176 data points of Tab. 1 (second column) and to the full set including data of Tab. 2 (third column).

The most relevant feature here is the sizable reduction of the gluon first moment and of its statistical error. Actually, such a low value of η_g is also correlated to the large fixed value of β_g , that seems, however, the value preferred by the data. Indeed, the same fit has been repeated by exploring lower (fixed) values of β_g , and the minimum χ^2 is found, for this set of data, with $\beta_g = 10$. The correlation between the parameter that controls the large- x shape of Δg and the first moment turns out to be a distinctive feature of the type-A parametrization, and is not observed in the case of the type-B fit (see Sec. 6.5.2). A deeper discussion of the impact of each set of experimental points on η_g is given in Sec. 6.5.1.

The resulting polarized gluon density (type-A) is displayed in Fig. 6.5 with increasing scale Q^2 (red lines), and compared with the analogous result of the reference fit to 176 data points (black lines).

Finally, the value of the singlet axial charge $a_0(Q^2)$ is considerably increased, and is given in Tab. 3 at $Q^2 = 10 \text{ GeV}^2$ for both fits. Also shown in Tab. 3, as an example, is the first moment of the polarized structure function g_1

for a proton target at the same scale and computed over the full x -range. Complete results for g_1 are summarized in Sec. 6.6.1.

6.4 Low-energy data

A large amount of low-energy and very precise data points from the CLAS collaboration [45, 46], both on proton and deuteron targets, has been left aside in the previous analysis in order to disentangle the effects of high and low energy data on polarized pdfs. Indeed, CLAS data are restricted to a limited region of the final-state hadronic invariant mass, roughly $1 \text{ GeV} \lesssim W \lesssim 3 \text{ GeV}$, where non-perturbative effects could be relevant. This kinematical region involves large Bjorken- x at moderate values of the squared momentum transfer Q^2 , and is characterized by the presence of nucleon resonances which contribute to higher-twist effects in the structure functions.

In order to perform a consistent perturbative analysis of world data, a quantitative criterion for selecting experimental points from CLAS has been studied. To this end, a lower bound on the invariant mass W has been preliminarily estimated on the basis of the relevance of higher-twist contributions to the moments of the polarized structure function g_1 .

As a next step, the precise location of the kinematic cut to be imposed on the whole set of data has been determined by explicitly evaluating residual higher-twist effects.

6.4.1 Selection of CLAS data

In order to fix a lower cut on the (x, Q^2) plane to the full set of CLAS data, a recent analysis [53] of the higher moments of the proton structure function g_1^p has been exploited. All the available data, both in the DIS and resonance region [45], down to very low Q^2 , are used in [53] to estimate the higher-twist contributions (twist-4 and 6) to the n -th moments of g_1^p

$$M_n(Q^2) = \delta\eta_n(Q^2) + HT_n(Q^2). \quad (6.7)$$

with $n = 3, 5, 7$. Here the leading and higher-twist terms, $\delta\eta_n(Q^2)$ and $HT_n(Q^2)$ respectively (see Eqs. (32) and (45) in Ref. [53]), have been determined by fitting a number of parameters to the data. As expected, the total

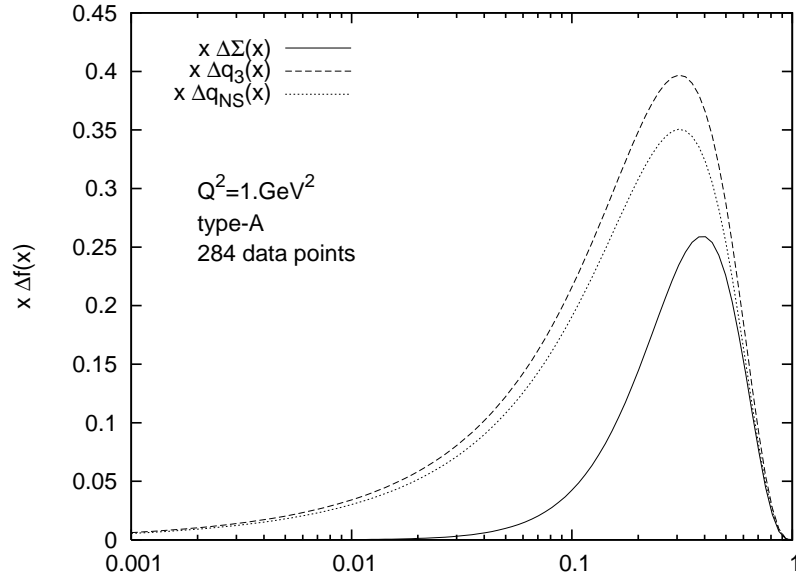


Figure 6.4: Singlet and nonsinglet distributions^x (proton target) at $Q^2 = 1 \text{ GeV}^2$ from a fit of type-A on the whole set of available data.

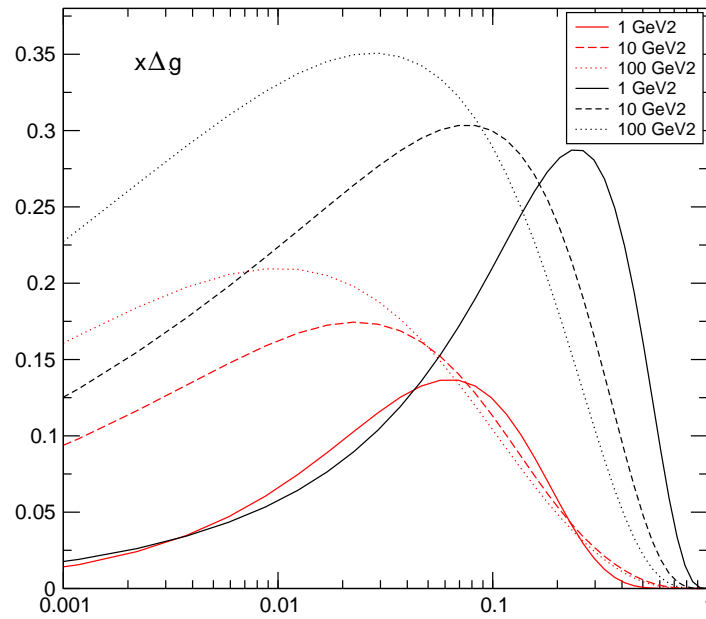


Figure 6.5: Best-fit forms (type-A) of $x\Delta g(x)$ in both fits, respectively to the set of 176 data points (black curves) and to the full set including data of Tab. 2 (red curves), with increasing Q^2 .

higher-twist term turned out [53] to be sizable mainly for $Q^2 \sim \text{few GeV}^2$ and is still non-negligible even at $Q^2 \simeq 10 \text{ GeV}^2$ for the higher moments. Moreover, it has been pointed out in [53] that the total higher-twist contribution is significantly larger in the polarized case than in the unpolarized one (see also [54]).

On the basis of the above analysis, the ratio $HT_n(Q^2)/\delta\eta_n(Q^2)$ can be easily evaluated for each n on a wide range of Q^2 . This fact has been used here to select a lower bound on the momentum transfer, Q_0^2 , for each n , by requiring $HT_n(Q^2)/\delta\eta_n(Q^2) \lesssim 10\%$ for $Q^2 \gtrsim Q_0^2$.

Then, in order to define a proper cut to CLAS data in the (x, Q^2) -plane, to each n a corresponding value of x must be also assigned. To this end, the integrand $x^{n-1} g_1^p(x, Q_0^2)$ of the n -th moment of the proton structure function g_1^p has been evaluated at the quoted Q_0^2 , and the position of the peak, x_0 , has been taken as a characteristic value of x .

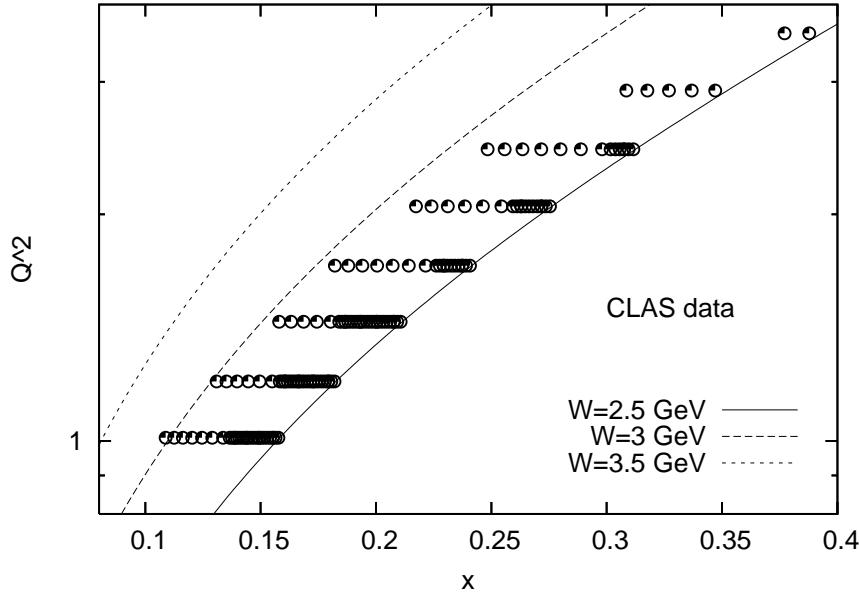


Figure 6.6: Set of CLAS data cut at $W \geq 2.5 \text{ GeV}$ used in the present analysis.

By combining these values of x_0 and Q_0^2 for each $n = 3, 5, 7$, the corresponding invariant mass W_0 has been computed according to Eq. (5.3). It has been found $W_0 = 1.93, 2.48, 2.96 \text{ GeV}$ for the moments $n = 3, 5, 7$, respectively.

Then, taking an average over the three values of W_0 , one roughly finds $W_0 \simeq 2.5$ GeV as a lower bound on the final-state invariant mass. One may thus conclude that data points below this threshold can not be safely included in the analysis without taking into account higher-twist corrections, whose contribution amounts to at least 10% of the leading twist term in this region of the (x, Q^2) -plane.

As a first result, this leads to a preliminary selection on the full set of CLAS data. Indeed, only 148 experimental points lying above the cut $W_0 = 2.5$ GeV are retained in what follows, and their distribution in the (x, Q^2) -plane is displayed in Fig. 6.6.

6.4.2 Higher-twist effects

As a result of the above analysis, a lower bound should be consistently imposed on the whole set of available data. Indeed, all the data below $W_0 = 2.5$ GeV must be certainly discarded, and the precise position of the global cut has been investigated by studying the related effects of residual higher twist corrections on the results.

Three possible cuts are compared in Fig. 6.7 with the whole set of data, including the selected CLAS data (cut at $W \geq 2.5$ GeV). As can be seen, a cut at $W \geq 3$ GeV would entail the exclusion of all the experimental points from CLAS (with the exception of only one point on proton target), and of a number of new HERMES data as well. Higher cuts would mean a sizeable loss of information, whereas imposing the lower bound at $W = 2.5$ GeV does not significantly reduce the set of data but higher twist effects could still play a relevant role in this region.

This issue has been quantitatively evaluated by introducing a phenomenological term for the structure function g_1 , so as to take into account higher-twist contributions in the Bjorken- x space, namely

$$g_1(x, Q^2) \rightarrow g_1(x, Q^2) \left[1 + \frac{c}{W^2} \right]. \quad (6.8)$$

The multiplicative factor in Eq. (6.8) depends on one dimensional parameter c to be fitted to the data, in order to study the role of lower energy points in the determination of higher-twist corrections. A broad range of possible cuts W_0 has been investigated; specifically, the same fit of type-A, with one more fitting parameter c , has been performed on the whole set of data (including

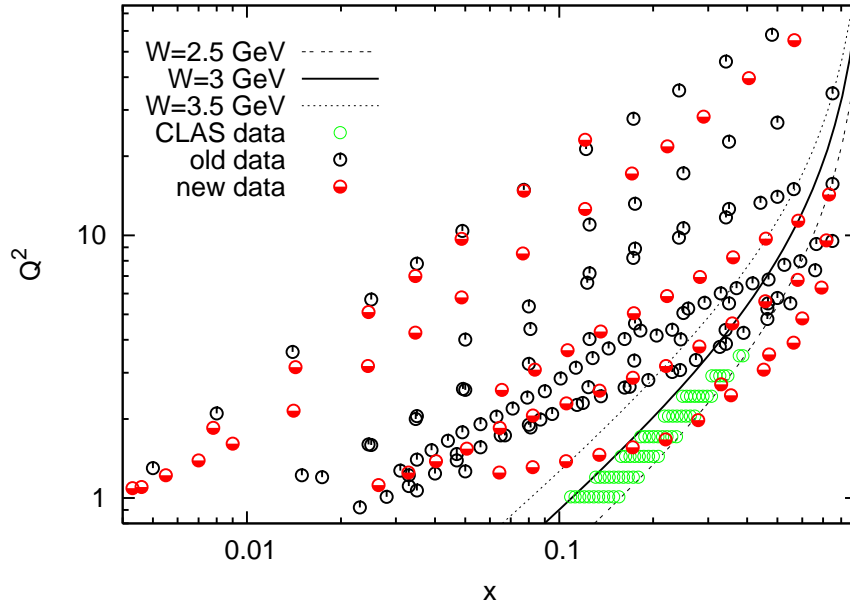


Figure 6.7: Distribution in the (x, Q^2) -plane of the whole set of data including selected CLAS data, compared with lines of fixed final-state invariant mass $W = 2.5, 3$ and 3.5 GeV.

the selected subset of CLAS data), progressively cut at higher values W of the invariant mass.

The values of the HT parameter c with their errors, as determined by these fits, are displayed in Fig. 6.8 as a function of the cut W_0 imposed. As a result, the higher-twist contributions turn out to be gradually less relevant as the full set of data is restricted to higher values of W . Indeed, as can be seen by Fig. 6.8, the largeness of the error bar increases with the value of the cut W_0 , making the higher-twist parameter more consistent with zero.

A glance to Figs. 6.7 and 6.8 reveals that the choice $W_0 = 3$ GeV, where the higher-twist parameter c differs from zero by no more than 1.5 standard deviations, seems a reasonable one, in that it justifies a purely perturbative analysis while reducing the loss of experimental information.

In Tab. 4 are shown, as an example, the results of two fits of type-A with 11 fitted parameters and different cuts on W , i.e., no cut at all (except for CLAS data cut at $W \gtrsim 2.5$ GeV) and $W \gtrsim 3.5$ GeV over all the available points (which excludes CLAS data altogether).

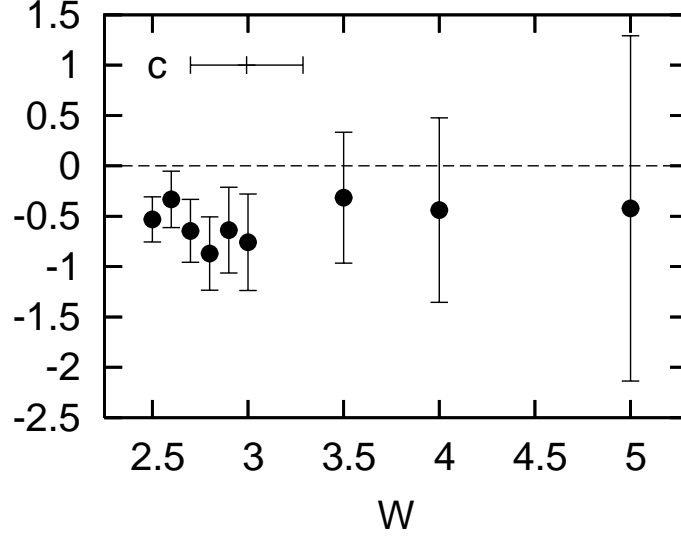


Figure 6.8: Values with errors of the parameter c fitted to the set of data gradually cut at higher W .

Parameters ($Q_0^2 = 1 \text{ GeV}^2$)	no cut	$W \geq 3.5 \text{ GeV}$
η_Σ	0.401 ± 0.014	0.397 ± 0.021
α_Σ	1.357 ± 0.273	1.347 ± 0.304
β_Σ	2.655 ± 1.233	2.435 ± 1.198
γ_Σ	-1.015 ± 0.448	-1.191 ± 0.320
η_g	0.444 ± 0.066	0.494 ± 0.075
α_g	-0.388 ± 0.184	-0.451 ± 0.179
β_g	8. (fixed)	6. (fixed)
γ_g	-1.015 ± 0.448	-1.191 ± 0.320
η_3	1.129 ± 0.027	1.137 ± 0.041
α_{NS}	-0.236 ± 0.158	-0.327 ± 0.218
β_{NS}	3.119 ± 0.163	2.903 ± 0.300
γ_{NS}	7.114 ± 5.630	8.979 ± 10.051
c	-0.561 ± 0.210	-0.315 ± 0.650
$\chi^2/\text{d.o.f}$	0.937	1.056

Tab. 4. Fits of type-A, respectively to the full set of data with no cut except for CLAS ($W \geq 2.5 \text{ GeV}$) (second column), and with a global cut at $W \geq 3.5 \text{ GeV}$ (third column).

Comparing the second column of Tab. 4 with the third one of Tab. 3 it can be seen that CLAS data do not sizably affect the shape of quark and gluon densities, whereas the main effects of the lower energy points, all cut in the third column of Tab. 4, is essentially the improvement in the determination of higher-twist contributions to g_1 . Similar conclusions were also reached in Ref. [55] where the impact of a much extended subset of CLAS data [46] (i.e. $W \gtrsim 2$ GeV) on polarized pdfs has been studied.

6.5 Gluon polarization from g_1 data

As discussed in the previous section, in order to perform a consistent perturbative treatment of world data, avoiding systematic errors induced by higher-twist effects, the final set of experimental points retained is the one selected by the cut on the invariant mass at $W \geq 3$ GeV, which amounts to 238 data points and covers the region above the solid curve in Fig. 6.7. Indeed, in this kinematical region the higher-twist contributions can be safely neglected.

The corresponding experimental asymmetries on proton, neutron and deuteron targets included in the analysis are given as a function of x in Figs. 6.9, 6.10 and 6.11 respectively.

As already noted, all the CLAS data (except for one point) have been excluded, together with the three points from JLAB and also a number of lower energy HERMES data. Such a cut has obviously no effect on the higher energy data from COMPASS and SMC.

The information that can be extracted specifically on the polarized gluon density by a global fit of the present inclusive DIS data are discussed in the following sections.

6.5.1 Best-fit results and impact of the data on the gluon first moment

The results of a type-A fit to this set of experimental points is shown in Tab. 5. Here, higher-twist corrections are switched off ($c = 0$ fixed), whereas target mass corrections are included as a rule. As a cross check, it has been verified that no sizable differences can be traced with respect to the results

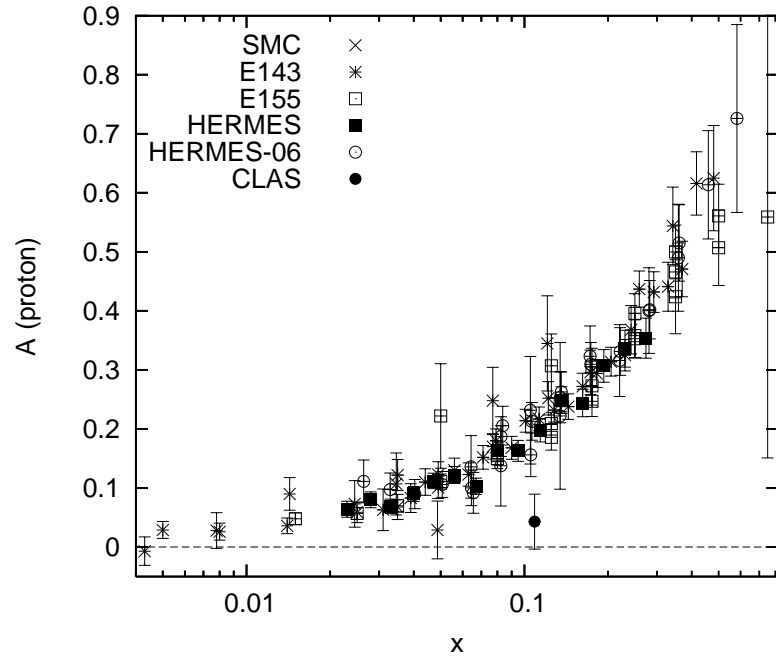


Figure 6.9: Asymmetry data on proton target summarized in Tabs. 1 and 2, cut at $W \geq 3$ GeV.

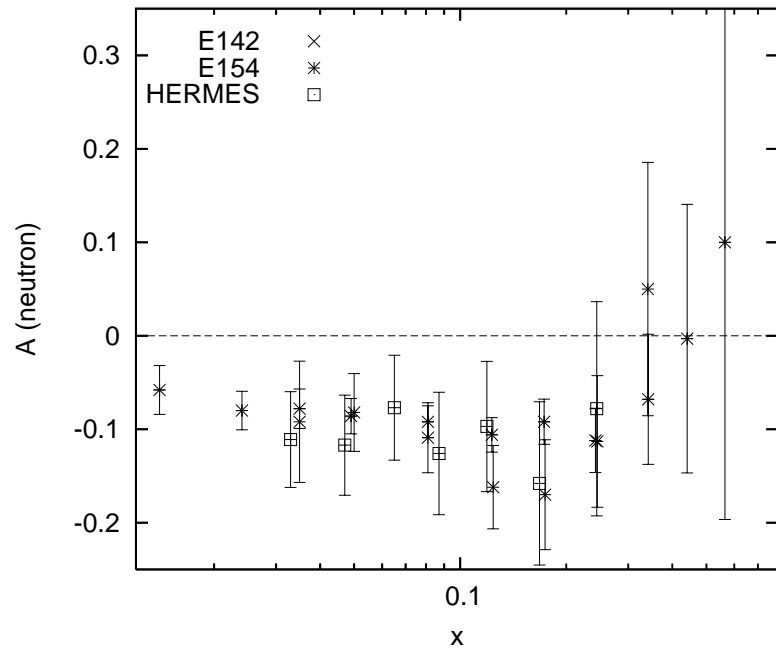


Figure 6.10: Asymmetry data on neutron target summarized in Tabs. 1 and 2, cut at $W \geq 3$ GeV.

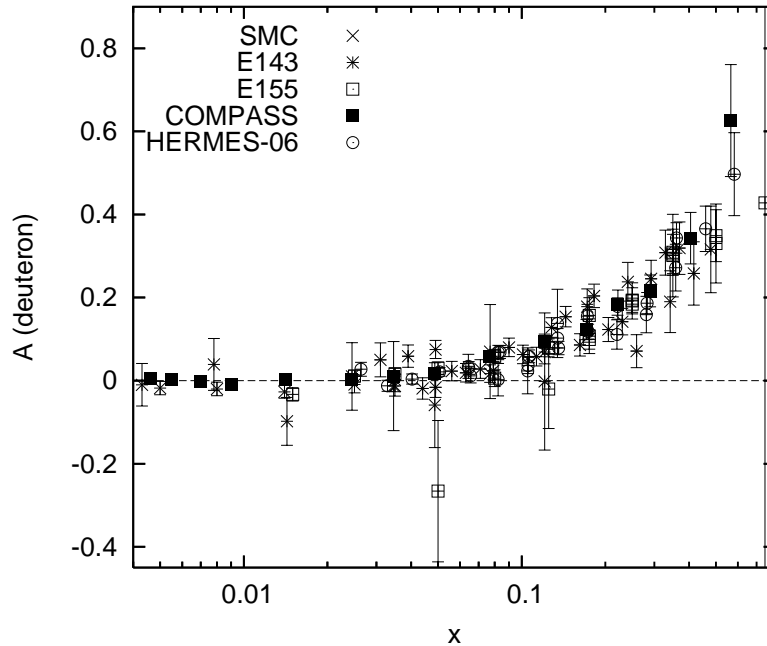


Figure 6.11: Asymmetry data on deuteron target summarized in Tabs. 1 and 2, cut at $W \geq 3$ GeV.

of a similar fit performed on the same set of data where the higher-twist parameter c has been fitted ($c = -0.76 \pm 0.48$).

Comparing the results of Tab. 5 with those of the third column of Tab. 3 (including the whole set of data except for CLAS) makes clear that the main effect of the cut on the quark and gluon polarizations amounts to an overall increase of the statistical errors due to the loss of a number of experimental points, mainly from HERMES. On the other hand, the systematic error due to higher-twist effects is reduced by excluding low-energy data.

The x -shapes of the quark singlet and nonsinglet distributions are very similar to those displayed in Figs. 6.4, and slightly differ only for the normalization. Specifically, the nonsinglet quark distribution rises at small- x , whereas the Adler-Bardeen singlet quark turns out to be flat at the initial scale. The best-fit form of quark distributions is displayed in Fig. 6.12 (black lines).

The first moment of the polarized gluon density (and its statistical error) at the initial scale is slightly increased, but is nevertheless much smaller than the previous determinations (see Tab. 3, second column), in agreement with

many current analyses (see Sec. 6.5).

The parameter γ_g in Tab. 5 has been disentangled from γ_Σ , but clearly the present data can not give precise constrains on its value. Again, the behavior of Δg as $x \rightarrow 1$ can not be determined by inclusive DIS measurements and the parameter β_g has to be fixed. The range $4 \leq \beta_g \leq 10$ has been explored and the minimum χ^2 is found for $\beta_g = 6$.

Parameters ($Q_0^2 = 1 \text{ GeV}^2$)	type-A ($W \geq 3 \text{ GeV}$, 238 data)
η_Σ	0.391 ± 0.021
α_Σ	1.154 ± 0.334
β_Σ	1.918 ± 0.972
γ_Σ	-1.232 ± 0.192
η_g	0.555 ± 0.146
α_g	-0.484 ± 0.293
β_g	6. (fixed)
γ_g	3.829 ± 10.443
η_3	1.127 ± 0.034
α_{NS}	-0.321 ± 0.271
β_{NS}	2.970 ± 0.336
γ_{NS}	9.475 ± 13.376
$\chi^2/\text{d.o.f}$	0.932
$a_0(10 \text{ GeV}^2)$	0.246 ± 0.025
$\Gamma_1^p(10 \text{ GeV}^2)$	0.125 ± 0.003

Tab. 5. Best-fit result of type-A on the selected data set, and $c = 0$ fixed.

data set	$\eta_g (Q_0^2 = 1 \text{ GeV}^2)$	β_g (fixed)	$\chi^2/\text{d.o.f}$.
176 set	0.86 ± 0.67	4.	0.94
+ SMC2	0.69 ± 0.52	6.	0.96
+ COMPASS	0.53 ± 0.14	8.	0.93
+ HERMES-06	0.43 ± 0.07	8.	0.88
+ JLAB	0.40 ± 0.06	10.	0.88
238 set ($W \geq 3 \text{ GeV}$)	0.56 ± 0.15	6.	0.93

Tab. 6. Impact of each set of experimental data on the value of the first moment η_g of the gluon distribution. Also shown are the corresponding value of β_g and the related χ^2 .

The x -shape of the best-fit result of type-A (black curves) for the polarized gluon distribution is displayed in Fig. 6.13 with increasing momentum transfer.

Finally, the impact of each set of data on the first moment of the gluon polarization is summarized in Tab. 6, together with the corresponding best value of β_g and the related χ^2 . As can be seen, all the measurements contribute to decreasing η_g , the much relevant effect being that from the high-energy data by COMPASS, lying well above the cut imposed on the (x, Q^2) -plane.

6.5.2 Dependence of Δg on input densities

The assumed functional form of input densities sizably affects the determination of relevant quantities, such as the x -shape of the gluon polarization. A way of evaluating this effect is to perform the whole analysis by changing the initial parametrization of pdfs. This has been done here by using the functional form given by Eq. (6.6) (type-B) for an alternative fit on the selected set of data cut at $W \geq 3 \text{ GeV}$ used in the type-A fit (Tab. 5).

Parameters ($Q_0^2 = 1 \text{ GeV}^2$)	type-B ($W \geq \text{GeV}$, 238 data)
η_Σ	0.417 ± 0.023
α_Σ	2.496 ± 0.425
β_Σ	3.512 ± 0.467
η_g	0.801 ± 0.190
α_g	1.050 ± 0.486
β_g	3.113 ± 0.868
γ_g	-1.447 ± 0.647
η_3	1.219 ± 0.038
α_{NS}	1.733 ± 0.121
β_{NS}	4.655 ± 0.138
γ_{NS}	-0.269 ± 0.060
$\chi^2/\text{d.o.f}$	0.926
$a_0(10 \text{ GeV}^2)$	0.218 ± 0.027
$\Gamma_1^p(10 \text{ GeV}^2)$	0.129 ± 0.004

Tab. 7. Best-fit result of type-B on the selected data set, and $c = 0$ fixed.

The analysis is performed in the Adler-Bardeen scheme, and the results for the pdf parameters, the singlet axial charge $a_0(Q^2)$ and the first moment $\Gamma_1^p(Q^2)$ of the proton structure function at $Q^2 = 10 \text{ GeV}^2$ are given in Tab. 7. These results may be compared with those of the related fit of type-A (Tab. 5).

In the quark sector first moments turns out to be compatible within the errors with those from the type-A fit. The resulting x -shapes of singlet and nonsinglet distributions are also very similar to the best-fit forms of type-A, and are displayed in Fig. 6.12 at the initial scale (red lines).

A stronger sensitivity to the initial functional form is observed in the gluon sector. The central value of the gluon first moment turns out to be larger than that of type-A, even though still compatible within the errors.

On the other hand, the x -shape of Δg is considerably changed with respect to type-A, and both are displayed in Fig. 6.13 with increasing momentum transfer Q^2 . Note that, at variance with the fits of type-A, the behavior of Δg as $x \rightarrow 1$ has not been fixed here a priori.

A quantitative estimate of the systematic uncertainty produced by the choice of input densities may be performed by analyzing distinctive features of the x -shape in both type-A and B gluon distributions, such as the position of the peak and the corresponding value of the function. This study has been performed in Sec 7, in connection with pseudo-data analyses for charm photo-production at the COMPASS experiment that aim at measuring Δg directly (see Sec. 7).

Finally, being the quality of the fit fairly the same in both cases, no one of the assumed functional forms is neatly preferred by the data, that is both choices of input densities give equally good fits of inclusive world data, although the gluon x -shapes are significantly different. This result makes clear the large bias produced by the initial parametrization on the spin-dependent gluon distribution. This fact, sometimes hidden within most of the available phenomenological studies, mainly performed by imposing standard input densities (and constrained by the positivity condition), has been here clearly stated and taken into account in the estimation of the theoretical errors (see Sec. 6.6.2 below, and also Sec. 7.3). One may thus conclude that, even though the better coverage of the (x, Q^2) -plane, mainly due to the precise COMPASS data, allows a more reliable determination of the first moment of the gluon polarization by scaling violations, its x -shape is still largely unconstrained by the present inclusive DIS data.

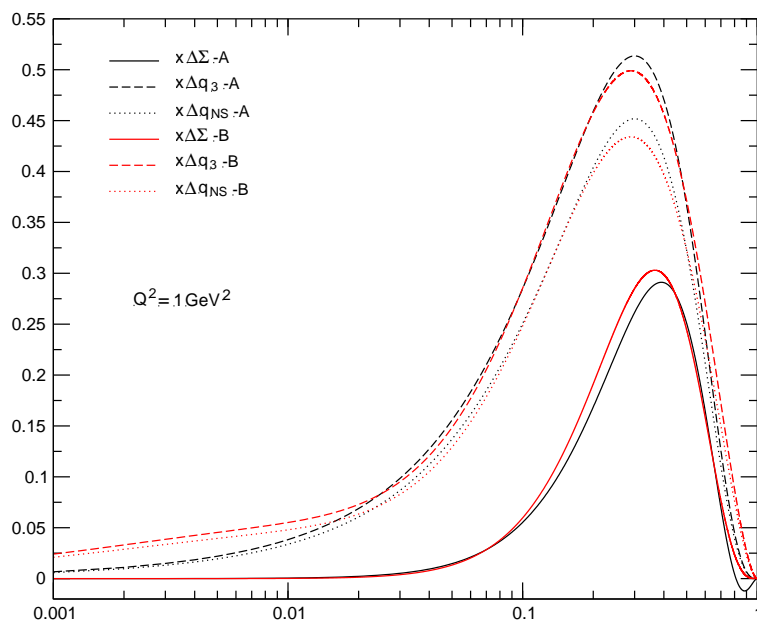


Figure 6.12: Best-fit results of type-A and B (black and red lines respectively) for the polarized quark singlet and nonsinglet distributions (proton target) at $Q^2 = 1 \text{ GeV}^2$, over the selected set of available data ($W \geq 3 \text{ GeV}$).

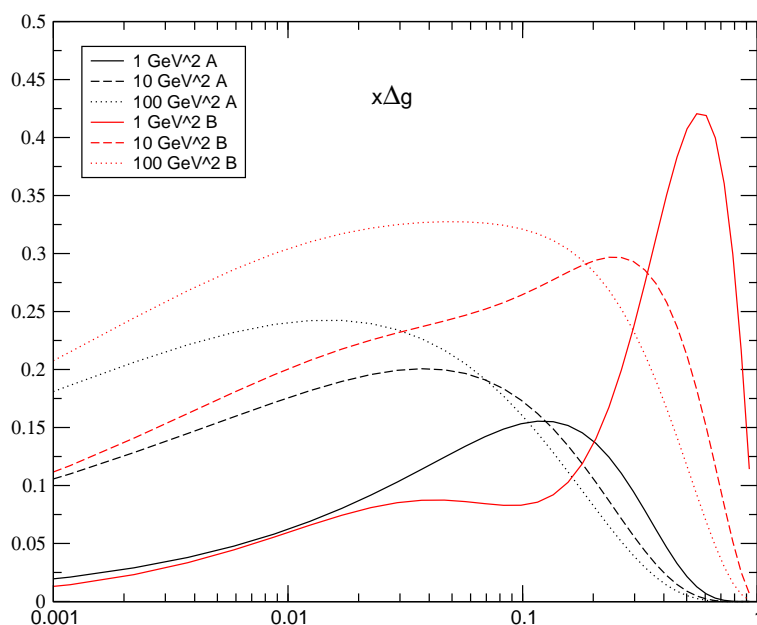


Figure 6.13: Best-fit results for the polarized gluon distribution with increasing Q^2 , over the selected set of available data ($W \geq 3 \text{ GeV}$). The black curves denote the fit of type-A, and the red ones the fit of type-B.

6.6 Phenomenological implications

The main results of the above analysis as far as physically relevant quantities are concerned are summarized in the following sections. Specifically, the best-fit forms of structure functions are presented, and the final estimate for the singlet axial charge and the polarization of the gluon and the quark flavor singlet combination in the nucleon are discussed.

6.6.1 Best-fit results for g_1

The best-fit structure functions g_1 (type-A) for proton, neutron and deuteron targets, are displayed in Figs. 6.14, 6.15 and 6.16 respectively, in the range of momentum transfer covered by the data (i.e. $Q^2 = 1, 10 \text{ GeV}^2$), and compared with the experimental points with their errors used in the analysis. Note that the sharp rise at large- x observed in all the three curves at the initial scale ($Q^2 = 1 \text{ GeV}^2$) is due to the inclusion of target mass corrections, and it disappears if $m^2 = 0$ is taken exactly for the nucleon mass. Such an effect, however, is not physical since the approximation adopted for the calculation of target mass corrections becomes unreliable at very large x (see [22]). Indeed, because of the m^2/Q^2 suppression factor, this unphysical peak is washed out at higher Q^2 , which is actually the experimentally interesting region for large- x .

Figs. 6.17, 6.18 and 6.19 compare the best-fit forms of g_1 for each target, corresponding to both fits, type-A and B respectively, at $Q^2 = 10 \text{ GeV}^2$. Sizable differences can be traced in the small- x region in the two fits. This fact is due to the way the functional forms of pdfs extrapolate the behavior observed in the last measured points, emphasizing the impact of the initial parametrization on the small- x behavior of the structure functions. In all cases g_1 is driven negative at small- x by the rise of the polarized gluon density in this region.

The values of the first moment of g_1 obtained by integration over both the full x -range and only over the measured range, are given in Tab. 8, at typical values of Q^2 for each target. Both fits, type-A and B respectively, are considered. The truncated moments turn out to be generally quite close to each other.

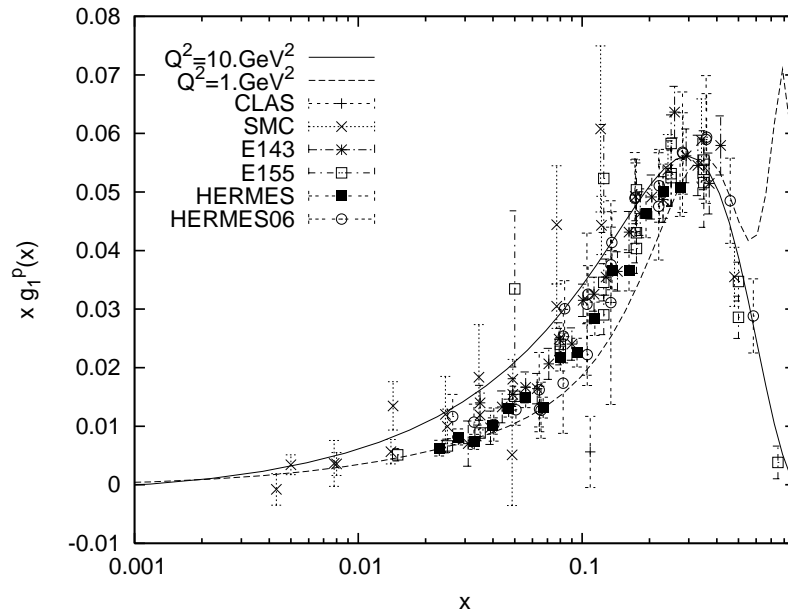


Figure 6.14: Best-fit result (type-A) for the proton structure function compared with the data points used in the analysis ($W \geq 3 \text{ GeV}$).

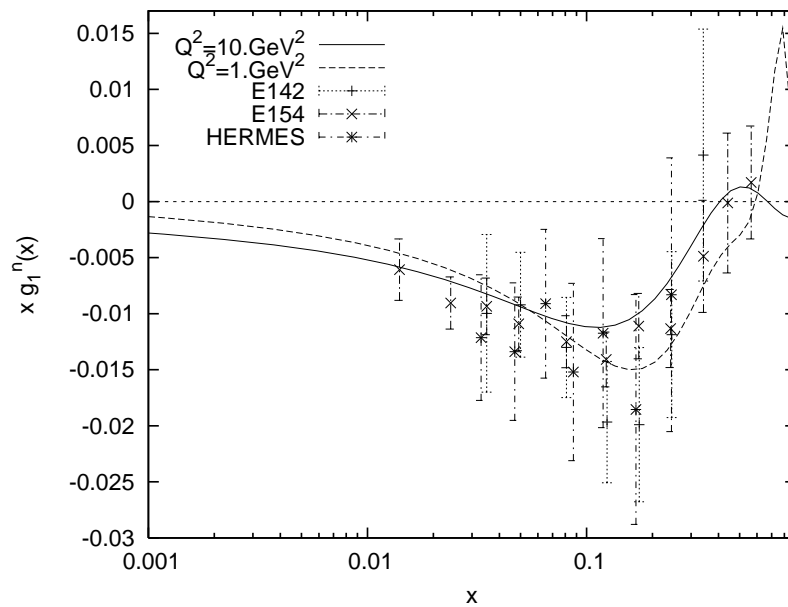


Figure 6.15: Best-fit result (type-A) for the neutron structure function compared with the data points used in the analysis ($W \geq 3 \text{ GeV}$).

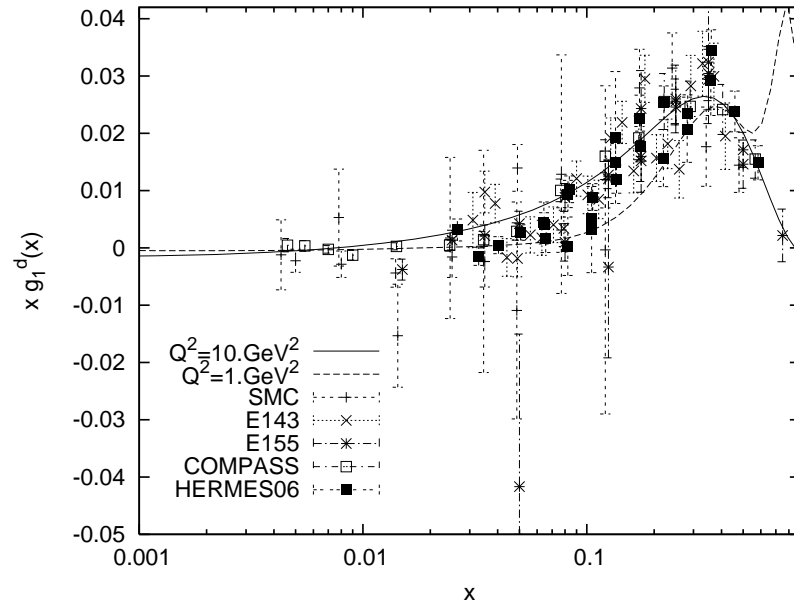


Figure 6.16: Best-fit result (type-A) for the deuteron structure function compared with the data points used in the analysis ($W \geq 3 \text{ GeV}$).

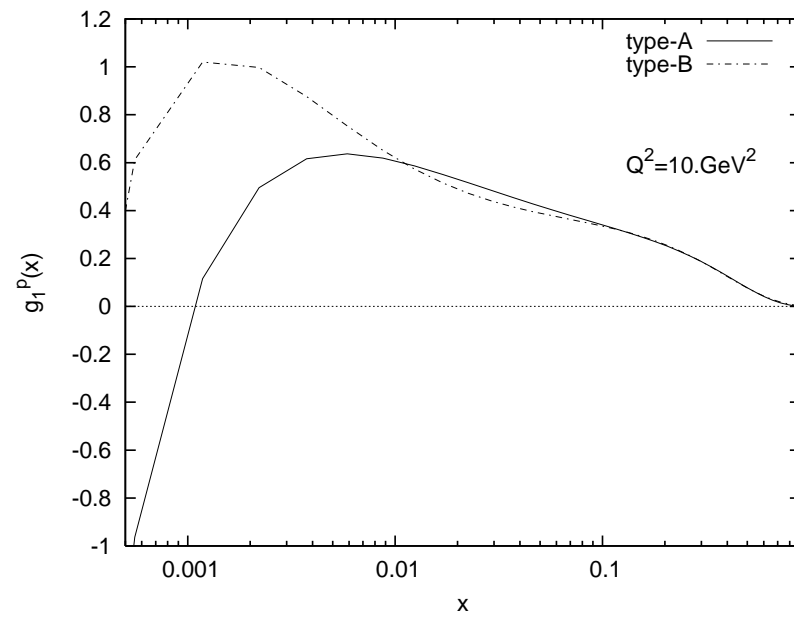


Figure 6.17: Best-fit results of type-A (solid) and type-B (dot-dashed) for the proton structure function.

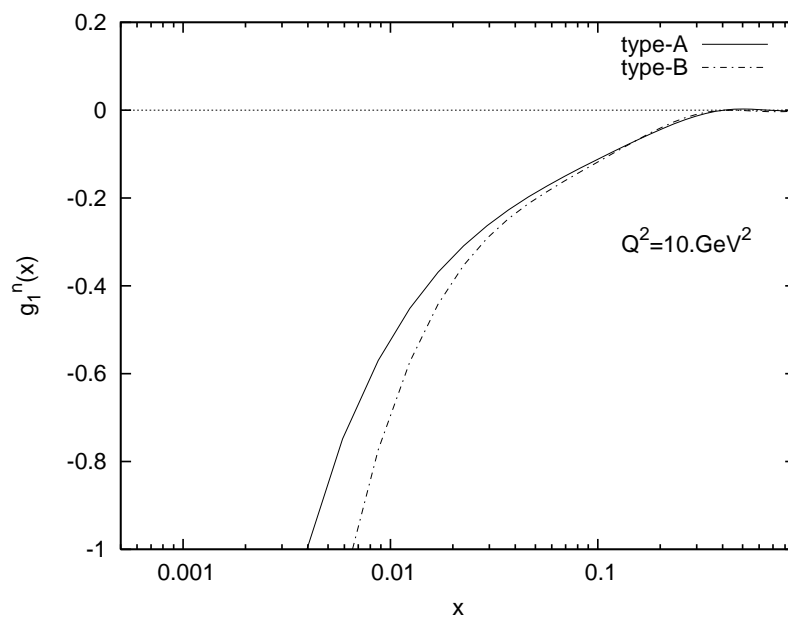


Figure 6.18: Best-fit results of type-A (solid) and type-B (dot-dashed) for the neutron structure function.

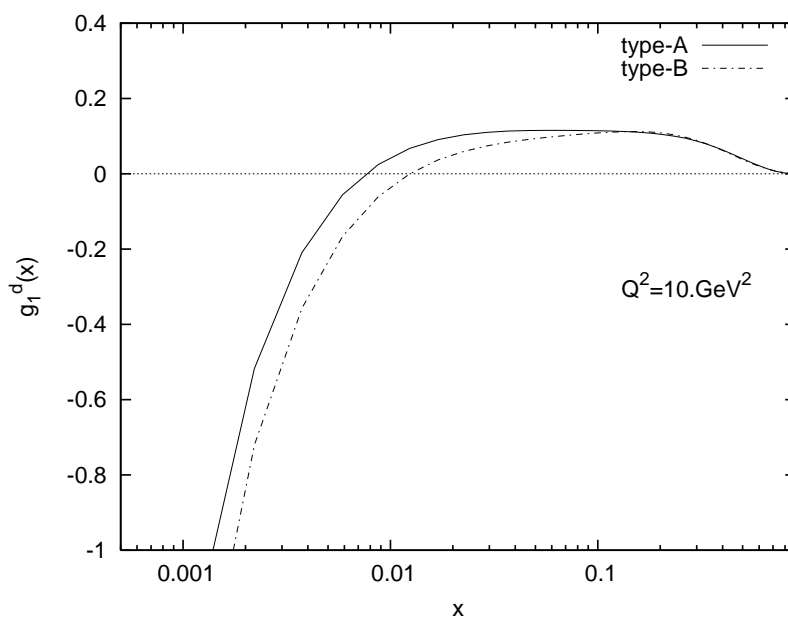


Figure 6.19: Best-fit results of type-A (solid) and type-B (dot-dashed) for the deuteron structure function.

	$\Gamma_1^p(10 \text{ GeV}^2)$	$\Gamma_1^d(10 \text{ GeV}^2)$	$\Gamma_1^n(5 \text{ GeV}^2)$
type-A (full range)	0.125 ± 0.003	0.038 ± 0.003	-0.047 ± 0.004
type-A (meas. range)	0.129	0.047	-0.029
type-B (full range)	0.129 ± 0.004	0.035 ± 0.003	-0.058 ± 0.005
type-B (meas. range)	0.128	0.044	-0.032

Tab. 8. First moment of the structure function g_1^p for proton, deuteron and neutron targets.

6.6.2 Polarized quark and gluon densities

Moments of quark singlet and gluon polarizations as well as the value of the singlet axial charge may be evaluated by taking the average over the central values in the two fits, type-A and B respectively, and the final estimates thus read

$$\begin{aligned}
\Delta\Sigma(1) &= 0.40 \pm 0.02 (\text{exp}) \pm 0.06 (\text{th}) \\
\Delta g(1, 1 \text{ GeV}^2) &= 0.68 \pm 0.12 (\text{exp}) \pm 0.29 (\text{th}) \\
a_0(10 \text{ GeV}^2) &= 0.23 \pm 0.02 (\text{exp}) \begin{matrix} +0.35 \\ -0.16 \end{matrix} (\text{th}).
\end{aligned} \tag{6.9}$$

The first error quoted in Eqs. (6.9) is the one related to the statistical errors from the fit, the second error is the theoretical one.

Indeed, as discussed in [12, 26], the main sources of theoretical uncertainty in the determination of quark and gluon polarizations, and of the related physical quantities, stem from the truncation of the perturbative expansions, as well as from the choice of the assumed initial parametrization of pdfs as emphasized in Sec. 6.5.2.

The error on the gluon first moment $\Delta g(1, 1 \text{ GeV}^2)$ due to the choice of input densities can be evaluated by comparing the results of the type-A and B fits, i.e. by taking the half-difference of the two central values as an estimate of the related uncertainty. It turns out roughly $\simeq \pm 0.12$. Similarly for the singlet quark and the axial charge one has $\simeq \pm 0.05$ and $\simeq \pm 0.01$ respectively. The uncertainty induced by the truncation of the perturbative series for the coefficient functions and the evolution kernels is reflected by the dependence of the results on the renormalization scale μ_R and on the factorization scale μ_F respectively, that are usually both fixed to the value of Q^2 of each data

point. A way of studying the effects of higher orders is by changing the value of μ_R and μ_F around the chosen values. On the basis of the previous analyses [56, 12, 26], the theoretical error on $\Delta g(1, 1 \text{ GeV}^2)$ due to higher order corrections has been estimated to be roughly $\simeq \pm 0.26$. Similarly for $\Delta\Sigma(1)$ and $a_0(10 \text{ GeV}^2)$ one has $\simeq \pm 0.03$ and $\simeq_{-0.16}^{+0.35}$ respectively.

Another source of theoretical uncertainty is due to higher-twist corrections, and, as extensively discussed in Sec. 2.4, the related systematic error has been strongly reduced in the present analysis by discarding very low energy data, i.e. below the cut at the final-state invariant mass $W = 3 \text{ GeV}$. However, by exploiting results of Sec. 2.4.2, an estimate of higher-twist effects may be attained by comparing the results of the same fit of type-A to the whole set of available data (Tab. 4, second column) with the one performed on the selected subset cut at $W \geq 3 \text{ GeV}$ (Tab. 5). The related error on the gluon first moment $\Delta g(1, 1 \text{ GeV}^2)$ amounts to $\simeq \pm 0.06$, and it is thus negligibly small if compared to the theoretical errors from the higher orders and the initial parametrization. For $\Delta\Sigma(1)$ and $a_0(10 \text{ GeV}^2)$ one finds $\simeq \pm 0.01$ and $\simeq \pm 0.02$ respectively.

The overall theoretical uncertainties in Eqs. (6.9) is then obtained by combining the errors quoted above. Other sources of theoretical error, such as the uncertainty on the value of $\alpha_s(M_Z^2)$ and η_8 , and the one related to the positions of heavy quark thresholds, all entail very small effects [56] and have been neglected in the final estimates. Also the impact of target mass corrections is found to be small (see [56, 57]).

In order to compare these results with those of current analyses, it should be recalled that in the Adler-Bardeen factorization scheme the polarized singlet quark density $\Delta\Sigma(1)$ is scale independent, whereas in the $\overline{\text{MS}}$ scheme, adopted in most of the recent works [27, 28, 58, 59], it coincides with the (non conserved) singlet axial charge $a_0(Q^2)$ (see Eq. (5.32)). The polarized gluon density Δg should be the same in the two schemes at NLO accuracy. A reasonable agreement between the above results and the most recent estimates is found. As an example, in Ref. [27] the quoted values read

$$\Delta\Sigma(1, 1 \text{ GeV}^2) = 0.25 \pm 0.10, \quad \Delta g(1, 1 \text{ GeV}^2) = 0.47 \pm 1.08, \quad (6.10)$$

that are very similar to their previous estimates [38].

Furthermore, in Refs. [41, 55] two solutions with either $\Delta g > 0$ or $\Delta g < 0$ have been found; the first moment of Δg at the initial scale turns out to be

small in absolute value, i.e. $|\eta_g| < 0.3$ [41, 55] for both solutions, but the shapes of the distributions are very different. It is finally worth noting that in the analysis of Ref. [41] the positive solution for Δg seems to be favored by the data.

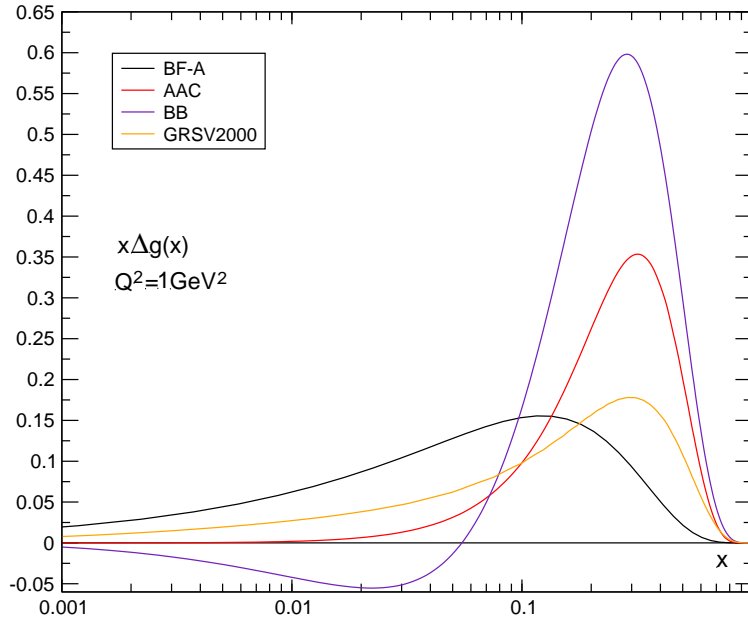


Figure 6.20: Best-fit result (type-A) for $x\Delta g(x)$ compared at $Q^2 = 1 \text{ GeV}^2$ with the other parametrizations, i.e. AAC [38], BB [58] and GRSV [59].

Then, even though the most recent global fits to world data fairly agree within the errors as far as the first moment of the polarized gluon density is concerned, they produce very different shapes of Δg , as shown in Fig. 6.20. Here, the best-fit result of type-A (Tab. 5) is compared at the scale $Q^2 = 1 \text{ GeV}^2$ with other available parametrizations [38, 58, 59] of the spin-dependent gluon distribution. One may thus conclude that to the present accuracy inclusive DIS data are not capable to discriminate among the existing different scenarios, and thus to pin down the x -shape of the gluon polarization. As discussed

extensively in the next section, some light may be shed on this issue by direct measurements of Δg , rather than by scaling violations, that is, by including in the analysis experimental data from exclusive reactions in which gluons contribute at leading order.

Chapter 7

Open-charm photoproduction at COMPASS

The spin-dependent gluon distribution Δg in the nucleon seems to be hardly constrained by the inclusive DIS measurements. Actually, as discussed in Sec. 6, a global fit to world data including the most recent and precise experimental results on the polarized structure function g_1 , allows a better determination of its first moment, that turns out to be much smaller than previous estimates (see e.g.[12, 60]). However, the polarized gluon density exhibits a sizable dependence on the assumed functional form (see Sec. 6.4.2), and, as a result, the x -shape is still largely unknown.

At present, experimental constraints on the gluon polarization are expected to come from exclusive reactions, aimed at measuring Δg directly, rather than through scaling violations. Such measurements entail the observation of specific events that receive leading contributions from gluon initiated subprocesses, such as, for example, production of heavy-flavored hadrons and jets with large transverse momentum. In particular, as discussed below, the open-charm photoproduction represents a promising approach for extracting $\Delta g(x)$. This channel is currently experimentally studied at COMPASS, and first results on the spin asymmetry are upcoming. Therefore, a complete analysis of polarized photoproduction of open-charm at the COMPASS kinematics has been performed in the present work, in order to assess the relevance of such measurements in constraining the x -shape of $\Delta g(x)$.

A brief overview of the current scenario on direct measurements of the gluon

polarization is sketched in Sec. 7.1. Sec. 7.2 is devoted to the theoretical study of the COMPASS experiment, and finally phenomenological results are discussed in Sec. 7.3.

7.1 Direct determination of Δg

Reactions dominated by gluon initiated processes at the partonic level can be investigated with both electromagnetic and strong probes, that is, in lepto- and photo-production reactions and hadro-production respectively.

7.1.1 Experiments at polarized proton-proton colliders

Inelastic proton-proton collisions with polarized beams at high energies provide the possibility to investigate the gluon spin distribution by using strong interaction among partons from the colliding hadrons.

New perspectives have been opened up by the RHIC-Spin (Relativistic Heavy Ion Collider) machine at Brookhaven National Laboratories, where a number of high- p_T processes can be generated by proton beam collisions at c.m.s. energies of $\sqrt{S} = 200 - 500$ GeV, which are sensitive to Δg , such as prompt photon and heavy flavor production, jet, single-inclusive and di-hadron production (see e.g. [61]). Indeed, in all cases, the polarized gluon density plays a prominent role already at LO of QCD, through the underlying hard processes of gluon-gluon fusion and gluon-quark scattering.

Complete NLO corrections to polarized QCD hard-scattering processes, such as high- p_T pion and jet production by polarized proton collisions, are also available [62, 63, 64].

In particular, in the NLO analysis [62] of high- p_T pion hadroproduction, the predicted asymmetry $A_{LL}^{\pi_0}$, i.e. the ratio of polarized and unpolarized cross sections for the specific reaction, exhibits sizable differences for two distinct sets of spin-dependent pdfs [59], which both provide good fit to inclusive DIS data, but differ significantly in the polarized gluon density (see also [64]). The gluon polarizations considered in Ref. [62] are the maximal gluon polarization “GRSV-max” – based on the maximal saturation of the positivity constraint, i.e. the assumption $\Delta g = g$ at the input scale – and the “standard” distribution of the GRSV analysis [59]. The latter in particular is compared

in Fig. 6.20 with the best fit result (type-A) of Sec. 6 and with other available parametrizations. As a result, observed spin asymmetries should be capable of discriminating among different scenarios.

First experimental results from PHENIX and STAR detectors at RHIC on double helicity asymmetry at c.m.s. energy $\sqrt{S} = 200$ GeV, in pion [65] and jet [66] production, probing the kinematic region in the parton momentum fraction $0.03 < x < 0.3$, turn out to be consistent with a moderate gluon polarization, such as the “standard” GRSV distribution [59]. Specifically, the observed asymmetries are small, and a large positive gluon contribution to the nucleon spin, as given by the maximally polarized gluon “GRSV-max” [59], is clearly disfavored by the data [65, 66].

Besides, the PHENIX π_0 data points have been also included in a recent analysis of inclusive DIS world data by the AAC Collaboration [27], and the conclusion was reached that the ensuing uncertainty on Δg is significantly reduced (by about 60%). Nonetheless, within this analysis, along with a positive gluon polarization, a negative gluon distribution in the small- x region – type-1 and -3 respectively [27] – is still consistent with the data, and resides outside the estimated error band of type-1 Δg . Further insights into the low- x shape of the polarized gluon density may be supplied by higher energy runs ($\sqrt{S} = 500$ GeV) at RHIC.

7.1.2 Lepton-nucleon scattering in polarized fixed target experiments

Polarized lepton-nucleon interactions still play a crucial role for investigating the spin structure of the nucleon. In order to obtain observables which are sensitive to the polarized gluon density, one has to consider reactions that are less inclusive than DIS, in which one measures one or more outgoing final-state particles resulting from spin-dependent gluon interactions. The largest cross sections typically stem from the photoproduction regime, which is characterized by scattered leptons at very small angles, and thus by exchanged photons almost on-shell.

A crucial point here is the clear-cut sensitivity of cross sections and spin asymmetries in photoproduction reactions, such as for example heavy flavored hadron production, at both collider and fixed target energies, to the

shape and size of the spin-dependent gluon distribution, as was shown in earlier studies (see e.g. [67, 68]).

At present, experimental results on lepton-nucleon interactions are supplied by low-energy fixed target experiments, where a beam of longitudinally polarized leptons is scattered off longitudinally polarized nucleon targets at c.m.s energies \sqrt{S} of at most few tens GeV.

In the framework of polarized DIS, the gluon polarization can be directly accessed via the underlying photon-gluon fusion (PGF) mechanism, resulting in a quark-antiquark pair. Experimental signatures to tag this subprocess are hadron pairs with high- p_T in the final states, and open-charm events where the $q\bar{q}$ pair is required to be a $c\bar{c}$ pair and an outgoing charmed meson is reconstructed.

First measurements of longitudinal spin asymmetries in high- p_T hadron-pair production are given by HERMES [69] at DESY and more recently by COMPASS [70] at CERN, both in the photoproduction regime, and by SMC [71] at CERN in the DIS region ($Q^2 \geq 1 \text{ GeV}^2$). However, in such a reaction, the measured asymmetries receive contributions not only by pure PGF events, but also by a significant fraction of background events, mainly due to the two competing processes of gluon radiation by QCD Compton scattering ($\gamma^*q \rightarrow qg$) and photon absorption at the lowest order of DIS ($\gamma^*q \rightarrow q$). High- p_T hadron pair photoproduction is affected by large higher order corrections, and a full perturbative understanding is lacking. Estimates of the relative contributions from the background processes then rely on Monte-Carlo simulations, which are tuned to describe the data (see e.g. [70]). The average gluon polarization is probed within a restricted range of momentum fraction, i.e. roughly $x \sim 0.1$, and turned out, on the whole, to be consistent with a moderate gluon polarization (for a summary of such measurements see [70]). Phenomenological studies of hadron-pair polarized photoproduction at HERMES and COMPASS can be found in [72, 73, 74].

7.1.3 The open-charm method at COMPASS

At variance with hadron-pair production, the open-charm approach is free of background, since the PGF subprocess is the main mechanism for producing charm quarks in polarized DIS. A clean perturbative description is thus possible, and higher order corrections have been found to be reasonably small [80].

This approach is currently used at COMPASS [75] to extract the ratio of the polarized and unpolarized gluon distribution $\Delta g/g$. Here, polarized muons with a beam energy of $E_\mu = 160$ GeV scatter off deuterons in a polarized ${}^6\text{LiD}$ target, corresponding to a c.m.s. energy of roughly $\sqrt{S} \simeq 18$ GeV, in the photoproduction regime where the photon virtuality is $Q^2 \simeq 0$ (a description of the experimental setup can be found in [76]). D mesons in the final states, originated from charm quark fragmentation, are reconstructed from their decay products in the channel $D^0 \rightarrow K\pi$, with a branching ratio of only $\sim 4\%$, which results in low statistics. In addition, the channel $D^* \rightarrow D^0\pi_s$, where π_s is a slow pion, is studied, increasing the signal-to-background ratio [77].

From the measured spin asymmetry A_{LL} a preliminary determination of $\Delta g/g$ has been obtained by a LO analysis in QCD, that relies on the approximate relation [78]

$$A_{LL} = R_{\text{PGF}} \hat{a}_{LL} \frac{\Delta g}{g} + A_{\text{BG}}, \quad (7.1)$$

where \hat{a}_{LL} is the partonic asymmetry, i.e. the ratio of spin-dependent and spin-averaged hard cross sections, R_{PGF} is the fraction of PGF events in the selected sample and A_{BG} is the background asymmetry. An estimation of \hat{a}_{LL} on a event-by-event basis is then provided as a function of the measured kinematical variables, and is based on the comparison of the data sample with Monte-Carlo studies (see [79] for details on the analysis method).

The extracted value [79] of $\Delta g/g$ for data collected from 2002 up to 2004 turned out to be negative, i.e. $\langle \Delta g/g \rangle = -0.57 \pm 0.41$ (stat) ± 0.17 (syst), but still consistent with zero, and represents an average over the probed x -range, $\langle x \rangle \simeq 0.15$. The hard scale is approximatively given by the charm quark mass $\mu^2 = 4(m_c^2 + p_{tD}^2) \simeq 13 \text{ GeV}^2$, where p_{tD} is the D^0 meson transverse momentum with respect to the photon direction.

However, the above Monte-Carlo approach entails a number of approximations, thus missing a clean theoretical description of the process. On the other hand, as already noted, since the photon-gluon fusion is the main underlying mechanism for producing charm quarks by polarized lepton-nucleon scattering, the open-charm reaction can be reliably calculated in perturbation theory, with the charm quark mass as the hard scale required.

7.2 Theoretical analysis of charm asymmetries at COMPASS

A thorough analysis of open-charm production from deep inelastic muon scattering off nucleons, with longitudinally polarized beam and target, has been performed here in the photoproduction approximation, where only quasi-real photons ($Q^2 \simeq 0$), radiated from the incoming leptons, are considered. The analysis is indeed tailored to the COMPASS experiment [75, 79] with relation to upcoming results on spin asymmetries in open-charm photoproduction, and is aimed at assessing the sensitivity of the actually observed quantities to the polarized gluon distribution.

As already noted, many earlier studies of heavy quark polarized photoproduction, at both high and low energy up to NLO, are also available [67, 68, 80]. This issue is here re-analysed by constructing a close theoretical description of the experimental spin asymmetry at COMPASS, as a function of the measured kinematic variables.

7.2.1 General framework

The spin-dependent and spin-averaged cross sections are defined by

$$\Delta\sigma = \frac{1}{2} [\sigma^{\uparrow\uparrow} - \sigma^{\uparrow\downarrow}] \quad \text{and} \quad \sigma = \frac{1}{2} [\sigma^{\uparrow\uparrow} + \sigma^{\uparrow\downarrow}] \quad (7.2)$$

respectively, where the arrows denote parallel and opposite helicities of the scattering particles. The spin-dependent photoproduction cross section for the process $lN \rightarrow l'HX$, where a longitudinally polarized lepton beam scatters off a longitudinally polarized nucleon target producing one observed hadron H in the final state, can be written, on the basis of factorization theorem of QCD, as

$$d\Delta\sigma_{lN} = \sum_{ijk} \int dx_i dx_j dz_k \Delta f_i^{(l)}(x_i, \mu_F) \Delta f_j^{(N)}(x_j, \mu_F) \quad (7.3) \\ \times d\Delta\hat{\sigma}_{ij}(x_i, x_j, S, P_H/z_k, \mu_R, \mu_F, \mu'_F) D_k^H(z_k, \mu'_F).$$

Here, $\Delta f_j^{(N)}(x_i, \mu_F)$ is the usual polarized parton density in the nucleon at the factorization scale μ_F , and the non-perturbative function $D_k^H(z_k, \mu'_F)$ describes

the fragmentation process of the produced parton k into the observed hadron H at the scale μ'_F , with momentum fraction z_k . The polarized hard scattering cross section $d\Delta\hat{\sigma}_{ij}$ can be calculated in QCD order-by-order in the strong coupling $\alpha_s(\mu_R^2)$, μ_R being the renormalization scale, and the sum in Eq. (7.3) is taken over all partonic channels. Finally, the function $\Delta f_i^{(l)}(x_i, \mu_F)$ represents the parton density in the lepton.

In the framework of the photoproduction approximation, which is the physically interesting case in connection with the COMPASS experiment, the initial-state lepton is considered as a source of quasi-real photons (equivalent-photon approximation), with energy distribution given by the Weizsacker-Williams spectrum [81] that can be theoretically computed. The function $\Delta f_i^{(l)}$ is given by the polarized Weizsacker-Williams function [82]

$$\Delta f_\gamma^{(l)}(y) = \frac{\alpha_{\text{em}}}{2\pi} \left[\frac{1 - (1-y)^2}{y} \ln \frac{Q_{\text{max}}^2(1-y)}{m_l^2 y^2} + 2m_l^2 y^2 \left(\frac{1}{Q_{\text{max}}^2} - \frac{1-y}{m_l^2 y^2} \right) \right], \quad (7.4)$$

where m_l is the lepton mass, y the lepton momentum fraction carried by the radiated photon and Q_{max} is the allowed upper value to the photon's virtuality, to be fixed according to the experimental conditions [83]. The unpolarized counterpart of Eq. (7.4) reads [83]

$$f_\gamma^{(l)}(y) = \frac{\alpha_{\text{em}}}{2\pi} \left[\frac{1 + (1-y)^2}{y} \ln \frac{Q_{\text{max}}^2(1-y)}{m_l^2 y^2} + 2m_l^2 y \left(\frac{1}{Q_{\text{max}}^2} - \frac{1-y}{m_l^2 y^2} \right) \right]. \quad (7.5)$$

Actually, quasi-real photons undergo interactions with partons in the nucleon either directly (“point-like” component) or via their partonic structure (“resolved” or “hadronic” component). In the first case photons simply interact as elementary point-like particles, whereas in the second case photons fluctuate into a hadronic state, before the hard QCD interaction takes place, and the so-called “resolved” contributions to the cross section compete with the “direct” part. Therefore, the experimentally measurable cross section is the sum of the point-like and the resolved photon contributions (see for example [84, 85, 86] and references therein)

$$d\Delta\sigma_{lN} = d\Delta\sigma_{lN}^{\text{dir}} + d\Delta\sigma_{lN}^{\text{res}}. \quad (7.6)$$

Here, the direct component is given by Eqs. (7.3) and (7.4), and the resolved component can also be cast in the form of Eq. (7.3), by properly defining the

parton density of the lepton as the convolution product [68]

$$\Delta f_i^{(l)}(x_i, \mu_F) = \int_{x_i}^1 \frac{dy}{y} \Delta f_\gamma^{(l)}(y) \Delta f_i^{(\gamma)}\left(\frac{x_i}{y}, \mu_F\right), \quad (7.7)$$

with $\Delta f_\gamma^{(l)}(y)$ given by Eq. (7.4). The partonic content of the polarized photon is unmeasured so far and models are usually invoked [87] in actual calculations. Furthermore, the direct photon contribution can be viewed as a particular case of Eq. (7.7), by defining

$$\Delta f_i^{(\gamma)} = \delta \left(1 - \frac{x_i}{y}\right). \quad (7.8)$$

The corresponding spin-averaged cross sections are finally given by Eq. (7.3) replacing polarized parton densities and hard cross sections by the related unpolarized quantities. The experimentally relevant observable is the spin asymmetry, i.e. the ratio of polarized and unpolarized cross sections

$$A_{LL} = \frac{d\Delta\sigma_{lN}}{d\sigma_{lN}}. \quad (7.9)$$

Focussing on the determination of the gluon polarization from photoproduction reactions, such resolved contributions act as a background. Extensive analyses of their relevance with relation to the kinematic regime have been performed in studies on high-energy lepton-proton collisions (see e.g. [68, 85, 88]), in view of the polarized mode of HERA at DESY and the planned eRHIC project at BNL [89]. Lower energies (fixed-target) experiments are generally expected to be less sensitive to the unmeasured partonic content of the polarized photon (see [85, 88] and references therein), and LO estimates [68] have revealed that the resolved contributions are negligibly small in the case of polarized photoproduction of charm quarks at COMPASS energies. In the analysis of this experiment, one can thus safely neglect the resolved piece in Eq. (7.6).

In the case of open-charm photoproduction, as already noted, the only partonic subprocess contributing in LO to the spin-dependent cross section Eq. (7.3), is photon-gluon fusion $\gamma g \rightarrow c\bar{c}$. However, in the NLO approximation of QCD, along with 1-loop virtual corrections to PGF and real corrections with an additional gluon in the final state, new subprocesses, induced by a light quark (antiquark) replacing the gluon in the initial-state,

i.e. $\gamma q(\bar{q}) \rightarrow c\bar{c}q(\bar{q})$, can also contribute, diluting the dependence of the asymmetry on $\Delta g(x)$.

All NLO contributions have been explicitly calculated in [80], for the polarized case ¹, and found to be reasonably small (around 10%) in the energy range accessible at COMPASS (roughly $\sqrt{S_{\gamma N}} \simeq 12$ GeV), and should be outside of the present level of experimental accuracy at COMPASS [75]. Furthermore, the background due to the light quark induced subprocesses turned out [80] to be fairly negligible. In particular, the PGF mechanism dominates in the COMPASS kinematical region, and a clear determination of Δg may be performed by detecting open-charm events.

On this basis, the theoretical analysis of the spin asymmetries in open-charm photoproduction is performed below at the leading order of QCD, and by retaining only the point-like photon channel. The calculation is then specialized to the COMPASS kinematics in order to reconstruct the actual experimentally observed quantities.

7.2.2 Leading order cross section

Open-charm events in the final states are a clear signature of the LO PGF channel, namely

$$\gamma(q, \lambda_\gamma) + g(p, \lambda_g) \rightarrow c(k) + \bar{c}(k'), \quad (7.10)$$

where, λ_γ , q and λ_g , p denote photon and gluon helicities and four-momenta respectively, such that $q^2 = p^2 = 0$. For the outgoing heavy quark pair $k^2 = k'^2 = m_c^2$, m_c being the charm quark mass. The corresponding Mandelstam variables are then defined by

$$s = (q + p)^2, \quad t_1 = (p - k)^2 - m_c^2, \quad \text{and} \quad u_1 = (q - k)^2 - m_c^2, \quad (7.11)$$

with $s + t_1 + u_1 = 0$. To order $\mathcal{O}(\alpha_{\text{em}}\alpha_s)$ the differential partonic cross section can be written as [67, 93]

$$\frac{d^2 \hat{\sigma}_{\gamma g}}{dt_1 du_1}(s, t_1, u_1, \lambda_\gamma, \lambda_g) = \frac{2\pi\alpha_{\text{em}}\alpha_s(\mu_R^2)}{9s^2} [\Sigma + \lambda_\gamma\lambda_g\Delta] \delta(s + t_1 + u_1) \quad (7.12)$$

¹The NLO QCD corrections in the unpolarized case have been calculated for the first time in Refs. [90, 91]. Photoproduction of heavy quarks in the unpolarized case at fixed target experiments has been extensively studied [92].

with

$$\Sigma = -\frac{8m_c^4 s^2}{t_1^2 u_1^2} + 2\frac{t_1^2 + u_1^2 + 4m_c^2 s}{t_1 u_1}, \quad (7.13)$$

$$\Delta = \frac{4m_c^2(t_1^3 + u_1^3)}{t_1^2 u_1^2} + 2\frac{t_1^2 + u_1^2 - 2m_c^2 s}{t_1 u_1}. \quad (7.14)$$

The spin-dependent and spin-averaged hard cross sections are defined as usual by

$$d\Delta\hat{\sigma}_{\gamma g} = \frac{1}{2} [d\hat{\sigma}_{\gamma g}^{\uparrow\uparrow} - d\hat{\sigma}_{\gamma g}^{\uparrow\downarrow}], \quad d\hat{\sigma}_{\gamma g} = \frac{1}{2} [d\hat{\sigma}_{\gamma g}^{\uparrow\uparrow} + d\hat{\sigma}_{\gamma g}^{\uparrow\downarrow}] \quad (7.15)$$

respectively, where the arrows denote parallel and antiparallel polarizations of incoming photons and gluon. The Born-level cross sections thus explicitly read

$$\frac{d^2\Delta\hat{\sigma}_{\gamma g}}{dt_1 du_1} = \frac{4\pi\alpha_{\text{em}}\alpha_s}{9s^2} \left(\frac{t_1}{u_1} + \frac{u_1}{t_1} \right) \left(1 - \frac{2m_c^2 s}{t_1 u_1} \right) \delta(s + t_1 + u_1), \quad (7.16)$$

$$\frac{d^2\hat{\sigma}_{\gamma g}}{dt_1 du_1} = \frac{4\pi\alpha_{\text{em}}\alpha_s}{9s^2} \left[\frac{t_1}{u_1} + \frac{u_1}{t_1} + \frac{4m_c^2 s}{t_1 u_1} \left(1 - \frac{m_c^2 s}{t_1 u_1} \right) \right] \delta(s + t_1 + u_1). \quad (7.17)$$

Physical cross sections for the leptonproduction process $\mu N \rightarrow \mu' H X$ where H is a charmed meson in the final state, can be related to the photoproduction analogue by the Weizsacker-Williams function Eq. (7.4). To order $\mathcal{O}(\alpha_{\text{em}}\alpha_s)$, at the partonic level only the gluon distribution is relevant. Then Eq. (7.3), in the unpolarized (polarized) case, can be now rewritten schematically as

$$d(\Delta)\sigma_{\mu N} = \int_{y_{\text{min}}}^{y_{\text{max}}} dy (\Delta) f_{\gamma}^{(\mu)}(y) d(\Delta)\sigma_{\gamma N} \quad (7.18)$$

where $(\Delta) f_{\gamma}^{(\mu)}(y)$ is given by Eq. (7.5) (Eq. (7.4)), $q = yP_{\mu}$ with P_{μ} the incoming muon four-momentum, and the integration range over y is fixed by the experimental conditions. The photoproduction cross section in Eq. (7.18) at LO is given by

$$d(\Delta)\sigma_{\gamma N} = \int dx (\Delta) g(x, \mu_F^2) \int dz D_c^H(z) d(\Delta)\hat{\sigma}_{\gamma g}(x, z, y, S, T, U, \mu_R^2), \quad (7.19)$$

where the (photoproduction) hadronic invariants S, T, U are related to their partonic counterparts by

$$s = xS, \quad t_1 = \frac{xT}{z} \quad \text{and} \quad u_1 = \frac{U}{z}. \quad (7.20)$$

The only parton distribution involved at LO is the unpolarized (polarized) gluon density $(\Delta)g(x, \mu_F^2)$, whereas $D_c^H(z)$ is the non-perturbative fragmentation function of a produced charm quark into an observed charmed meson. Using the expressions Eqs. (7.16) and (7.17) of the hard scattering cross sections, Eq. (7.19) explicitly reads

$$\begin{aligned} \frac{d^2 \Delta \sigma_{\gamma N}}{dT dU} &= \frac{4\pi \alpha_{\text{em}} \alpha_s(\mu_R^2)}{9S^2} \int \frac{dx}{x} \Delta g(x, \mu_F^2) \int \frac{dz}{z^2} D_c^H(z) \times \\ &\quad \left(\frac{U}{xT} + \frac{xT}{U} \right) \left(1 - \frac{2m_c^2 z^2 S}{TU} \right) \delta \left(xS + \frac{xT}{z} + \frac{U}{z} \right), \end{aligned} \quad (7.21)$$

$$\begin{aligned} \frac{d^2 \sigma_{\gamma N}}{dT dU} &= \frac{4\pi \alpha_{\text{em}} \alpha_s(\mu_R^2)}{9S^2} \int \frac{dx}{x} g(x, \mu_F^2) \int \frac{dz}{z^2} D_c^H(z) \times \\ &\quad \left[\frac{U}{xT} + \frac{xT}{U} + \frac{4m_c^2 z^2 S}{TU} \left(1 - \frac{m_c^2 z^2 S}{TU} \right) \right] \delta \left(xS + \frac{xT}{z} + \frac{U}{z} \right), \end{aligned} \quad (7.22)$$

in the spin-dependent and spin-averaged case respectively.

Actually, if the momentum fraction y of the incoming muon carried by the photon is reconstructed event-by-event, the open-charm asymmetries do depend on y , as well as on the measured variables of the outgoing D meson. Within this framework, no average over the Weizsacker-Williams spectrum, Eq. (7.18), is required, and the observed quantity is consistently described by the photoproduction asymmetry

$$A_{LL}^D = \frac{d\Delta \sigma_{\gamma N}}{d\sigma_{\gamma N}} \quad (7.23)$$

with $d(\Delta)\sigma_{\gamma N}$ given by Eqs. (7.21) and (7.22).

7.2.3 COMPASS kinematics

Specifying the above general discussion to the case of the (fixed target) open-charm experiment at COMPASS, the muon momentum fraction y carried by

the photon is indeed reconstructed event-by-event with no experimental cut. Thus, the polarized and unpolarized cross sections in Eq. (7.23) are double differential distributions, parametrized by the measured D meson variables in the nucleon rest frame, that is, the transverse momentum p_{tD} with respect to the photon direction, and the energy fraction $z_D = E_D/E_\gamma$ with respect to the photon energy E_γ . They also depend on y through the incoming photon energy, given as a function of the muon beam energy $E_\gamma = yE_\mu$, with $E_\mu = 160$ GeV. The hadronic invariant system in the laboratory frame then reads

$$T = -Sz_D, \quad U = -\frac{S^2}{2M^2}(z_D - \chi_D) \quad \text{and} \quad S = 2ME_\gamma \quad (7.24)$$

$$\text{with} \quad \chi_D = \sqrt{z_D^2 - \frac{4M^2m_{tD}^2}{S^2}}, \quad (7.25)$$

and $m_{tD} = \sqrt{p_{tD}^2 + m_D^2}$, i.e. the D meson transverse mass. Using the Jacobian $dTdU = (2p_{tD}S/\chi_D)dz_Ddp_{tD}$ to express Eqs. (7.21) and (7.22) in the nucleon rest frame variables Eq. (7.24), the relevant spin-dependent and spin-averaged physical cross sections become

$$\begin{aligned} \frac{d^2\Delta\sigma_{\gamma N}}{dp_{tD} dz_D} &= \frac{16\pi\alpha_{\text{em}}\alpha_s(\mu^2)M^2}{9S^3} \frac{p_{tD}}{z_D\chi_D(z_D - \chi_D)} \int_{x_{\text{min}}}^1 \frac{dx}{x} \Delta g(x, \mu^2) (z_D + w_D) \\ &\times \left[1 - \frac{2z_D w_D}{(z_D + w_D)^2} \right] \left[1 - \frac{4m_c^2 M^2}{z_D(z_D - \chi_D)S^2} (z_D + w_D)^2 \right] D(z_D + w_D) \end{aligned} \quad (7.26)$$

and

$$\begin{aligned} \frac{d^2\sigma_{\gamma N}}{dp_{tD} dz_D} &= \frac{16\pi\alpha_{\text{em}}\alpha_s(\mu^2)M^2}{9S^3} \frac{p_{tD}}{z_D\chi_D(z_D - \chi_D)} \int_{x_{\text{min}}}^1 \frac{dx}{x} g(x, \mu^2) (z_D + w_D) \times \\ &\left[1 - \frac{2z_D w_D}{(z_D + w_D)^2} + \frac{4m_c^2}{xS} \left(1 - \frac{2m_c^2 M^2}{z_D(z_D - \chi_D)S^2} (z_D + w_D)^2 \right) \right] D(z_D + w_D), \end{aligned} \quad (7.27)$$

respectively, where the shorthand

$$w_D = \frac{(z_D - \chi_D)S}{2xM^2} \quad (7.28)$$

has been used. The actual observable at COMPASS is finally the ratio of Eqs. (7.26) and (7.27), according to Eq. (7.23).

It is worth noting that in Eqs. (7.26) and (7.27) integration over the fragmentation variable z has been explicitly performed, being constrained by the δ -function. Moreover, the integration range over the gluon momentum fraction x depends on the measured variables through the relation

$$x_{\min}(p_{tD}, z_D) = \frac{E_\gamma}{M} \left(\frac{z_D - \chi_D}{1 - z_D} \right). \quad (7.29)$$

On the other hand, if one explicitly integrates over x , the integration threshold over z is constrained by the relation

$$z_{\min}(p_{tD}, z_D) = z_D + \frac{E_\gamma}{M} (z_D - \chi_D). \quad (7.30)$$

This actually means that the gluon momentum fraction x and the fragmentation variable z are not independent variables.

The strong coupling $\alpha_s(\mu_R^2)$, as well as the polarized gluon density $\Delta g(x, \mu_F^2)$ are evaluated in NLO at the common fixed value $\mu_R = \mu_F = 2m_c$ for the renormalization and factorization scales respectively. For the charm quark mass $m_c = 1.5$ GeV is taken, $M \simeq 0.938$ GeV for the nucleon mass, and the D mass is taken as an average of the experimentally detected D^0 and D^* masses [8], roughly $m_D \simeq 1.94$ GeV. The strong coupling is normalized as $\alpha_s(M_Z^2) \simeq 0.118$ at the Z boson mass [8].

Note that the experimental cut $z_D \gtrsim 0.2$ is imposed on the fractional D energy, and the most populated bins are estimated [75] as $0.32 \lesssim z_D \lesssim 0.66$ and $0.35 \lesssim p_{tD} \lesssim 1$ GeV.

Finally, as far as Eqs. (7.29) and (7.30) are concerned some comments are in order. Indeed, for fixed values of the observed kinematic variables z_D, p_{tD} , the fragmentation variable z is completely fixed by the momentum fraction x , and thus only the integral over x remains as shown by the expression of the cross sections Eqs. (7.26) and (7.27). Furthermore, the integration threshold over x is determined by the values of z_D and p_{tD} . This bound, given by Eq. (7.29), is displayed in Figs. 7.1 and 7.2 as a function of each of the two variables. As expected, the low x region ($x \lesssim 0.1$) is unaccessible at COMPASS energies, and the integration region involved is stretched towards larger x with increasing p_{tD} (Fig. 7.1). The same situation is observed as the

D meson energy approaches the kinematical boundaries (Fig. 7.2), whereas in the physically meaningful region of z_D x_{\min} is nearly constant ($x_{\min} \sim 0.1$). As already noted, one could equivalently determine x for given z and then only the integration over z remains. In such a case, it is the fragmentation variable z which is bounded from below with z_{\min} determined by z_D and p_{tD} according to Eq. (7.30). The bound on z is displayed in Figs. 7.3 and 7.4 versus z_D and p_{tD} respectively. Both figures show that a sizable amount of the charm quark momentum is carried by the D meson in the whole kinematical region.

7.2.4 Pdfs and fragmentation function

The sensitivity of the asymmetry on the spin-dependent gluon distribution $\Delta g(x, \mu_F^2)$ is investigated here by using three (NLO) parametrizations, obtained from fit to inclusive DIS data, namely AAC [38], BB [58], and the most recent best-fit result BF-A (i.e. type-A) discussed in Sec. 6.5.1.

The use of NLO parton distributions in a LO calculation has obviously no effect on the accuracy of the calculation which remains LO. Note also that the AAC and BB polarized gluons are given in the $\overline{\text{MS}}$ factorization scheme, whereas the BF-A gluon is given in the Adler-Bardeen scheme. However, as already noted, the polarized gluon densities are the same in the two schemes at NLO accuracy. The three parametrizations used for $\Delta g(x, \mu_F^2)$ are displayed at the common scale $\mu_F = 2m_c$ in Fig. 7.5, together with the MRST2004f4 [94] unpolarized gluon distribution, which is used as a rule in the spin-averaged cross section Eq. (7.27).

In Fig. 7.6 the LO and NLO MRST2004f4 parametrizations for the unpolarized gluon distribution $g(x)$ are compared in the region of interest for x ($x \gtrsim 0.1$), at the scale $\mu = 2m_c$. This will be used to estimate the dependence of the results on the unpolarized gluon distribution.

Note also that some of the available LO parametrizations of $\Delta g(x)$ (e.g. BB and LSS [28]) violate the positivity constraint imposed by the LO MRST determination of $g(x)$ at intermediate and large x . This problem is also marginally present for the NLO BB polarized gluon as seen in Fig. 7.5, but does not affect significantly the analysis. Indeed, the uncertainty on the unpolarized gluon at large- x makes violation of the positivity bound less serious.

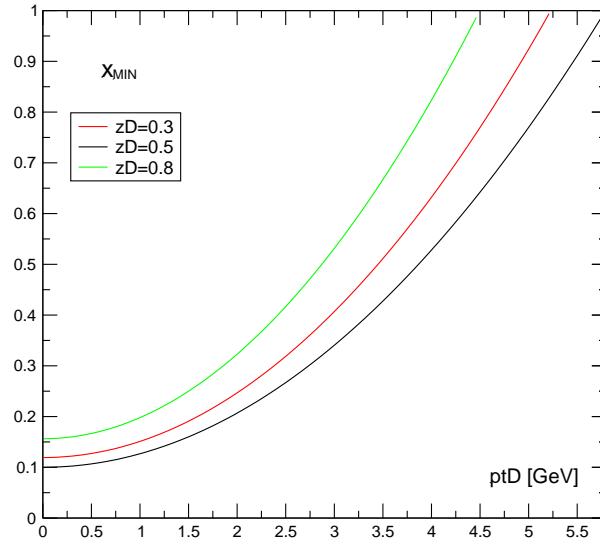


Figure 7.1: Variation of the lower bound x_{min} in the integration over the gluon momentum fraction x , as a function of p_{tD} at three different values of z_D .

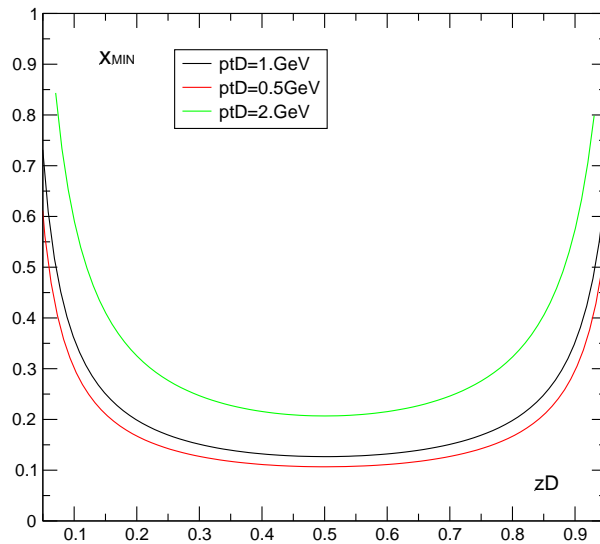


Figure 7.2: Variation of the lower bound x_{min} in the integration over the gluon momentum fraction x , as a function of z_D at three different values of p_{tD} .

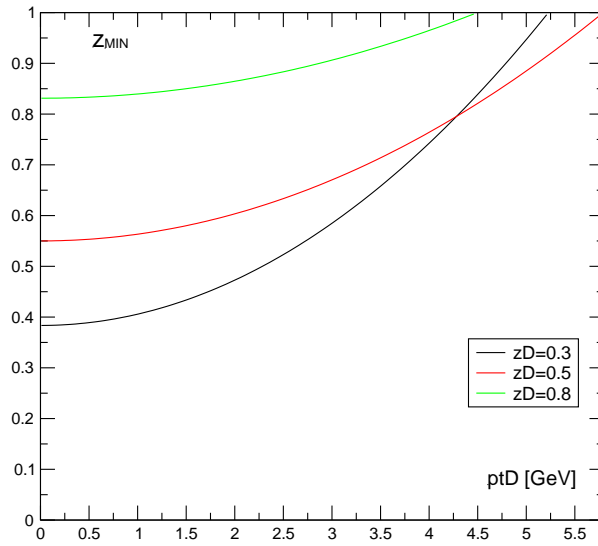


Figure 7.3: Variation of the lower bound z_{\min} in the integration over the fragmentation variable z , as a function of p_{tD} at three different values of z_D .

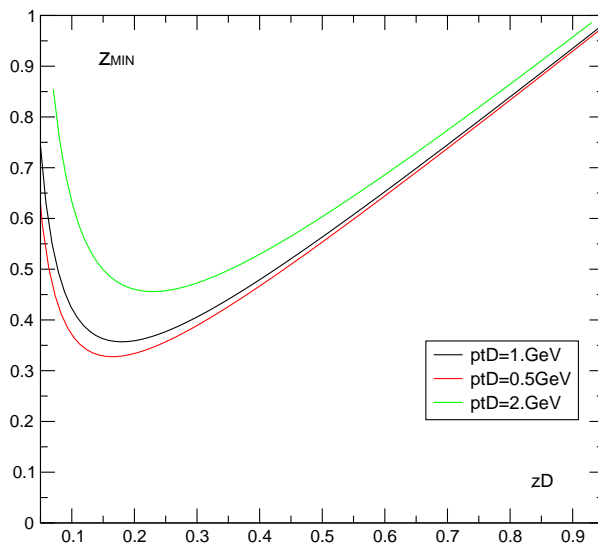


Figure 7.4: Variation of the lower bound z_{\min} in the integration over the fragmentation variable z , as a function of z_D at three different values of p_{tD} .

Finally, for the fragmentation function of a charm quark into a D meson (D^0 and D^*) the non-perturbative Peterson (P) function [95]

$$D_c^H(z) = \frac{N}{z[1 - 1/z - \varepsilon/(1 - z)]^2} \quad (7.31)$$

is used as a baseline, with N the normalization factor. The phenomenological parameter ε , that is predicted to scale as $\varepsilon \sim \Lambda_{\text{QCD}}^2/m_Q^2$ in the fragmentation of a heavy quark Q , is fixed to the usual value $\varepsilon = 0.06$ [96] (see also [97]). In Fig. 7.7 the Peterson fragmentation function Eq. (7.31) is compared to the slightly different parametrization (CN) given in Ref. [98], namely

$$D_c^H(z) = N(1 - z)^{a_1} z^{a_2}, \quad a_1 = 0.8, \quad a_2 = 3.2. \quad (7.32)$$

The latter is also used in the present analysis in order to estimate the impact of the precise shape of the fragmentation function on the results.

7.3 Phenomenological results

The theoretically predicted asymmetries A_{LL}^D , given by Eqs. (7.23), (7.26) and (7.27), are analysed here as a function of the relevant kinematic variables y, z_D, p_{tD} , so as to determine their sensitivity to the polarized gluon density. Next, the effect of including COMPASS results in a global fit of pdfs, along with inclusive DIS data, is discussed by using pseudo-data generated on the basis of the theoretical prediction and the expected statistical error.

7.3.1 Asymmetries as a function of the measured variables

The asymmetries A_{LL}^D as a function of the incoming photon energy $E_\gamma = yE_\mu$ are compared in Fig. 7.8 for the aforementioned parametrizations of $\Delta g(x)$. The D meson transverse momentum and fractional energy are fixed to the values $p_{tD} = 1$ GeV and $z_D = E_D/E_\gamma = 0.4$, corresponding roughly to a maximum in both the polarized and unpolarized cross sections at the COMPASS kinematics. With increasing photon energy, the asymmetry slowly decreases due to the faster growth of the unpolarized cross section, similarly

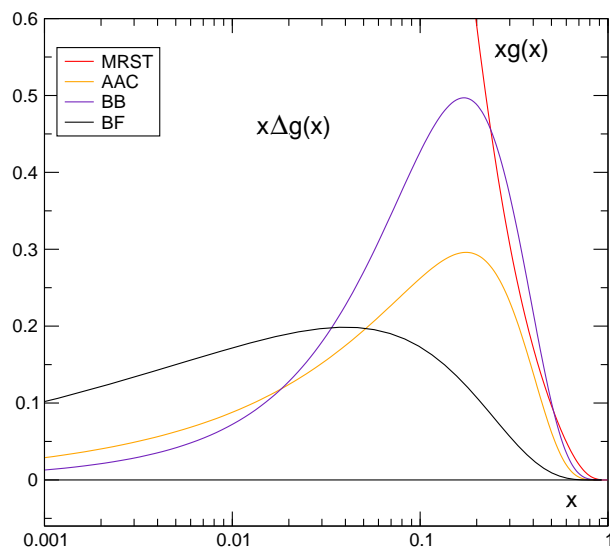


Figure 7.5: NLO parametrizations of gluon distribution functions used in the analysis, namely MRST2004f4 [94] for $g(x)$, AAC [38], BB [58] and the most recent best-fit result BF-A for $\Delta g(x)$, at the scale $\mu_F^2 = 4m_c^2$.

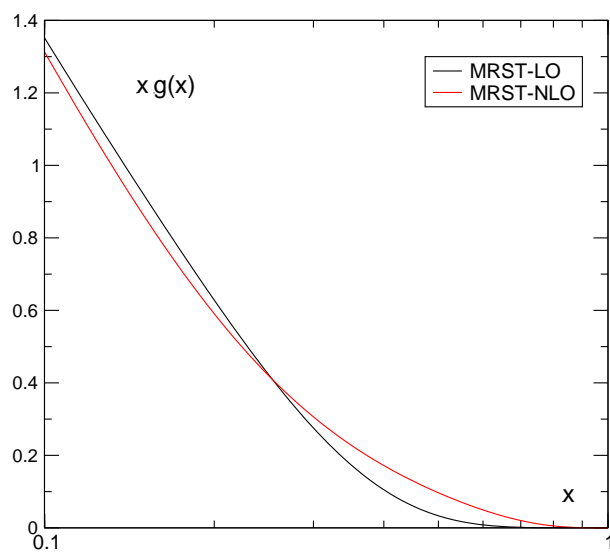


Figure 7.6: LO and NLO MRST2004f4 parametrizations [94] of the unpolarized gluon distribution in the region of interest, at the scale $\mu_F^2 = 4m_c^2$.

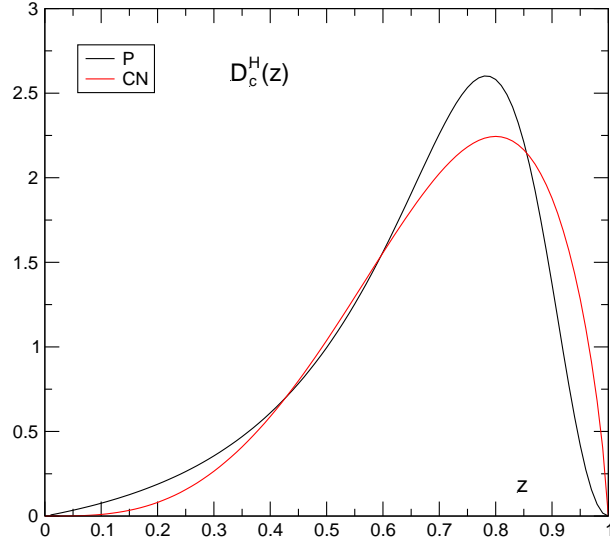


Figure 7.7: Fragmentation functions $D_c^H(z)$ used in the analysis, namely Eq. (7.31) (P) [95, 96] and Eq. (7.32) (CN) [98].

to the case of total charm photoproduction [68]. The gluon polarization has a significant impact on the size of the asymmetry, in that the normalization is mostly determined by the value of $\Delta g(x)$ for $x > x_{\min} \approx 0.1$. Because for all the given parametrizations $\Delta g(x)$ is rapidly decreasing in this region, the asymmetry is in fact essentially determined by the value of $\Delta g(x_{\min})$. This is indeed in substantial agreement with the estimated [79] average $x = \langle 0.15 \rangle$ over the probed region at COMPASS. The shape of the asymmetry is instead dominated by that of the underlying hard process.

The y -shape of A_{LL}^D is also displayed in Fig. 7.9 at different fixed values of p_{tD} , and for the same polarized gluon density BF-A, used as a benchmark in what follows. As the measured transverse momentum p_{tD} is increased the large x region of $g(x)$ and $\Delta g(x)$ is probed. Because the ratio $\Delta g(x)/g(x)$ increases with x , the asymmetry correspondingly increases with growing p_{tD} .

The asymmetry as a function of the fractional energy z_D is given in Fig. 7.10 at fixed photon energy $y = 0.5$ and $p_{tD} = 1 \text{ GeV}$, for the three different parametrizations of $\Delta g(x)$. Once again the normalization is determined

mostly by the value of $\Delta g(x_{\min})$ and the shape by that of the underlying hard process. The whole kinematically allowed region is displayed, even though the COMPASS data are cut at $z_D > 0.2$. Note that in the small $z_D \lesssim 0.2$ region x_{\min} grows as z_D decreases. Therefore, this kinematical region probes Δg at increasingly large values of x , and it is thus sensitive to the poorly known polarized gluon at large x . The asymmetry (and even the individual cross sections) in this region remains sizable despite the fact that the pdf is very small.

Fig. 7.11 displays again the effects of increasing p_{tD} , that is, of sampling only events with larger x , with $\Delta g(x)$ again given by BF-A.

The p_{tD} distribution is shown in Fig. 7.12, as before for the three parametrizations of $\Delta g(x)$, at fixed values of y_D and z_D . The observed p_{tD} , being the minimum transverse momentum of the parent charm quark, is directly related to the minimum gluon momentum required to initiate the process. Generally

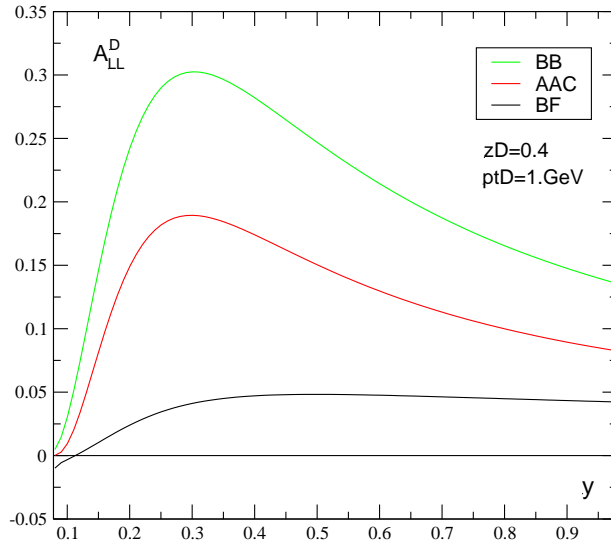


Figure 7.8: The spin asymmetry as a function of the photon energy $y = E_\gamma/E_\mu$, at $p_{tD} = 1$ GeV and $z_D = E_D/E_\gamma = 0.4$. Three (NLO) parametrizations for the Δg are used, namely AAC, BB and BF-A, whereas g is given by MRST2004f4 (NLO). The Peterson fragmentation function is used with $\varepsilon = 0.06$.

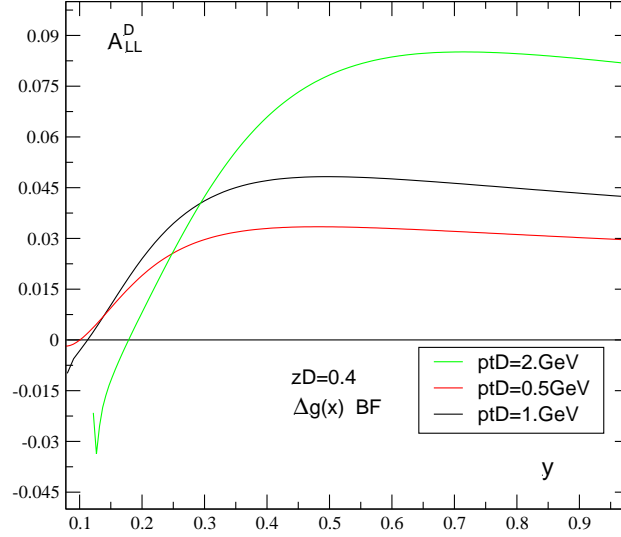


Figure 7.9: The spin asymmetry as a function of y at different p_{tD} and Δg given by BF-A (z_D , $g(x)$) and $D_c^H(z)$ as in Fig. 7.8)

speaking, at low p_{tD} (less than 1 GeV) a larger sample of allowed partonic events contributes, but the measurable asymmetry is small. On the other hand, the high p_{tD} region (greater than 3 GeV) corresponds to a smaller sample of subprocesses restricted to larger x , where the uncertainty in the unpolarized gluon distribution dominates.

Figs. 7.13 and 7.14 show the dependence of the results on the unpolarized gluon distribution by comparing the p_{tD} -shape of A_{LL}^D obtained using the LO and NLO MRST parametrizations of $g(x)$ and two different polarized gluon distributions, AAC and BF-A respectively. In both cases, at LO the positivity constraint is violated by the gluon distributions at large x . Specifically, the asymmetry exceeds 1 at $p_{tD} \geq 3$ GeV if Δg is given by AAC (Fig. 7.13), and at $p_{tD} \geq 4.7$ GeV with BF-A (Fig. 7.14). This is due to the fact that both polarized and unpolarized cross sections become very small in this region. Actually, the large difference in the asymmetries in the two cases, that is, with the LO and the NLO parametrizations of $g(x)$, in both Figs. 7.13 and 7.14, indicates that for $p_{tD} \gtrsim 2$ GeV the uncertainty in the unpolarized

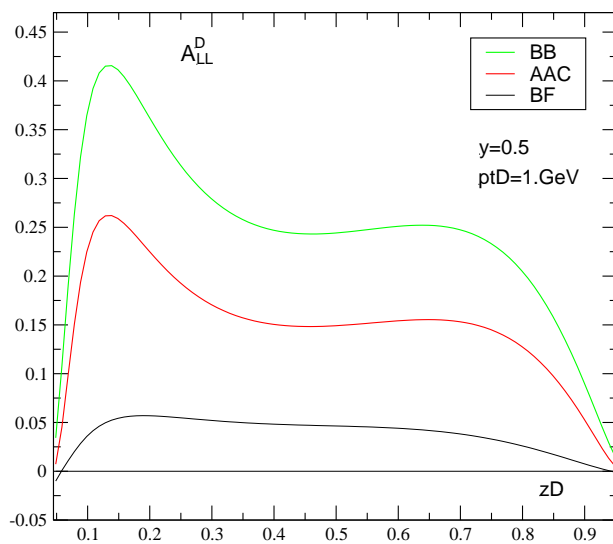


Figure 7.10: The spin asymmetry as a function of the fractional energy $z_D = E_D/E_\gamma$, at fixed photon energy $y = 0.5$ (p_{tD} , $g(x)$, $\Delta g(x)$ and $D_c^H(z)$ as in Fig. 7.8).

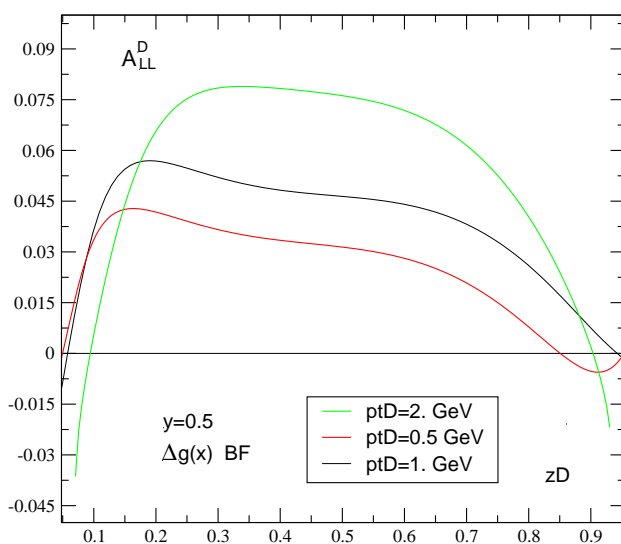


Figure 7.11: The spin asymmetry as a function of z_D at different p_{tD} and Δg given by BF-A (y , $g(x)$ and $D_c^H(z)$ as in Fig. 7.10)

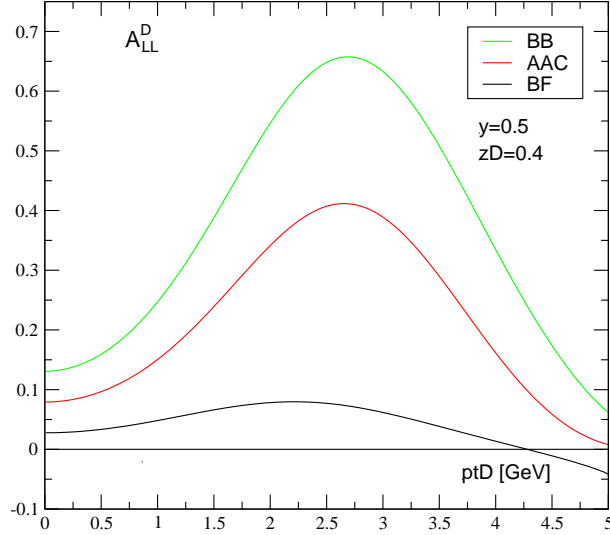


Figure 7.12: The spin asymmetry as a function of the D meson transverse momentum p_{tD} , at fixed photon energy $y = 0.5$ (z_D , $g(x)$, $\Delta g(x)$ and $D_c^H(z)$ as in Fig. 7.8).

gluon distribution makes the result completely unreliable.

As an example, the dependence of the asymmetry on the precise shape of the fragmentation function is shown as a function of p_{tD} in Fig. 7.15, at fixed y and z_D . The BF-A and NLO MRST parametrizations are used for the polarized and unpolarized gluon respectively. The choice of the fragmentation function has no significant impact on the p_{tD} -distribution over the entire kinematical region. Similar results are found for the asymmetries as a function of the other relevant variables.

Finally, as already noted in [68], also a moderate scale-dependence of the asymmetry as a function of p_{tD} is observed in the region of interest, i.e. for $p_{tD} \lesssim 2$ GeV. This is displayed in Fig. 7.16 with $\Delta g(x)$ and $g(x)$ as in Fig. 7.15, for a simultaneous variation of the factorization and renormalization scales by a factor $a = 0.25, 1, 4$ around the value $\mu_F^2 = \mu_R^2 = 4m_c^2$.

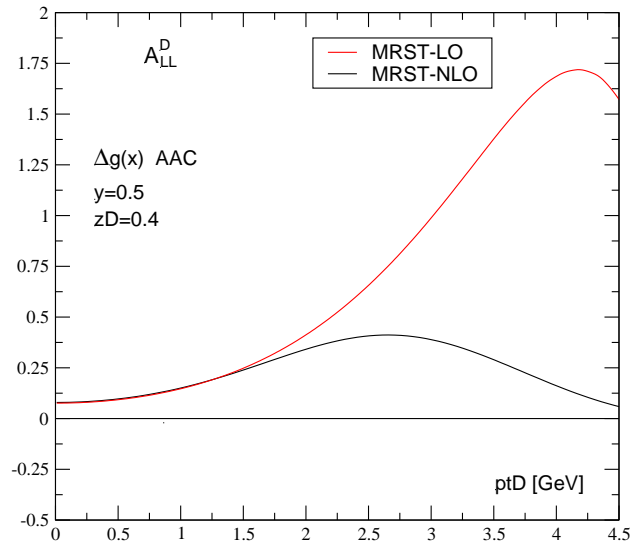


Figure 7.13: Effect of the uncertainty in the unpolarized gluon distribution at large x on the asymmetry as a function of p_{tD} . LO and NLO MRST parametrizations of g are compared, with Δg given by AAC and $D_c^H(z)$, y , z_D as in Fig. 7.12.

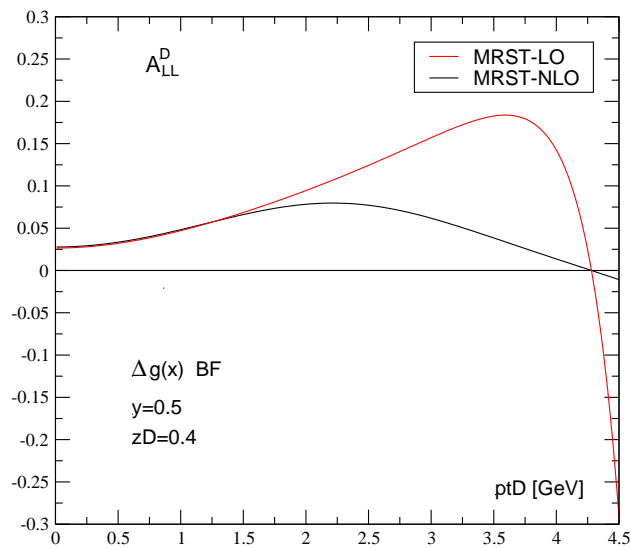


Figure 7.14: Effect of the uncertainty in the unpolarized gluon distribution g as in Fig. 7.13, with Δg given by BF-A.

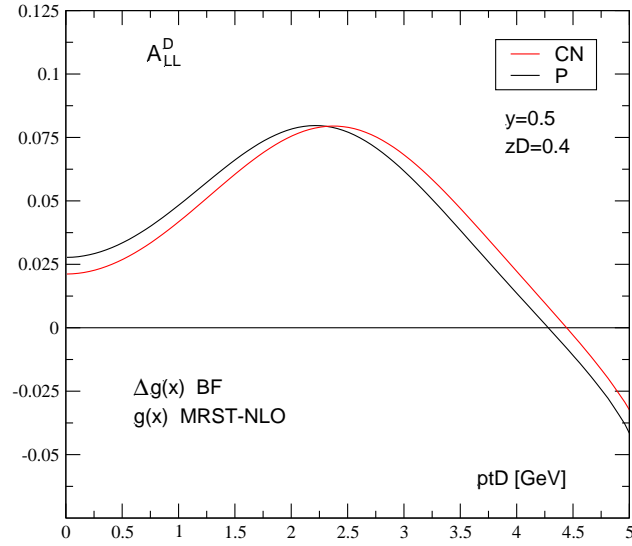


Figure 7.15: The asymmetry as a function of p_{tD} with two different fragmentation functions, P and CN. Δg , y and z_D are as in Fig. 7.14 and g is given by MRST at NLO.

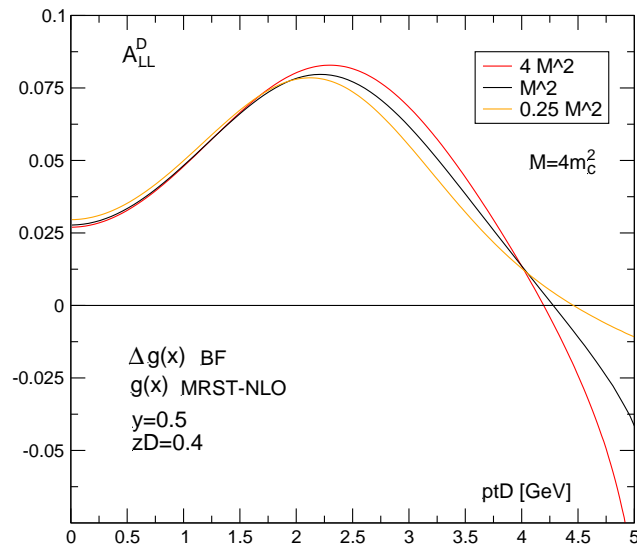


Figure 7.16: The asymmetry as a function of p_{tD} at different scales $\mu_F^2 = \mu_R^2 = a 4m_c^2$, $a = 0.25, 1, 4$. Δg , g , y and z_D are as in Fig. 7.14 and D_c^H is given by the Peterson function.

7.3.2 Results from pseudo-data fit

As a last step, pseudo-data for open-charm asymmetries A_{LL}^D have been generated by a Gaussian-distributed random shift around the theoretical values. The latter are based upon two different assumptions on the polarized gluon density, namely the AAC parametrization [38] and the best-fit result of type-A (BF-A) discussed in Sec. 6. Both are displayed in Fig. 7.5 at the scale of the process at hand.

The primary goal is to determine to what extent such data can pin down the x -shape of Δg , so far unconstrained by inclusive DIS measurements, and potentially reduce the systematic error induced by the choice of the initial parametrization.

To this end, twelve bins have been selected for the measured kinematic variables, with central values $y = 0.35, 0.65, z_D = 0.45, 0.65$ and $p_{tD} = 0.5, 1, 2$ GeV. These are chosen such that they uniformly cover the experimentally relevant kinematical region.

The related asymmetries A_{LL}^D are calculated in each bin, for the chosen polarized gluon. On the basis of the total number of the reconstructed D mesons and their distribution with respect to each relevant variable [79], a statistical error is assigned to the predicted asymmetries, i.e. $\delta A_{LL}^D = \sqrt{(1 - (A_{LL}^D)^2)/N}$, where N is the estimated total number of events in each bin. The theoretical values are then randomly shifted with Gaussian distribution to produce the final set of 12 pseudo-data for the assumed polarized gluon parametrization.

As expected, due to the sensitivity of A_{LL}^D to Δg , very different values of pseudo-asymmetries are found by using the two distinct polarized gluons, i.e. AAC and BF-A; the two sets of related pseudo-data, when included in the global fit of pdfs along with inclusive DIS data (see Sec. 6), also produce very different results for the fitted gluon polarizations.

Indeed, a first set of 12 pseudo-data has been generated by using the AAC parametrization for $\Delta g(x)$ (\tilde{A}_{AAC} in what follows), and included in the global fit of type-A (Sec. 6). A glance to Fig. 7.17 reveals the significant impact of the \tilde{A}_{AAC} pseudo-data on the x -shape of Δg . Here, the original best fit result BF-A (only inclusive data) for Δg at the initial scale $Q^2 = 1$ GeV² is compared with that obtained by including \tilde{A}_{AAC} pseudo-data.

Also shown in Fig. 7.17 are the statistical errors propagated to characteristic points of $x\Delta g(x)$, namely $x = 0.1$ (roughly corresponding to the region

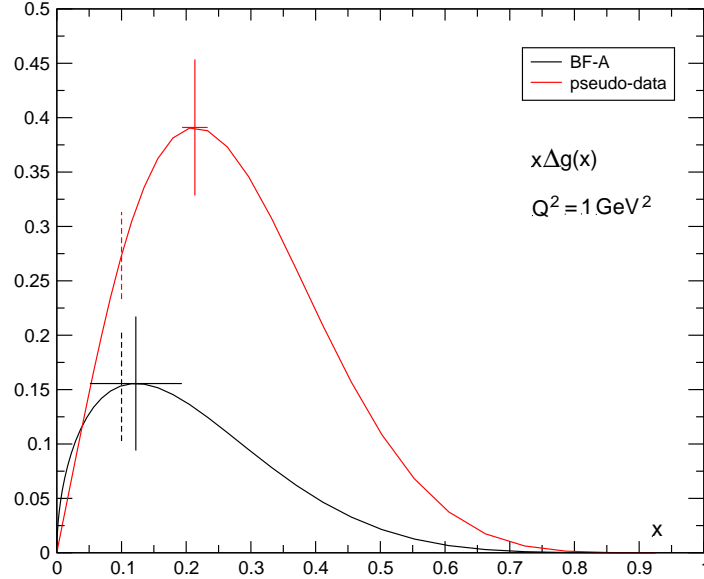


Figure 7.17: Best fit result (type-A) for Δg at $Q^2 = 1 \text{ GeV}^2$ including \tilde{A}_{AAC} pseudo-data, compared to BF-A (only inclusive data).

probed by COMPASS), the position and the value of the peak in $x\Delta g(x)$. As can be seen, in particular the peak values in the two cases are not consistent within several standard deviations.

Then, in order to perform a quantitative study of the impact of open-charm asymmetries on the x -shape of Δg , a second set of pseudo-data has been generated by using the best-fit result of type-A for the polarized gluon (\tilde{A}_{BF-A}). \tilde{A}_{BF-A} pseudo-data are then included in two types of fit to world data, type-A and B respectively (see Sec. 6.5.2), that differ by the assumed functional form of pdfs at the initial scale. The results for the gluon polarization are summarized in Fig. 7.18.

As already pointed out, the two original best-fit gluons, type-A and B respectively, both provide equally good fit to inclusive DIS data, even though they significantly differ in shape. These are represented in Fig. 7.18 by black-solid (BF-A) and black-dashed (BF-B) curves respectively. The red-solid and red-dashed curves in Fig. 7.18 denote the type-A and B results respectively

(CH-A and CH-B), obtained by adding the $\tilde{A}_{\text{BF-A}}$ pseudo-data to the fit. As a measure of the systematic error induced by the choice of the input gluon density, one may compare the values of characteristic points (and the related errors) of the x -shape for the two types of best-fit gluons (type-A and B), with and without charm data. Specifically, for only inclusive data fits, the position of the peak of $x\Delta g(x)$ and the corresponding function value in the case of type-A parametrization turn out to be

$$x_{\text{max}} = 0.122 \pm 0.071, \quad x_{\text{max}}\Delta g(x_{\text{max}}) = 0.156 \pm 0.062 \quad (\text{BF-A}), \quad (7.33)$$

whereas for the type-B fit they read

$$x_{\text{max}} = 0.552 \pm 0.169 \quad x_{\text{max}}\Delta g(x_{\text{max}}) = 0.421 \pm 0.871 \quad (\text{BF-B}). \quad (7.34)$$

The quoted uncertainties are obtained by propagating the related statistical errors of the parameters from the fit.

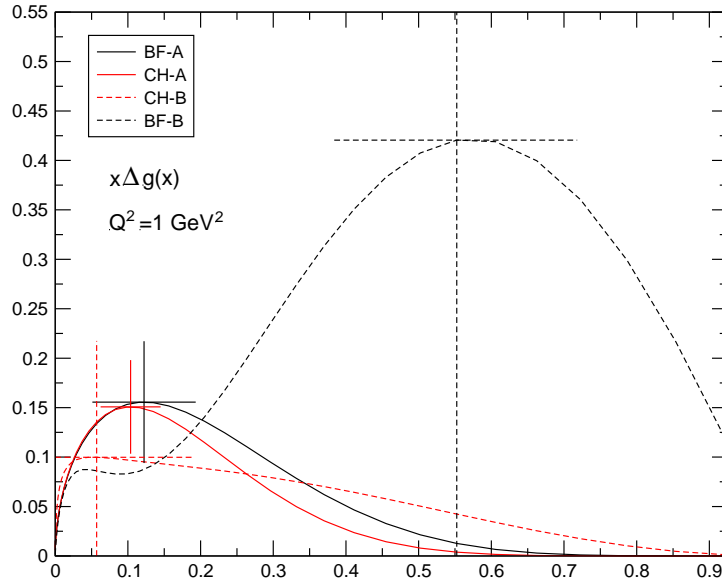


Figure 7.18: Best fit results for Δg at $Q^2 = 1 \text{ GeV}^2$ for inclusive DIS data alone (black curves) and including $\tilde{A}_{\text{BF-A}}$ pseudo-data (red curves).

On the other hand, by including charm pseudo-data $\tilde{A}_{\text{BF-A}}$, one has

$$x_{\text{max}} = 0.104 \pm 0.041, \quad x_{\text{max}}\Delta g(x_{\text{max}}) = 0.151 \pm 0.047 \quad (\text{CH-A}) \quad (7.35)$$

for the type-A parametrization, and

$$x_{\text{max}} = 0.057 \pm 0.132, \quad x_{\text{max}}\Delta g(x_{\text{max}}) = 0.100 \pm 0.118 \quad (\text{CH-B}), \quad (7.36)$$

in the case of type-B, the main effect being obviously on the latter. Specifically, one may take e.g. the half-difference of the central values in the two fits, A and B respectively, as an estimate of the uncertainty on the position of the peak in the polarized gluon density; in the case of inclusive DIS data alone, from Eqs. (7.33-7.34) this amounts to roughly $\simeq 0.2$, whereas by including charm pseudo-data in the two fits it turns out to be strongly reduced, i.e. $\simeq 0.02$ by using Eqs. (7.35-7.36). Indeed, in the latter case, the positions of the peak of $x\Delta g(x)$ for type-A and B are now largely consistent within the errors. Similar consideration hold also for the corresponding function values.

This fact clearly demonstrates the capability of open-charm asymmetries in constraining the x -shape of the gluon polarization, significantly reducing the bias induced by the choice of input densities.

Finally, the two best-fit results for all the pdfs parameters, including $\tilde{A}_{\text{BF-A}}$ pseudo-data are shown in Tab. 9 below. Comparing these results with the type-A and B fits to inclusive DIS data alone, respectively Tabs. 5 and 7, it can be seen that, as expected, charm pseudo-data have no sizable effect on quark distributions. Moreover, the statistical errors are generally slightly reduced, and the quality of the fit improved.

In particular, as far as the gluon first moment is concerned, very close values arise from the two types of fits if charm pseudo-data are included. Averaging over the two best-fit values one would obtain $\Delta g(1, 1 \text{ GeV}^2) = 0.54 \pm 0.08$, to be compared with the second of Eqs. (6.9).

One may thus conclude that the much constrained x -shape of the spin-dependent gluon distribution, beside the more precise determination of the first moment, is the most relevant feature of a global analysis that includes open-charm asymmetries along with inclusive DIS data. Indeed, charm pseudo-data strongly reduce the impact of the initial parametrization on the results, that significantly biases inclusive data analyses. Thus, on the basis of the above results, real charm asymmetries from the COMPASS experiment

should be capable to discriminate among the existing different best-fit forms of the gluon polarization which equally well describe DIS data.

Parameters ($Q_0^2 = 1 \text{ GeV}^2$)	type-A (CH-A)	type-B (CH-B)
η_Σ	0.388 ± 0.018	0.391 ± 0.016
α_Σ	1.184 ± 0.317	2.670 ± 0.412
β_Σ	1.958 ± 0.974	3.614 ± 0.456
γ_Σ	-1.229 ± 0.198	–
η_g	0.525 ± 0.123	0.553 ± 0.095
α_g	-0.481 ± 0.321	3.529 ± 0.257
β_g	8. (fixed)	2.281 ± 1.360
γ_g	6.620 ± 14.070	11.656 ± 12.533
η_3	1.127 ± 0.034	1.207 ± 0.034
α_{NS}	-0.315 ± 0.270	1.624 ± 0.110
β_{NS}	2.965 ± 0.328	5.498 ± 0.170
γ_{NS}	8.966 ± 12.571	-0.180 ± 0.050
$\chi^2/\text{d.o.f}$	0.888	0.902

Tab. 9. Fits of type-A and B, including 12 charm pseudo-asymmetries $\tilde{A}_{\text{BF-A}}$ to the set of 238 inclusive DIS data points (cut at $W \geq 3 \text{ GeV}$, see Sec. 6).

Chapter 8

Conclusions

To summarize, the possibility of inferring the spin-dependent gluon distribution from scaling violations has been thoroughly studied, by means of a full NLO phenomenological analysis of the available experimental inclusive DIS data, performed in the Adler-Bardeen factorization scheme.

Special attention, in particular, has been paid on the selection of the lower-energy data, in order to avoid systematic errors induced by higher-twist corrections. Indeed, a bulk of data in polarized DIS are restricted to the region of the final-state invariant mass which involves large Bjorken- x at moderate values of the momentum transfer Q^2 , roughly $1 \lesssim W \lesssim 3$ GeV.

It has been shown that such data do not sizably affect the shape of quark and gluon densities, whereas the main effect of the lower energy points (mainly from the CLAS and the HERMES experiments) is essentially the improvement in the determination of the higher-twist contributions to the structure function g_1 . Then, for a consistent perturbative treatment of world data, lower energy points can be safely discarded; to this end, a quantitative criterion has been established by a phenomenological study of higher-twist corrections to g_1 . As a result, a lower bound has been imposed on DIS data at $W = 3$ GeV, since above this threshold higher-twist corrections are consistent with zero within 1.5 standard deviations, thus justifying a pure perturbative analysis.

Furthermore, the bias produced by the choice of input densities has been investigated by performing global fits to the same subset of DIS data using different boundary conditions for pdfs (namely type-A and B fits).

It turns out that the spin-dependent gluon distribution exhibits a sizable dependence on the assumed functional form, whereas minor effects are observed in the quark sector. Indeed, best-fit gluons obtained with different input densities (type-A and B) both provide equally good fits to inclusive DIS data, even though they significantly differ in shape. On the other hand, the first moment of the polarized gluon turns out to be more stable with respect to the initial parametrization, and, in particular, smaller if compared to previous estimates. If all the theoretical errors are properly taken into account, the final estimate reads

$$\Delta g(1, 1 \text{ GeV}^2) = 0.68 \pm 0.12 (\text{exp}) \pm 0.29 (\text{th}),$$

in reasonable agreement with the results of other recent phenomenological studies.

Thus, even though the better coverage of the (x, Q^2) -plane, mainly due to the recent precise COMPASS data, allows a more reliable determination of the gluon first moment, an analysis based on inclusive DIS data alone is not capable to pin down the x -shape of the gluon distribution, which is still largely unknown.

At present, further constraints are expected to come from direct measurements of $\Delta g(x)$, which are based upon the observation of gluon-initiated processes at the partonic level, such as for example production of heavy-flavored hadrons and jets with large transverse momentum, from both hadro- and lepto-production.

Actually, one of the most promising approach is the measurement of open-charm events from (fixed target) polarized lepton-nucleon scattering, since charmed mesons in the final states are a clean signature of the underlying photon-gluon fusion mechanism, with essentially no competing processes and moderate NLO corrections. Furthermore, asymmetry data of open-charm photoproduction from the COMPASS experiment are upcoming. Therefore, a LO analysis of this process has been performed by constructing a close theoretical description of the actually observed quantities at COMPASS.

As a first result, this study has revealed in particular that, in the range of gluon momentum fractions accessible at COMPASS energies, that is restricted to $x \gtrsim 0.1$, the absolute value of the gluon polarization has a significant impact on the size of the asymmetry viewed as a function of each of the kinematic variables of the outgoing D meson. This is interesting in view of the fact that available polarized gluon distributions have similar values

of the first moment, but very different shapes and thus very different values at fixed $x \gtrsim 0.1$. For instance, the best-fit result of type-A of the present analysis, BF-A, and the AAC parametrizations both have a first moment of Δg around 0.5 at $Q^2 = 1 \text{ GeV}^2$, but at $x = 0.2$ they differ by more than a factor two, as seen in Fig. 7.5. Open-charm data may thus resolve the gluon x -shape in this region.

In order to assess to what extent such data can actually pin down the x -shape of $\Delta g(x)$, so far unconstrained by scaling violations, and potentially reduce the systematic error induced by the choice of input densities, a phenomenological study has been performed by using open-charm pseudo-data, generated by a Gaussian-distributed random shift around the theoretical values. Adding pseudo-asymmetries to global fits of world data with different input densities, type-A and B respectively, a much constrained x -shape for the fitted gluon turns out, as well as a better determined first moment. Specifically, the two best-fit forms for the gluon polarization become largely consistent in shape if charm pseudo-data are included in the analysis.

This fact clearly emphasizes that, at variance with analyses based on scaling violations, the open-charm approach should be capable to significantly reduce the bias induced by the choice of the initial parametrization, which is one of the most relevant theoretical uncertainties in the determination of the spin-dependent gluon distribution, and thus to discriminate among the available different best-fit forms which equally well describe DIS data.

Bibliography

- [1] J. Ashman *et al.* [European Muon Collaboration], Phys. Lett. B **206** (1988) 364; J. Ashman *et al.* [European Muon Collaboration], Nucl. Phys. B **328** (1989) 1.
- [2] B. Lampe and E. Reya, Phys. Rept. **332** (2000) 1 [arXiv:hep-ph/9810270].
- [3] J. Kodaira *et al.*, Phys. Rev. D **20** (1979) 627; Nucl. Phys. B **159** (1979) 99.
- [4] S. Forte, arXiv:hep-ph/9409416.
- [5] M. Anselmino, A. Efremov and E. Leader, Phys. Rept. **261** (1995) 1 [Erratum-ibid. **281** (1997) 399] [arXiv:hep-ph/9501369]; E. V. Shuryak and A. I. Vainshtein, Nucl. Phys. B **199** (1982) 451.
- [6] R. Mertig and W. L. van Neerven, Z. Phys. C **70** (1996) 637 [arXiv:hep-ph/9506451]; W. Vogelsang, Phys. Rev. D **54** (1996) 2023 [arXiv:hep-ph/9512218].
- [7] J. Ellis and M. Karliner, Phys. Lett. B **313** (1993) 131; Phys. Lett. B **341** (1995) 197.
- [8] W. M. Yao *et al.* [Particle Data Group], J. Phys. G **33** (2006) 1.
- [9] P. G. Ratcliffe, Phys. Lett. B **365** (1996) 383 [arXiv:hep-ph/9509237]; F. E. Close and R. G. Roberts, Phys. Lett. B **316** (1993) 165 [arXiv:hep-ph/9306289].
- [10] G. Altarelli and G. G. Ross, Phys. Lett. B **212** (1988) 391, R. D. Carlitz, J. C. Collins and A. H. Mueller, Phys. Lett. B **214** (1988) 229.

- [11] J. D. Bjorken, Phys. Rev. **148** (1966) 1467; Phys. Rev. D **1** (1970) 465.
- [12] G. Altarelli, R. D. Ball, S. Forte and G. Ridolfi, Acta Phys. Polon. B **29** (1998) 1145 [arXiv:hep-ph/9803237].
- [13] J. R. Ellis and R. L. Jaffe, Phys. Rev. D **9** (1974) 1444 [Erratum-ibid. D **10** (1974) 1669].
- [14] S. Forte, Phys. Lett. B **224** (1989) 189; Nucl. Phys. B **331** (1990) 1; S. Forte and E. V. Shuryak, Nucl. Phys. B **357** (1991) 153.
- [15] S. J. Brodsky and B. Q. Ma, Phys. Lett. B **381** (1996) 317.
- [16] S. J. Brodsky, J. Ellis and M. Karliner, Phys. Lett. B **206** (1988) 309.
- [17] E. B. Zijlstra and W. L. van Neerven, Nucl. Phys. B **417** (1994) 61 [Erratum-ibid. B **426** (1994 ERRAT,B773,105-106.2007) 245.1994 ER-RAT,B773,105].
- [18] G. Altarelli, Phys. Rept. **81** (1982) 1.
- [19] G. Altarelli and G. Parisi, Nucl. Phys. B **126** (1977) 298.
- [20] R. D. Ball, S. Forte and G. Ridolfi, Phys. Lett. B **378** (1996) 255 [arXiv:hep-ph/9510449].
- [21] K. Abe *et al.* [E143 Collaboration], Phys. Rev. Lett. **76** (1996) 587 [arXiv:hep-ex/9511013]; K. Abe *et al.* [E154 Collaboration], Phys. Lett. B **404** (1997) 377 [arXiv:hep-ex/9705017].
- [22] A. Piccione and G. Ridolfi, Nucl. Phys. B **513** (1998) 301 [arXiv:hep-ph/9707478].
- [23] J. Kodaira, S. Matsuda, K. Sasaki and T. Uematsu, Nucl. Phys. B **159** (1979) 99.
- [24] S. Wandzura and F. Wilczek, Phys. Lett. B **72** (1977) 195.
- [25] F. James, CERN Program Library Long Writeup D506. See <http://wwwasdoc.web.cern.ch/wwwasdoc/minuit/minmain.html>.
- [26] G. Altarelli, R. D. Ball, S. Forte and G. Ridolfi, Nucl. Phys. B **496** (1997) 337 [arXiv:hep-ph/9701289].

- [27] M. Hirai, S. Kumano and N. Saito, Phys. Rev. D **74** (2006) 014015 [arXiv:hep-ph/0603213].
- [28] E. Leader, A. V. Sidorov and D. B. Stamenov, Phys. Rev. D **73** (2006) 034023 [arXiv:hep-ph/0512114].
- [29] G. Altarelli, S. Forte and G. Ridolfi, Nucl. Phys. B **534** (1998) 277 [arXiv:hep-ph/9806345]; Nucl. Phys. Proc. Suppl. **74** (1999) 138 [arXiv:hep-ph/9808462].
- [30] B. Adeva *et al.* [Spin Muon Collaboration], Phys. Rev. D **58** (1998) 112001.
- [31] K. Abe *et al.* [E143 collaboration], Phys. Rev. D **58** (1998) 112003 [arXiv:hep-ph/9802357].
- [32] P. L. Anthony *et al.* [E155 Collaboration], Phys. Lett. B **493** (2000) 19 [arXiv:hep-ph/0007248].
- [33] A. Airapetian *et al.* [HERMES Collaboration], Phys. Lett. B **442** (1998) 484 [arXiv:hep-ex/9807015].
- [34] P. L. Anthony *et al.* [E155 Collaboration], Phys. Lett. B **463** (1999) 339 [arXiv:hep-ex/9904002].
- [35] P. L. Anthony *et al.* [E142 Collaboration], Phys. Rev. D **54** (1996) 6620 [arXiv:hep-ex/9610007].
- [36] K. Ackerstaff *et al.* [HERMES Collaboration], Phys. Lett. B **404** (1997) 383 [arXiv:hep-ex/9703005].
- [37] K. Abe *et al.* [E154 Collaboration], Phys. Rev. Lett. **79** (1997) 26 [arXiv:hep-ex/9705012].
- [38] M. Hirai, S. Kumano and N. Saito [Asymmetry Analysis Collaboration], Phys. Rev. D **69** (2004) 054021 [arXiv:hep-ph/0312112].
- [39] S. Forte, M. L. Mangano and G. Ridolfi, Nucl. Phys. B **602** (2001) 585 [arXiv:hep-ph/0101192].
- [40] [arXiv:hep-ex/0701014].

- [41] V. Y. Alexakhin *et al.* [COMPASS Collaboration], Phys. Lett. B **647** (2007) 8 [arXiv:hep-ex/0609038].
- [42] A. Airapetian *et al.* [HERMES Collaboration], Phys. Rev. D **75** (2007) 012007 [Erratum-ibid. D **76** (2007) 039901] [arXiv:hep-ex/0609039].
- [43] X. Zheng *et al.* [Jefferson Lab Hall A Collaboration], Phys. Rev. C **70** (2004) 065207 [arXiv:nucl-ex/0405006].
- [44] B. Adeva *et al.* [Spin Muon Collaboration], Phys. Rev. D **60** (1999) 072004 [Erratum-ibid. D **62** (2000) 079902].
- [45] R. Fatemi *et al.* [CLAS Collaboration], Phys. Rev. Lett. **91** (2003) 222002 [arXiv:nucl-ex/0306019].
- [46] K. V. Dharmawardane *et al.* [CLAS Collaboration], Phys. Lett. B **641** (2006) 11 [arXiv:nucl-ex/0605028].
- [47] L. W. Whitlow, S. Rock, A. Bodek, E. M. Riordan and S. Dasu, Phys. Lett. B **250** (1990) 193.
- [48] K. Abe *et al.* [E143 Collaboration], Phys. Lett. B **452** (1999) 194 [arXiv:hep-ex/9808028].
- [49] L. H. Tao *et al.* [E140X Collaboration], Z. Phys. C **70** (1996) 387; M. Arneodo *et al.* [New Muon Collaboration], Nucl. Phys. B **483** (1997) 3 [arXiv:hep-ph/9610231]; U. K. Yang *et al.* [CCFR/NuTeV Collaboration], arXiv:hep-ex/9806023; J. P. Berge *et al.*, Z. Phys. C **49** (1991) 187.
- [50] M. Arneodo *et al.* [NMC Collaboration], Phys. Lett. B **364** (1995) 107
- [51] See <http://sophia.ecm.ub.es/f2neural/>
- [52] L. Del Debbio, S. Forte, J. I. Latorre, A. Piccione and J. Rojo [NNPDF Collaboration], JHEP **0503** (2005) 080 [arXiv:hep-ph/0501067]; S. Forte, L. Garrido, J. I. Latorre and A. Piccione, JHEP **0205** (2002) 062 [arXiv:hep-ph/0204232].
- [53] M. Osipenko *et al.*, Phys. Rev. D **71** (2005) 054007 [arXiv:hep-ph/0503018].

- [54] S. Simula, M. Osipenko, G. Ricco and M. Taiuti, Phys. Rev. D **65** (2002) 034017 [arXiv:hep-ph/0107036].
- [55] E. Leader, A. V. Sidorov and D. B. Stamenov, Phys. Rev. D **75** (2007) 074027 [arXiv:hep-ph/0612360].
- [56] G. Ridolfi, *In the Proceedings of QCD @ Work 2003: 2nd International Workshop on Quantum Chromodynamics: Theory and Experiment, Conversano, Italy, 14-18 Jun 2003, pp 019.*
- [57] J. Blumlein and A. Tkabladze, Nucl. Phys. B **553** (1999) 427 [arXiv:hep-ph/9812478].
- [58] J. Bluemlein and H. Bottcher, Nucl. Phys. B **636** (2002) 225 [arXiv:hep-ph/0203155].
- [59] M. Gluck, E. Reya, M. Stratmann and W. Vogelsang, Phys. Rev. D **63** (2001) 094005 [arXiv:hep-ph/0011215].
- [60] M. Gluck, E. Reya, M. Stratmann and W. Vogelsang, Phys. Rev. D **53** (1996) 4775 [arXiv:hep-ph/9508347]; T. Gehrmann and W. J. Stirling, Phys. Rev. D **53** (1996) 6100 [arXiv:hep-ph/9512406].
- [61] G. Bunce, N. Saito, J. Soffer and W. Vogelsang, Ann. Rev. Nucl. Part. Sci. **50** (2000) 525 [arXiv:hep-ph/0007218].
- [62] B. Jager, A. Schafer, M. Stratmann and W. Vogelsang, Phys. Rev. D **67** (2003) 054005 [arXiv:hep-ph/0211007].
- [63] D. de Florian, Phys. Rev. D **67** (2003) 054004 [arXiv:hep-ph/0210442].
- [64] B. Jager, M. Stratmann and W. Vogelsang, Phys. Rev. D **70**, 034010 (2004) [arXiv:hep-ph/0404057].
- [65] S. S. Adler *et al.* [PHENIX Collaboration], Phys. Rev. D **73** (2006) 091102 [arXiv:hep-ex/0602004]; Phys. Rev. Lett. **93** (2004) 202002 [arXiv:hep-ex/0404027].
- [66] J. Kiryluk [STAR Collaboration], AIP Conf. Proc. **842** (2006) 327 [arXiv:hep-ex/0512040].

- [67] S. Frixione and G. Ridolfi, Phys. Lett. B **383** (1996) 227 [arXiv:hep-ph/9605209].
- [68] M. Stratmann and W. Vogelsang, Z. Phys. C **74** (1997) 641 [arXiv:hep-ph/9605330].
- [69] A. Airapetian *et al.* [HERMES Collaboration], Phys. Rev. Lett. **84** (2000) 2584 [arXiv:hep-ex/9907020].
- [70] E. S. Ageev *et al.* [COMPASS Collaboration], Phys. Lett. B **633** (2006) 25 [arXiv:hep-ex/0511028].
- [71] B. Adeva *et al.* [Spin Muon Collaboration (SMC)], Phys. Rev. D **70** (2004) 012002 [arXiv:hep-ex/0402010].
- [72] C. Hendlmeier, M. Stratmann and A. Schafer, Eur. Phys. J. C **48** (2006) 135 [arXiv:hep-ph/0606096].
- [73] C. Hendlmeier, M. Stratmann and A. Schafer, arXiv:0706.3766 [hep-ph].
- [74] See e.g. A. Bravar, D. von Harrach and A. Kotzinian, Phys. Lett. B **421** (1998) 349 [arXiv:hep-ph/9710266].
- [75] G. Baum *et al.*, COMPASS collab., CERN/SPSLC-96-14, CERN/SPSLC-93-30.
- [76] P. Abbon *et al.* [COMPASS Collaboration], Nucl. Instrum. Meth. A **577** (2007) 455 [arXiv:hep-ex/0703049].
- [77] J. M. Le Goff, see <http://wwwcompass.cern.ch/compass/publications/talks/#2007>
- [78] K. Kurek [COMPASS Collaboration], PoS D **IFF2006** (2006) 010.
- [79] S. Koblitz [COMPASS Collaboration], arXiv:0707.0175 [hep-ex].
- [80] I. Bojak and M. Stratmann, Phys. Lett. B **433** (1998) 411 [arXiv:hep-ph/9804353]; Nucl. Phys. B **540** (1999) 345 [arXiv:hep-ph/9807405].
- [81] C. F. von Weizsacker, Z. Phys. **88** (1934) 612.

- [82] D. de Florian and S. Frixione, Phys. Lett. B **457** (1999) 236 [arXiv:hep-ph/9904320].
- [83] S. Frixione, M. L. Mangano, P. Nason and G. Ridolfi, Phys. Lett. B **319** (1993) 339 [arXiv:hep-ph/9310350].
- [84] M. Klasen, Rev. Mod. Phys. **74** (2002) 1221 [arXiv:hep-ph/0206169].
- [85] B. Jager, M. Stratmann and W. Vogelsang, Phys. Rev. D **68** (2003) 114018 [arXiv:hep-ph/0309051].
- [86] M. Drees and R. M. Godbole, Phys. Rev. D **39** (1989) 169; Phys. Rev. Lett. **61** (1988) 682; J. F. Owens, Phys. Rev. D **21** (1980) 54.
- [87] M. Stratmann and W. Vogelsang, Phys. Lett. B **386** (1996) 370 [arXiv:hep-ph/9606346].
- [88] D. de Florian and W. Vogelsang, Phys. Rev. D **57** (1998) 4376 [arXiv:hep-ph/9712273].
- [89] See http://www.phenix.bnl.gov/WWW/publish/abhay/Home_of_EIC/
- [90] J. Smith and W. L. van Neerven, Nucl. Phys. B **374** (1992) 36.
- [91] R. K. Ellis and P. Nason, Nucl. Phys. B **312** (1989) 551.
- [92] S. Frixione, M. L. Mangano, P. Nason and G. Ridolfi, Adv. Ser. Direct. High Energy Phys. **15** (1998) 609 [arXiv:hep-ph/9702287], and Refs. therein.
- [93] M. Gluck, E. Reya and W. Vogelsang, Nucl. Phys. B **351** (1991) 579.
- [94] A. D. Martin, W. J. Stirling and R. S. Thorne, Phys. Lett. B **636** (2006) 259 [arXiv:hep-ph/0603143].
- [95] C. Peterson, D. Schlatter, I. Schmitt and P. M. Zerwas, Phys. Rev. D **27** (1983) 105.
- [96] J. Chrin, Z. Phys. C **36** (1987) 163.
- [97] M. Cacciari, arXiv:hep-ph/9708282.
- [98] G. Colangelo and P. Nason, Phys. Lett. B **285** (1992) 167.